HARVARD UNIVERSITY
Graduate School of Arts and Sciences

DISSERTATION ACCEPTANCE CERTIFICATE

The undersigned, appointed by the

The Committee on Higher Degrees in Chemical Biology

have examined a dissertation entitled

All-Optical Electrophysiology of Excitation and Inhibition in Neural Circuits

presented by

Linlin Fan

candidate for the degree of Doctor of Philosophy and hereby certify that it is worthy of acceptance.

Signature _____

Typed name: Prof. Rachel Wilson

Signature _____

Typed name: Prof. Gary Yellen

Signature _____

Typed name: Prof. Naoshige Uchida

Signature _____

Typed name: Prof. Adam Cohen

Date: 9/4/2019

All-Optical Electrophysiology of Excitation and Inhibition in Neural Circuits

A dissertation presented
by
Linlin Fan
to
The Committee on Higher Degrees in Chemical Biology

in partial fulfillment of the requirements
for the degree of
Doctor of Philosophy
in the subject of
Chemical Biology

Harvard University
Cambridge, Massachusetts
September 2019

Dissertation advisor: Adam E. Cohen Linlin Z. Fan

All-Optical Electrophysiology of Excitation and Inhibition in Neural Circuits

Abstract

The stability of neural dynamics arises through a tight coupling of excitatory (E) and inhibitory (I) signals, and imbalance in these signals is implicated in many nervous system disorders such as schizophrenia and autism. Genetically encoded voltage indicators (GEVIs) can report both spikes and subthreshold dynamics, but voltage only reveals the combined effects of E and I currents, not their separate contributions individually. All-optical electrophysiology, simultaneous optical manipulation and recording of electrical activity of genetically defined neurons, would greatly facilitate studies of E/I balance in neuronal information processing. My PhD work has been focused on developing optical methods for probing E/I balance in cultured neurons for disease modeling and in awake, behaving mice to study attentional control of cortical layer 1 neurons.

First, I developed optogenetic tools and methods for all-optical interrogation of synaptic electrophysiology (synOptopatch), and applied the technique to address an important and controversial neurobiological question: why does blockade of excitatory N-methyl-D-aspartate receptor (NMDAR)-mediated synaptic transmission by ketamine lead to overall enhanced neural activity? This counterintuitive

phenomenon is important because NMDAR hypofunction and consequent network hyperactivity are hypothesized to occur in schizophrenia and are the basis of ketamine-induced model of schizophrenia. I developed genetic constructs to express a channelrhodopsin actuator and an archaerhodopsin-derived voltage indicator in disjoint subsets of neurons. Optically induced activity in the channelrhodopsin-expressing neurons generated excitatory and inhibitory postsynaptic potentials that could be optically resolved in reporter-expressing neurons. I demonstrated synOptopatch recordings in cultured rodent neurons and in acute rodent brain slice. In synOptopatch measurements of primary rodent cultures, acute ketamine administration suppressed disynaptic inhibitory feedbacks, mimicking the effect of this drug on network function in both rodents and humans. I discovered that this action of ketamine is through blocking E-to-I synapses. These results establish an in vitro all-optical model of disynaptic disinhibition, a synaptic defect hypothesized in schizophrenia-associated psychosis.

Second, I developed optogenetic tools and methods for all-optical dissection of excitation and inhibition in vivo, and revealed the input-output properties of barrel cortical L1 circuit in awake mice during sensory processing. Our brain receives constant inputs from all of our sensory organs; yet we only attend to inputs that are important to us, either because we have learned that the input is important (top-down signals) or because the input is novel or salient (bottom-up signals). How does the brain control which inputs get processed and which

get ignored? Cortical L1 interneurons have been hypothesized to be a hub for attentional control by integrating bottom-up and top-down inputs and controlling the underlying cortex through inhibition or disinhibition. However, it is unclear what their activity dynamics are in awake behaving mice during sensory processing and how they integrate the different inputs to produce the output. To study the input-output properties of L1 circuit, I developed all-optical electrophysiology in awake mice – simultaneous optical manipulation and recording of membrane voltage – to probe both spiking, and subthreshold excitation (E) and inhibition (I) individually, and neuromodulation in barrel cortex L1 neurons. Our studies reveal how the L1 microcircuit process sensory input by integrating thalamocortical excitation, lateral inhibition and top-down neuromodulatory inputs. We develop a simple computational model of the L1 microcircuit which captures the main features of our data. Together, these results suggest a model for computation in L1 interneurons consistent with their hypothesized role in attentional gating of the underlying cortex. My results demonstrate that all-optical electrophysiology can reveal basic principles of neural circuit function in vivo.

This work provides a roadmap for how one can use all-optical electrophysiology to dissect circuit function in awake mice, a task which has been formidably difficult using conventional tools (patch clamp or calcium imaging). In the context of attentional control, the work opens the possibility of follow-on experiments to study in greater detail the role of different types of sensory and modulatory

inputs to L1 as well as the downstream consequences of L1 activation.

Contents

Author List

The author for **Chapter 1** is L. Z. Fan.

The authors for **Chapter 2** are L. Z. Fan, R. Nehme, Y. Adam, E. S. Jeung, H. Wu, K. Eggan, D. B. Arnold, and A. E. Cohen.

The authors for **Chapter 3** are L. Z. Fan, S. Kheifets, U. L. Bohm, K. D. Piakevich, H. Wu, V. Parot, M. E. Xie, E. S. Boyden and A. E. Takesian and A. E. Cohen.

The author for **Chapter 4** is L. Z. Fan.

Author contributions are further detailed at the end of each chapter in the section entitled 'Manuscript Information'.

Contributions are further detailed at the end of Chapters **2** and **3**.

List of Figures

List of Tables

To my family and Lu.

Acknowledgments

First I want to thank my advisor and mentor Adam Cohen. Adam welcomed me to his lab with a big open heart five years ago. He not only teaches me how to do science: from how to fail fast, to being quantitative, and to being fearless, but also teaches me how to lead by example and how to be a good community member. His passion, rigor and intuition have been constantly inspiring me. I also appreciate the stimulating environment he creates and the opportunities he gives me to argue with him, through which I learn a lot and sometimes lead to unexpected research directions. I am forever in debt. I will for sure miss him and the lab.

I am thankful for my dissertation advisory committee: Bernardo Sabatini, Gary Yellen, and Rachel Wilson; and my thesis committee: Naoshige Uchida. None of my graduate studies would have been possible without their continuous support and encouragement. They have been constantly inspiring me to pursue good science. Thank you.

I am fortunate to collaborate with many great scientists, Anne Takesian at Harvard Medical School, Kiryl Piatkevich and Ed Boyden at MIT, Ralda Nehme and Kevin Eggan at Harvard Stem Cell Institute, Eun Sun Jung and Don Arnold at University of Southern California, Stephen Traynelis at Emory University, Ofer

Yizhar at Weizmann Institute, Miao Jing and Yulong Li at Peking University, Geoff Vargish and Takao Hensch at Harvard University. I want to specially thank Anne Takesian for having me in her lab meeting, constantly encouraging me, and discussing data and research directions along the second project. I am sincerely grateful.

Inside the lab, I am lucky to have worked with many talented rotation students, postdoc, graduate and undergraduate students: Hao Wu, Lin Zhi, Xiaotian Bi, Chris Qiu, Kathryn Evans, Kit Werley, Simon Kheifets, Vicente Parot, Urs Boehm, Michael Xie, Yoav Adam, Zheng Shi, Benjamin Gmeiner, Peng Zou, Haitan Xu and Bo Zeng. I am grateful to Hao, my rotation student, for teaching me how to code labview. I overlapped with Kit and worked with Simon for a short period of time. I am grateful to Kit, Simon and Vicente for helping transfer my vague optics knowledge in class to hands-on skills. I started my rotation with Yoav. I am grateful to him for showing me slicing and surgery.

I thank Katherine Williams, Melinda Lee, Shahin Begum, Andrew Preecha, Vaibhav Joshi, and Hanan Dache for valuable assistance over the years. I am also indebted to Maggie Kenar for assistance and counsel.

I have learned so much from my other lab mates and Anne's lab: Sami Farhi, Harry McNamara, He Tian, Miao-Ping Chien, Daan Brinks, Eli Weinstein, Liz Wood, Shan Lou, Stefano Baccoardo, Yooree Ha, Rosalind Xu, Shane Nichols, Hongkang Zhang, Amanda Klaeger, JJ Kim and Xin Tang; Dongqin Cai, Carolyn Sweeney,

Ana Castro, Vivek Kanumuri, Emma He, Jacob Mclennan and Benjamin Glickman. My fellow graduate students, Sami, Harry and Vicente have been cheering along the years.

I spent the last summer taking Methods in Computational Neuroscience class in the Marine Biological Laboratory. I thank Adam and Bernardo for supporting me for the application. I learned a lot in the class. I want to thank Steve Baccus and Bard Ermentrout for their guidance in my final project. I thank the teachers and my colleague classmates for the knowledge and the stimulating environment.

I want to thank my other mentors and the science community I meet on campus and in conferences and classes who give me valuable suggestions on science and career, including Michael Lin, Xiaodong Wang, Chao Tang, Zhaohui Xu, Peng Chen, Mike Hoppa, Loren Looger, Eric Schreiter, Nick Bellono, Alice Ting, Karel Svoboda, Michael Hausser, Darcy Peterka, Chris Harvey, Robert Edwards, Larry Abbott, Eve Marder, Nancy Kopell, Loren Frank, Jun Ding, Tianyi Mao, Ardem Patapoutian, Fan Wang, Chris Moore, HyunJae Pi, Nina Vogt, Andrew Rennekamp and many others.

I want to thank my graduate and college friends for their friendship and support. I want to specially thank Lola Fagbami and Le Cai, who have been like sisters taking care of me over the years.

Finally and most importantly, I'd like to thank my parents, Wenceng Zhang and Xinhua Fan, for their unconditional support, love, tolerance and confidence

in me. I also thank my boyfriend Lu for constant support and tolerance.

1

Introduction

Brain controls behavior through patterns of electrical activity traveling among neurons and circuits through synapses. Electrical activity across membrane in neurons and circuits display spatiotemporally rich behaviors such as adaptation[1], oscillation[2,3] and persistent activity[4,5] through a combination of voltage gated channels, depolarizing and hyperpolarizing synaptic input, and neuromodulatory input. A central goal of modern neuroscience[6] is to link the dynamics of neurons and circuits to behavior and to study what goes wrong in diseases: 1, how synaptic and cellular properties give rise to specific circuit dynamics

(from implementation to algorithm[7]); 2, how circuit dynamics relate to behavior (from algorithm to computational theory[7]); 3, what goes wrong pathologically in diseases. Ultimately, one would like to quantitatively describe the dynamics in mathematical models across different scales from synapse to behavior.

Cell-type-specific electrophysiological recordings and manipulations are highly desired to address these questions. Neurons are extremely diverse in terms of morphology, electrophysiology and gene expression pattern. New cell types are constantly being discovered, for example, in the cortex[8]. They are likely to exhibit different dynamics and execute different function in behavior. Therefore, cell-type-specific targeting is particularly important.

Electrophysiological recordings with electrode provide unparalleled temporal resolution and sensitivity allowing studies of even single channels[9], for instance with voltage clamp. However, it lacks spatial resolution, genetic specificity and longitudinal access. It is also invasive. Two-photon guided whole-cell patch clamp could be genetically targeted but to date, in awake behaving mice, it has only been simultaneously performed on two cells[10]. Recent advance on silicon probes allows recording of spikes on hundreds of cells[11]. However, it lacks spatial resolution and subthreshold resolution. It also lacks genetic specificity (however, see ref 12 for phototagging[12]). Furthermore, it is often hard to track the same set of neurons over time due to electrode drift (however, see ref 13 and 14 for soft electrodes[13,14]). Nevertheless, the Neuropixels probe[11] is likely

to revolutionize brain-wide distributed activity recording during behavior. For manipulation, electrical microstimulation lacks cell-type specificity and often could not be delivered with the same electrode for recording.

As a complement, optical recording of membrane potential with genetically encoded voltage indicators (GEVIs) provide unprecedented spatial resolution, genetic specificity and longitudinal access and it is noninvasive. GEVIs with fast kinetics provide high temporal precision. GEVIs with high sensitivity could follow subthreshold membrane potential dynamics comparing with extracellular recording. Optical imaging also allows high throughput measurement comparing with whole-cell patch clamp. Longitudinal recordings and manipulations over time are needed for studying longer time events such as learning and synaptic plasticity.

Furthermore, optical method allows multiplexing with simultaneous optical perturbation, providing a close loop understanding of the circuit basis of neural coding and behavior.

First, simultaneous optogenetic manipulation can reveal subthreshold hidden inhibition similarly as that in voltage clamp experiments. For example, Chapter 3 provides one example of revealing excitation and inhibition in cortical layer 1 neurons and suggests cortical layer 1 neurons function as a high pass filter. Similar methods can be used to test recurrent neuron network models of excitation and inhibition balance [15]. Meanwhile, many neuronal models including reinforcement learning model [16] and predictive coding [17] rely on subtracting inhibitory feedback

signals (eg, reward prediction) from excitatory input (eg, actual reward). However, experimental validations have not been shown yet. One could use simultaneous optogenetic manipulation and voltage imaging for untangling the excitation and inhibition in these neurons.

Second, even the same cell types canonically defined by gene expression patterns and morphology may show different neural activity pattern in the circuit in behavior. For instance, only sparse subset of the CA1 pyramidal neurons fire action potential in particular locations, namely place cells; they also show sequential activity during sharp-wave ripples[18]. Therefore, function-specific manipulation based on electrophysiological recording are desired. Vice versa, during behavior, multiple cell types may show ensembled activity pattern, again, requiring function-specific manipulation based on functional recording.

Third, simultaneous optical inhibition and voltage imaging will provide mechanistic understanding of the circuit computation and behavior. Inhibitory rhodopsins such as GtACR[19] could be combined with voltage imaging. One could imagine using voltage imaging to discover functional active neurons during behavior and then using optogenetic inhibition to reveal the necessity (for example, to study the causality of sharp-wave ripples).

Last, simultaneous optogenetic manipulation also allows circuit mapping and probing functional connectivity[20] in vivo.

For those above reasons, my PhD has been focused on developing simultaneous

optogenetic stimulation and optical voltage recording, revealing excitation and inhibition for modeling disease[21] and for dissecting circuit computation in vivo[22], and mapping functional connectivity in vivo[22]. As my PhD also witnessed the prosperous development of voltage imaging from primary culture to in vivo, here I first briefly overview the latest progress of GEVIs and optical engineering for voltage imaging. Then I present my work on all-optical electrophysiology of excitation and inhibition, a promising way for dissecting circuit computation at subthreshold level and testing network models.

1.1 GEVIs

The first GEVI, Flash, was developed in 1997, with a green fluorescent protein (GFP) inserted into the C terminal of the Shaker K+ channel[23]. Since then optimization have been conducted and new scaffolds have been explored. To date, the GEVIs are composed of two major families. The first family is based on voltage-sensing domain (VSD), including Arclight[24] and ASAP[25]. The rationale was to couple the conformational change of the VSD to fluorescence change of the fluorescent protein (FP) or circularly permuted FP. As it is based on the FP which is not embedded in the membrane, it is usually slower. The recent ASAP[26] are faster, with a fast component about 2 ms. This family of GEVIs show voltage dependent changes in fluorescence under two-photon illumination. To date, this

family of GEVIs have not been able to be combined with optogenetic actuators due to optical crosstalk as they spectrally overlap with optogenetic actuators, even nominally red-shifted variants[27–30]. However, recent genome mining identified a very sensitive red-shifted optogenetic actuator, ChRmine[31]. It may be possible to combine two photon imaging of ASAP with two photon stimulation of ChRmine.

The second family derives from microbial rhodopsins. In 2011, a green-absorbing proteorhodopsin (PROPS) was reported to function as a fluorescent voltage reporter in bacteria[32]. The fluorescence comes from the chromophore of retinal when it is protonated. The protonation-deprotonation equilibrium is voltage dependent as proton is charged. Therefore, the fluorescence is voltage dependent. Mutations are introduced to eliminate the natural pumping function. Further genome mining and screening yielded Arch[33], QuasAr[34] and Archon[35] for mammalian cells system. A big advantage of this family of GEVIs is that they can be readily combined with optogenetic stimulation as they are excited by red light and do not have optical crosstalk with optogenetic stimulation[34,21,36,22]. Chapter 2 and 3 are two examples of simultaneous voltage imaging with rhodopsin-derived GEVIs and optogenetic stimulation.

As retinal is intrinsically dim, one way to improve the brightness is through electrochromic Förster resonance energy transfer (eFRET) couple of the voltage dependent absorbance change of rhodopsin to a FP donor. This yielded QuasAr2-mOrange[37], MacQ-mOrange[38], Ace-mNeon[39] and Ace-mRuby[40]. Further swap

of the FP donor to the bright Janelia dyes yielded brighter version of GEVI, Voltron[41]. Mutation of the residues along the proton pump changed the direction of protonation yielding a positive responsive GEVI, Positron[42]. To date, only one version of these GEVIs were combined with optogenetic stimulation but with significant optical crosstalk[40].

1.2 Optics

Optical recording of membrane potential with GEVIs requires monitoring fast dynamics with high spatial resolution as action potential (AP) itself is intrinsically fast occurring on millisecond timescales. Optical manipulation of membrane potential with ChRs also requires high spatiotemporal resolution.

Unlike two dimensional monolayer primary culture, in vivo voltage imaging is more challenging due to tissue auto-fluorescence, light scattering and out-of-focus background.

1.2.1 Fast two photon microscopy for voltage imaging

Two-photon microscopy overcomes the light scattering by nonlinearly confining the excitation fluorescence only to a single point and collecting all the emitted photons by a single detector. Images are formed by raster scanning the sample. Two-photon microscopy also overcome the tissue auto-fluorescence as the brain

does not absorb much in the infrared wavelength window[43]. However, for two-photon voltage imaging, traditional raster scanning is too slow for detecting AP signals. This slow speed is due to galvanometer-based scanning and serial acquisition of the emitted photons.

For activity recording, one can achieve faster two photon imaging by scanning only regions of interest. Such methods include random-access scanning using acousto-optical deflectors which has been used for voltage imaging with ASAP[26,44]. Volumetric imaging by Bessel beam[45] and multi-plane imaging[46] also improve the imaging speed but require sparse activity for unmixing. These methods have not been used for voltage imaging. Recent scanned line angular projection microscopy[47] utilizes computational unmixing and can achieve imaging over 1kHz spanning hundreds of micrometers. It uses a 1030 nm laser providing high pulse energy. The wavelength is not optimal for ASAP imaging. By temporally stretching the ultrafast laser pulse for scanning fast across the sample plane, free-space angular-chirp-enhanced delay (FACED) reaches the limit imposed by fluorescence lifetime and has been used for voltage imaging[48]. However, it wastes time and energy onto samples that are not the target of interest.

1.2.2 Wide field microscopy for voltage imaging

Detection in wide field microscopy uses camera, which is much faster than serial acquisition of emitted photons in two photon microscopy, providing a unique

advantage for fast voltage imaging. The challenge however is scattering. The scattering length of visible photons are about 100 μm in brain tissue. Red photons (640 nm) have roughly $\sim$50% longer scattering length than blue photons (488 nm)[49]. Auto-fluorescence in brain tissue is much lower at in-fared photons than at 488 nm[43]. Therefore, for wide-field voltage imaging, far-red GEVIs are desired.

One could use structured illumination to overcome the background and scattering. For somatic voltage imaging in tissue, the signals arise solely from the neuronal membrane. Illumination that enters the tissue but misses the membrane of interest contributes to background fluorescence and heating, but not to signal. Excitation photons would most efficiently produce signal if targeted to the somatic membrane. One could achieve this through either digital micromirror device (DMD)[36] or spatial light modulator (SLM)[22]. SLM could provide higher efficiency of light usage and better optical sectioning when using high numerical aperture illumination (NA). Confocal-like excitation combined with spatially filtered emission would also minimize optical crosstalk from out-of-focus cells. Indeed, in Chapter 3, we characterized that holographic membrane-targeted illumination provided substantially better optical sectioning and signal-to-background ratio than did soma-wide illumination.

1.3 All-optical electrophysiology

As listed above, there are several motivations requiring the simultaneous optogenetic recording and voltage imaging.

In Chapter 2, I developed an all-optical synaptic assay for probing excitation and inhibition in primary culture, acute slices and human iPSC-derived neurons. I applied the method to primary cultured neurons and discovered the mechanism of ketamine-induced disinhibition.

In Chapter 3, I developed all-optical methods to dissect excitation and inhibition in cortical neurons in awake mice and applied the method to study how cortical layer 1 neurons process bottom-up sensory inputs and top-down signals. Chapter 3 shows how one could harness simultaneous voltage imaging and optical manipulation for dissection the circuit basis of neural coding in awake mice.

In Chapter 4, I propose possible development on optics for voltage imaging. I list considerations in improvement of GEVIs. I propose new types of measurements harnessing the techniques to test network models. I also specifically propose to study attention with the technique established in Chapter 3.

2

All-optical synaptic electrophysiology probes mechanism of ketamine-induced disinhibition

Optical assays of synaptic strength could facilitate studies of neuronal transmission and its dysregulation in disease. Here we introduce a genetic toolbox for all-optical interrogation of synaptic electrophysiology ('syn-Optopatch') via mutually exclusive expression of a channelrhodopsin actuator and an archaerhodopsin-derived voltage indicator. Optically induced activity in the channelrhodopsin-expressing neurons generated excitatory and inhibitory post-synaptic potentials which we optically resolved in reporter-expressing neurons. We further developed a yellow spine-targeted Ca^{2+} indicator to localize optogenetically triggered synaptic inputs. We demonstrated synOptopatch recordings in cultured rodent neurons and in acute rodent brain slice. In synOptopatch measurements of primary rodent cultures, acute ketamine administration suppressed disynaptic

inhibitory feedbacks, mimicking the effect of this drug on network function in both rodents and humans. We localized this action of ketamine to excitatory synapses onto interneurons. These results establish an in vitro all-optical model of disynaptic disinhibition, a synaptic defect hypothesized in schizophrenia-associated psychosis.

2.1 Introduction

Changes in synaptic strength underpin learning and memory, are the mechanism by which most neuropeptides[50] and neuromodulators[51] act, and contribute to the pathogenesis of many disorders. To study synaptic transmission and plasticity, a rapid, reliable and quantitative means to probe the strength of synapses in a neural circuit is desirable.

Such capabilities have remained elusive due to the difficulty of performing simultaneous electrophysiological measurements on defined pairs of neurons. Moreover, whole-cell patch clamp measurements can dialyze cellular components, possibly interfering with plasticity mechanisms.[52] It is also technically challenging to maintain patch clamp connections for long enough to probe long term plasticity.

Pairing of optogenetic actuation with fluorescence imaging[53] constitutes a suitable alternative. The technical challenges are to ensure that optogenetic stimuli are delivered only to the presynaptic cells, that readouts come only from the

postsynaptic cells, and that there is no optical crosstalk between stimulus and readout wavelengths. In the Optopatch technique,[34] cells co-expressed a blue light-activated channelrhodopsin, CheRiff, and a red light-excited voltage indicator, QuasAr. This technique enabled high-speed measurements of neuronal excitability in cultured neurons[54], acute brain slice, and peripheral nerves in vivo[55]. However, because the actuator and reporter are coexpressed, it may be difficult to distinguish synaptically mediated potentials from spurious optical stimulation of postsynaptic neurites that crossed the stimulus zone[56]. Here we describe an approach to achieve mutually exclusive expression of optogenetic actuators in presynaptic cells and voltage reporters in postsynaptic cells (synOptopatch). We further developed a spine-targeted yellow Ca^{2+} indicator, spine-jRGECO1a, which we combined with simultaneous synOptopatch measurements to probe the relation between synaptic Ca^{2+} and membrane voltage during sub- and supra-threshold activity. The synOptopatch technique functioned in primary cultured neurons and in acute brain slice. We developed pharmacological and genetic techniques to specify the sub-type of the presynaptic and postsynaptic cells.

We used synOptopatch to explore in vitro the mechanism of action of ketamine, a non-specific N-methyl-D-aspartate receptor (NMDAR) antagonist. In healthy subjects acute sub-anesthetic ketamine induced symptoms that mimicked both positive and negative symptoms of schizophrenia[57]. In rodents and in healthy humans ketamine induced elevated hippocampal glutamate and cortical

hyperexcitability[58–61]. In acute brain slices, ketamine decreased excitatory post-synaptic potential (EPSP) amplitudes in pyramidal neurons[62], as expected for an NMDAR blocker, but also decreased the amplitude of disynaptic inhibition[63]. The mechanism by which a blocker of excitatory neurotransmission enhances network excitability has not been conclusively established[64].

We found that ketamine had a dramatic dis-inhibitory effect in cultured neuronal networks. Combinations of Optopatch and synOptopatch measurements established that the dominant action of ketamine was to block excitatory-to-inhibitory synapses. These results demonstrate that synOptopatch can be used to dissect complex synaptically mediated phenomena.

2.2 Results

2.2.1 Cre-mediated mutually exclusive expression of QuasAr2 and CheRiff

To image membrane voltage we used QuasAr2-Citrine containing a triple repeat of the $K_{ir}2.1$ membrane trafficking signal[65,66]. When co-expressed with the channelrhopsin, CheRiff, in cultured rat hippocampal neurons, this genetically encoded voltage indicator (GEVI) reported optically evoked action potentials with signal-to-noise ratio (SNR) of 39 ± 3 in a 500-Hz bandwidth (n = 12 neurons, all statistics are mean ± s.e.m. unless specified), but targeted stimulation of individual cells sometimes caused spurious direct optical stimulation of dendrites

in a putative postsynaptic cell (Supplementary Fig. 1).

We developed a system based on Cre-recombinase[67] for mutually exclusive expression of CheRiff-CFP and QuasAr2-Citrine (**Figure 2.1**a). Cre-on CheRiff-CFP comprised a double-floxed inverse ORF (DIO) flanked by parallel double lox (loxP and lox2272) sites[68]. Cre-off QuasAr2-Citrine was flanked by a lox variant, FAS, which does not show cross-reactivity with loxP or lox2272 sites[69] (**Figure 2.1**a; Supplementary Fig. 2). Co-transduction of DIO Cre-on CheRiff-CFP, FAS Cre-off QuasAr2-Citrine and low-titer Cre virus led to mutually exclusive expression of the actuator and reporter (**Figure 2.1**b). The complete set of synOptopatch constructs is described in Supplementary Table 1.

Titration of the Cre virus tuned the ratio of actuator- to reporter-expressing neurons, from 0.07 at a Cre titer of 0.1 multiplicity of infection (MOI) to 8.3 at a Cre titer of 10 MOI, allowing control of the relative sizes of the pre- and post-synaptic populations (**Figure 2.1**c). We proceeded with a Cre titer of 1 MOI, corresponding to a 1.1:1 ratio of actuator- to reporter-expressing neurons. Mean expression levels per expressing neuron of the CheRiff-CFP and QuasAr2-Citrine depended on the titers of the corresponding lentiviruses, but did not depend on the titer of the Cre virus, which suggests that a single copy of the Cre virus per cell was probably sufficient to activate expression of all CheRiff genes and inactivate expression of all QuasAr2 genes (Supplementary Fig. 2g). In analysis of 324 neurons across a range of titers of each of the three constructs, we did

not observe any cells co-expressing CheRiff-CFP and QuasAr2-Citrine, confirming the orthogonality of the gene expression system (Supplementary Fig. 2h).

2.2.2 SynOptopatch enables all-optical measures of synaptic transmission

We delivered wide-field flashes of blue light (488 nm, 20 - 120 mW/cm^2, 10 ms, repeated at 1 Hz) to evoke spikes in the CheRiff-expressing neurons. The blue illumination covered a circular area 280 μm in diameter, typically encompassing 2.6 ± 0.3 CheRiff-expressing neurons (n = 10 fields of view), though not every CheRiff-expressing neuron necessarily synapsed onto each postsynaptic cell. We recorded the postsynaptic responses in the QuasAr2-expressing neurons via red excitation (640 nm, 400 W/cm^2, 500 Hz frame rate) and near-infrared fluorescence. Simultaneous manual patch clamp measurements provided ground-truth on the postsynaptic potentials in n = 10 neurons (**Figure 2.1**d).

We observed a variety of responses, including purely excitatory, purely inhibitory, and mixed excitatory and inhibitory post-synaptic potentials (PSPs), with close correspondence of the optical and electrical traces (Supplementary Fig. 3a,b) reflecting the linearity and speed (1.2 ms response time) of the QuasAr2 GEVI[34]. The mean EPSP amplitude was 22 ± 10 mV (n = 6 neurons) and the mean IPSP amplitude was -6 ± 2 mV (n = 4 neurons). The mean slope of the F vs. V relation was 45 ± 6% $\triangle$F/F per 100 mV, where the error represents the standard error of a fit to n = 10 cells (Supplementary Fig. 3c). Shot noise and camera

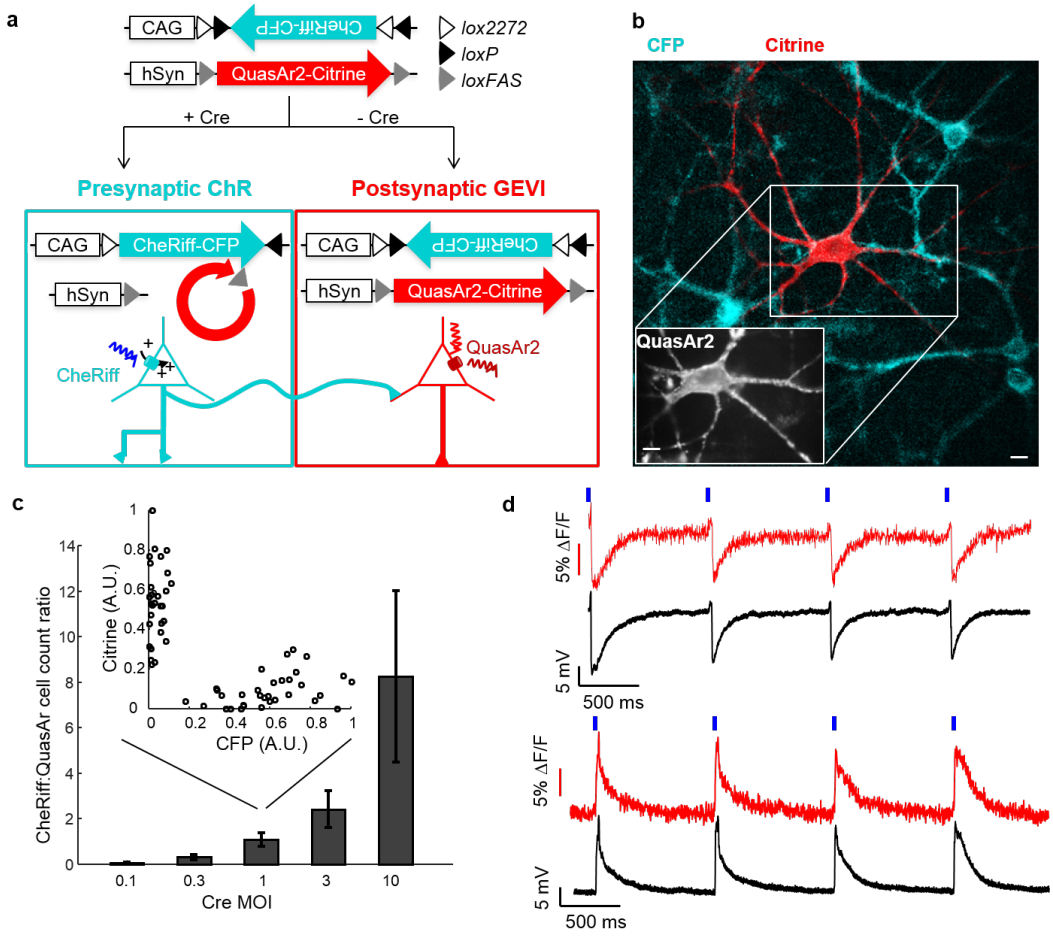

Figure 2.1: All-optical assay of synaptic function. (**a**) Scheme for Cre recombinase-mediated exclusive expression of Cre-on CheRiff and Cre-off QuasAr2. (**b**) Green: presynaptic cell expressing CheRiff-CFP. Red: postsynaptic cell expressing QuasAr2-Citrine (Citrine fluorescence; Inset: QuasAr2 fluorescence). Scale bars: 10 μm. (**c**) Ratio of cells expressing CheRiff to QuasAr2 as a function of MOI of AAV virus encoding Cre. Error bars represent standard deviation calculated by bootstrap method. Inset: At MOI = 1, approximately equal numbers of neurons expressed CheRiff or QuasAr2, but no cells expressed both (n = 63 neurons). (**d**) Optical initiation and monitoring of primarily inhibitory (top) and primarily excitatory (bottom) postsynaptic potentials. These measurements were performed without synaptic blockers and may contain minor contributions from both excitatory and inhibitory inputs (for example, slight uptick in top recording). Blue, 10 ms blue light stimulation; red, whole-cell single-trial unfiltered fluorescence; black, patch-clamp recording.

noise together contributed a mean noise of 0.8% $\Delta F/F$ (corresponding to 1.8 mV) in a 500 Hz bandwidth.

To test for optical crosstalk, we measured the effect of blue light on QuasAr2 in cultures not expressing a channelrhodopsin (Supplementary Fig. 3d-f). QuasAr2 did not generate detectable photocurrent under red light (400 W/cm^2), blue light (120 mW/cm^2), or both. The blue light led via direct QuasAr2 fluorescence to transients of 1.5% $\Delta F/F$, which were readily distinguished from true postsynaptic responses by their rapid rise and fall concurrent with the blue stimulus.

To test the long-term stability of the cultures, we optogenetically evoked and probed PSPs before and after a 2-hr interval during which the sample sat on the microscope stage. We did not observe a systematic change in the PSP response (n = 14 neurons, peak timing, p = 0.8, two-sided paired-sample t-test; area under the curve (AUC), p = 0.8, two-sided paired-sample t-test, Supplementary Fig. 3g). To test for photodamage, we illuminated a sample with continuous red light at 400 W/cm^2. The signal photobleached to 50% of initial intensity in 29 min, but we did not observe a change in the PSP waveform during a 30 min exposure. (Supplementary Fig. 3h,i).

The synOptopatch technique enabled repeated measurements on the same cells over several days. Chronic incubation with gabazine (20 μM, 48 hrs) followed by wash-out led to a homeostatic increase in the ratio of inhibitory to excitatory PSPs (IPSP:EPSP amplitude, 0.080 ± 0.03 before gabazine vs 0.23 ± 0.05 after gabazine,

n = 9 neurons, p = 0.04, two-sided paired-sample t-test), whereas control plates showed no significant change in PSP over 48 hrs (IPSP:EPSP amplitude, 0.091 ± 0.03 before vs 0.099 ± 0.01 after 48 hrs, n = 5 neurons, p = 0.76, two-sided paired-sample t-test, Supplementary Fig. 4).

The synOptopatch constructs reported EPSPs and spikes in human induced pluripotent stem cell (hiPSC)-derived neurons (Supplementary Fig. 5), although the signal-to-noise ratio was lower than in primary neurons due to low expression of the optogenetic constructs, and further improvements will probably be required for use in disease-modeling applications.

2.2.3 Resolving presynaptic cell types with pharmacology

Considering the complexity of neural circuits, we sought to isolate specifically excitatory versus inhibitory signals. SynOptopatch measurements in n = 403 cultured rat hippocampal neurons revealed pure EPSPs in n = 301 neurons (75%), pure IPSPs in n = 17 neurons (4%), and a mixed excitatory and inhibitory response in n = 85 neurons (21%, **Figure 2.2**a). The mixed responses were presumably due to co-activation of excitatory and inhibitory pre-synaptic neurons. Indeed we occasionally observed postsynaptic responses with intermittent inhibitory components, indicative of stochastic activation of an inhibitory presynaptic neuron (**Figure 2.2**b). Targeted stimulation of individual presynaptic neurons using patterned blue light resolved mixed postsynaptic responses into individual excitatory

and inhibitory components, confirming the presence of multiple presynaptic neurons (**Figure 2.2**c).

We sought a pharmacological means to isolate the contributions of distinct presynaptic cell types and postsynaptic receptors to the PSP. Picrotoxin (50 μM) eliminated the inhibitory components of the PSP (**Figure 2.2**d), (2R)-amino-5-phosphonovaleric acid (AP5) (50 μM) eliminated the slow NMDAR-dependent part of the EPSP while preserving the fast α-amino-3-hydroxy-5-methyl-4-isoxazolepropionic acid receptor (AMPAR)-dependent component (**Figure 2.2**e), and 2,3-dihydroxy-6-nitro-7-sulfamoyl-benzo[f]quinoxaline (NBQX) (20 μM) eliminated both the fast and slow excitatory components (**Figure 2.2**f). In neurons with mixed presynaptic inputs, sequential application of each of these three blockers isolated the respective contributions to the PSP (**Figure 2.2**g).

We ascribed the suppression by NBQX—an AMPAR blocker—of the putative NMDAR-dependent slow component of the EPSP to the voltage-dependent Mg2+ block of NMDARs, i.e. without AMPAR-mediated depolarization, the NMDARs did not activate. Optogenetic induction of presynaptic spikes in a medium containing 0 mM Mg2+, NBQX (20 μM) and picrotoxin (50 μM) restored the slow NMDAR component of the PSP, but not the fast AMPAR component, confirming this hypothesis (Supplementary Fig. 6). Although other blockers could be used to achieve finer segmentation of postsynaptic responses by receptor sub-types, the above examples demonstrate the broad flexibility of synOptopatch for dissecting

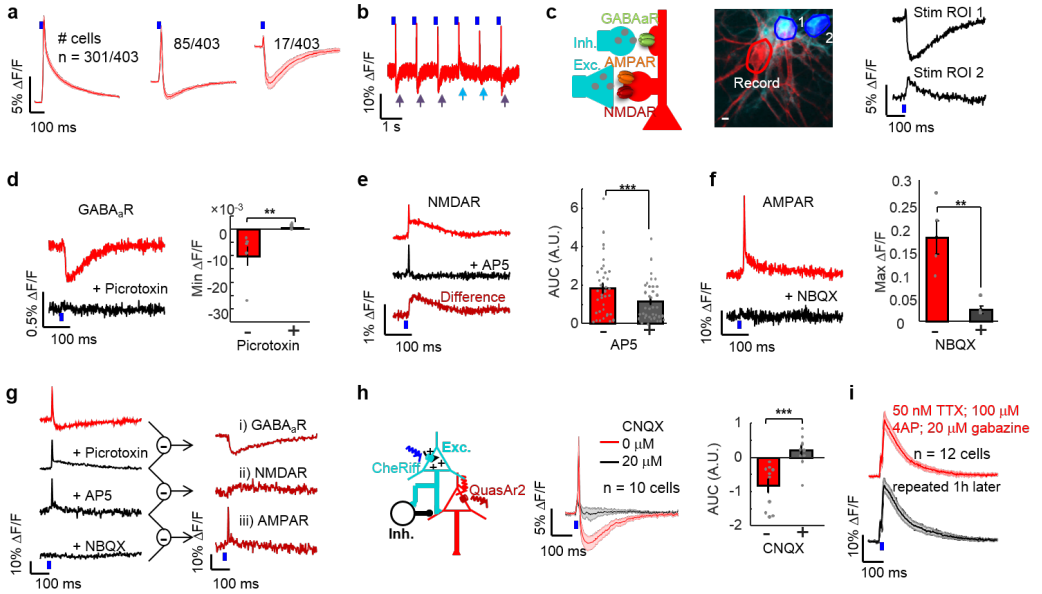

Figure 2.2: Pharmacological dissection of synaptic transmission and genetic tagging of inhibitory neurons. (**a**) In the absence of drugs, cells showed purely excitatory, mixed excitatory and inhibitory, and purely inhibitory PSPs. (**b**) Example single-cell single-trial trace showing intermittent optically evoked IPSPs (purple arrows) and IPSP failures (blue arrows). (**c**) Left: Schematic showing excitatory and inhibitory synaptic inputs into a single cell. Middle: green: CheRiff-CFP, red: QuasAr2-Citrine, blue: DMD masks for patterned blue light stimulation. Right: Stimulation of ROI 1 evoked a pure IPSP and of ROI 2 evoked a pure EPSP. Two-trial average. Scale bar 10 μm. (n = 3 times; representative data are shown) (**d**) Optogenetically triggered IPSP (red) was blocked by picrotoxin (50 μM; black; five-trial average). Bottom: quantification of minimum of $\Delta F/F$ before and after addition of picrotoxin. (-0.99% $\pm$ 0.37% vs -0.02% $\pm$ 0.02%, n = 6 neurons, **p = 0.04, two-sided paired-sample t-test) (**e**) NMDAR blocker AP5 (50 μM) blocked slow component of EPSP (red: before; black: after AP5 addition; dark red: difference; five-trial average). Bottom: quantification of maximum of $\Delta F/F$ before and after addition of NBQX and AP5. (1.86 $\pm$ 0.25 vs 1.19 $\pm$ 0.17, n = 36 neurons, ***p = 2$\times$10-6, two-sided paired-sample t-test). (**f**) AMPAR blocker NBQX (20 μM) blocked EPSPs (red: before; black: after NBQX addition; five-trial average). Bottom: quantification of maximum of $\Delta F/F$ before and after addition of NBQX. (17.94% $\pm$ 3.58% vs 2.48% $\pm$ 0.08%, n = 4 neurons, **p = 0.035, two-sided paired-sample t-test) (**g**) Pharmacological dissection of a mixed EPSP and IPSP. The cell was recorded following sequential addition of picrotoxin (50 μM), AP5 (50 μM) and NBQX (20 μM). Five-trial average. (n = 3 times; representative data are shown). (**h**) Left: Schematic showing network inhibition. Middle: In cells with mixed excitatory/inhibitory PSPs, blockade of excitatory transmission with CNQX (20 μM; black) relieved inhibition (red). Right: quantification of AUC before and after addition of CNQX. (-0.80 $\pm$ 0.24 vs 0.19 $\pm$ 0.17, n = 10 neurons, ***p = 0.001, two-sided paired-sample t-test). (**i**) 50 nM TTX, 100 μM 4-AP allowed detection of monosynaptic transmission (red). Signals were stable after 1 h under repeated measurements (black; n = 12 neurons). All shaded error bars and error bars, s.e.m.

mechanisms of synaptic transmission.

We next probed whether IPSPs were primarily driven by direct optogenetic stimulation of inhibitory neurons versus an E-to-I disynaptic mechanism (**Figure 2.2**h). In cells that showed mixed excitatory and inhibitory PSPs, addition of 6-cyano-7-nitroquinoxaline-2,3-dione (CNQX) (20 μM), an AMPAR blocker, abolished both the excitatory and inhibitory components of the PSP in 8 of 10 neurons tested, establishing that the IPSP was predominantly driven through a disynaptic (or polysynaptic) mechanism (**Figure 2.2**h).

To measure purely monosynaptic PSPs, we adapted a protocol previously developed for optogenetic mapping of synaptic connections in brain slice[70]. Tetrodotoxin (TTX) (50 nM) blocked network activity, 4-aminopyridine (4-AP) (100 μM), a non-specific potassium channel blocker, enabled the membrane potential to float, and gabazine (20 μM) blocked inhibitory signals. Optogenetic stimulation then evoked large monosynaptic EPSPs which were stable for > 1 hr (n = 12 neurons, **Figure 2.2**i).

2.2.4 Resolving active spines with spine-jRGECO1a

We next imaged spine-localized Ca^{2+} to probe the specific synapses activated during optogenetically induced synaptic transmission. GCaMP6s has previously been used to probe Ca^{2+} accumulation in individual synaptically activated dendritic spines under high magnification imaging[71], but this indicator is not spectrally

compatible with one-photon optogenetic stimulation. Although red-shifted Ca^{2+} indicators fulfill this requirement[72], under wide-field imaging conditions it was difficult to separate spine-specific signals from the much brighter background from the parent dendrite.

We therefore developed spine-enriched versions of the jRGECO1a[72] and GCaMP6s Ca^{2+} indicators. Dendritic spines contain high concentrations of filamentous actin, which has been used as a spine marker[73]. The calponin homology domain of rat Utrophin (Utr; amino acids 1-261), binds to actin filaments[74] and at low concentration does not perturb their dynamics. We fused jRGECO1a and GCaMP6s to Utr and drove expression with a transcriptional regulatory system that used negative feedback to minimize levels of untargeted probe (**Figure 2.3**a). High-resolution images showed that neurons expressing the complete construct had lower levels of dendritic background than did neurons expressing a construct lacking the transcriptional regulatory system (Supplementary Fig. 7)[75]. Immunostaining for PSD-95 confirmed spine localization of the reporter (Supplementary Fig. 7). We compared the Ca^{2+} response of the jRGECO1a-Utr and cytosolic jRGECO1a in HEK cells. Ca^{2+} transients induced by addition of ionomycin (10 μM) were indistinguishable between the two constructs (ΔF/F 1.6 ± 0.1 vs. 1.5 ± 0.07, n = 26 cells for jRGECO1a-Utr, n = 29 for cytosolic jRGECO1a, p = 0.4, student's t-test). Supplementary Fig. 7). For both the spine-jRGECO1a and spineGCaMP6s indicators, we observed flickering patterns throughout the dendritic

arbor, indicative of asynchronous activation of individual spines by synaptic inputs, as well as near-synchronous activation of many spines by back-propagating action potentials (Supplementary Videos 1 and 2).

We then combined optogenetic stimulation of presynaptic inputs with simultaneous imaging of dendritic spine Ca^{2+} and somatic voltage. This measurement required several modifications to the synOptopatch constructs and to the optical setup. We developed a bicistronic construct to drive co-expression of spine-jRGECO1a and QuasAr2-dark Citrine5 (a non-fluorescent Citrine variant, Supplementary Fig. 8a). To minimize spurious activation of CheRiff by the yellow light used for jRGECO1a imaging, we fused CheRiff with a trafficking motif derived from KV2.1, to localize expression to the soma[77], and we used a digital micromirror device (DMD) to pattern the yellow illumination to span the dendritic arbor of the postsynaptic cell while avoiding presynaptic CheRiff-expressing somas (**Figure 2.3**b). A dichroic beam splitter in the emission path separated the QuasAr2 from the spine-jRGECO1a emission, sending each to a separate camera (Supplementary Fig. 8b).

Wide-field blue light stimuli (488 nm, 200 mW/cm^2, 10 ms duration, repeated at 0.5 Hz) triggered presynaptic spikes, which in turn evoked somatic PSPs (detected with QuasAr2 fluorescence) and synchronous Ca^{2+} transients in a subset of postsynaptic spines (**Figure 2.3**b, c, Supplementary Fig. 9a,b). On average, we observed 8 ± 3 spines activated per stimulus (mean ± s.d, n = 5 neurons,

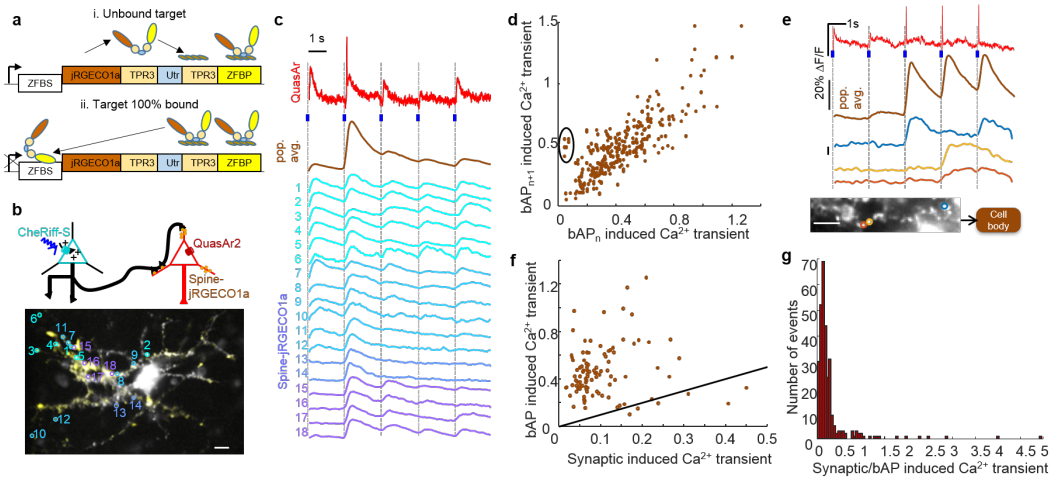

Figure 2.3: Simultaneous presynaptic optogenetic stimulation, spine Ca^{2+} imaging and somatic voltage imaging. (**a**) Design of spine-targeted jRGECO1a. (i) TPR3 linkers[76]: linked jRGECO1a, calponin homology domain of Utrophin (Utr), and a zinc finger DNA binding protein (ZFBP). (ii) Upon saturation of actin binding of spine-jRGECO1a, unbound protein accumulated in the nucleus where it bound the zinc finger binding site (ZFBS) downstream of the transcriptional start site and thereby blocked transcription. (**b**) Top: Schematic showing three color imaging with blue light excitable soma-localized CheRiff in presynaptic cells, yellow light excitable spine-jRGECO1a and red light excitable QuasAr2 co-expressed in postsynaptic cells. Bottom: spine-jRECO1a channel overlaid with active spines colored in yellow. Active spines are circled and numbered with correspondingly colored traces in (c). (**c**) Blue: 10 ms blue light stimulation of soma-localized CheRiff. Red: QuasAr2 fluorescence. Orange: population average of spine-jRGECO1a fluorescence over all the spines. Cyan-purple: spine-jRGECO1a fluorescence in individual spines. Dashed lines mark stimulus times. (**d**) Scatter plot of spine Ca^{2+} transients (ΔF) in pairs of successive bAPs. Transient amplitudes were predominantly correlated between events (R2 = 0.66, n = 100 spines, 3 bAPs) but some spines showed failures on some events (circled). (**e**) bAP failure in spines. Blue: 10 ms blue light stimulation of soma-localized CheRiff. Red: QuasAr2 fluorescence; orange: population average of spine-jRGECO1a over all the spines. Bottom: three spines on the same dendritic branch showed occasional bAP failures. (**f**) Scatter plot of bAP induced Ca^{2+} transients vs. PSP induced Ca^{2+} transients (R2 = 0.005, n = 100 spines). Black line indicates slope 1, corresponding to equal magnitude. (**g**) Histogram of the ratio of Ca^{2+} transient amplitudes driven by bAPs vs. synaptic events. All scale bars 15 μm.

Supplementary Fig. 9b). Occasionally, blue light stimulation triggered postsynaptic APs, which led to brief spikes in QuasAr2 fluorescence and concurrent whole-cell Ca^{2+} transients (**Figure 2.3**c, d, Supplementary Fig. 9a,b).

Simultaneous recording of spine Ca^{2+} and membrane voltage enabled detailed explorations of single-spine dynamics under both sub- and supra-threshold conditions. As expected, there was a positive correlation between the total synaptic Ca^{2+} transient and somatic PSP amplitude (Supplementary Fig. 9c, n = 14 events, R2 = 0.42, p = 0.01). Due to the simultaneous activation of multiple spines it was not possible to apportion the PSP voltage to contributions from individual spines.

We next studied how the back-propagating APs (bAPs) modulated spine Ca^{2+} levels. We observed strong bAP-to-bAP correlation in the bAP-induced Ca^{2+} amplitude at the level of single spines (Fig. 3d, R2 = 0.66, n = 100 spines). Remarkably, a small portion of spines (4 of 100) did not exhibit Ca^{2+} transients for some bAPs, while responding to others (Fig. 3e). While the mechanism underlying these failures is not known, we can rule out bAP failure in the parent dendritic branches because we observed bAP activation of spines distal to spines with bAP failures (**Figure 2.3**e, Supplementary Fig. 9d).

Finally, we studied the correlation between synaptically induced spine Ca^{2+} transients and bAP-induced transients. The correlation was much weaker than the bAP-to-bAP correlation, (R2 = 0.005, n = 100 spines) presumably reflecting the

different mechanisms driving synaptic vs. bAP spine Ca^{2+} transients (**Figure 2.3**f). For a small fraction of spines (6 of 100) the synaptic Ca^{2+} transient exceeded the magnitude of the bAP transient, again possibly reflecting bAP failure in a subset of spines (**Figure 2.3**f, g). These observations illustrate how the combination of synOptopatch with spine-jRGECO1a provides a platform for explorations of the interaction of voltage and calcium signals in single-spine dynamics.

2.2.5 SynOptopatch in acute brain slices

We next measured somatic PSPs in acute brain slices. To minimize non-specific GEVI fluorescence from neuropil, we previously developed a somatically localized QuasAr variant with improved trafficking in vivo. This variant, QuasAr2s, reported action potentials in acute brain slices with high signal-to-noise ratio[65].

We validated synOptopatch in visual cortex, using an Rbp4-Cre[78] driver to target expression of virally delivered Cre-on QuasAr2s-Citrine to a subset of L5 neurons. Cre-off CheRiff-CFP was expressed broadly, but not in the QuasAr2s-expressing neurons (**Figure 2.4**).

To minimize the background fluorescence in the QuasAr channel, we patterned the red illumination with a digital micromirror device (DMD) to illuminate expressing somas only[65]. Wide-field blue light stimulation (50 mW/cm^2, 5 ms, repeated at 1 Hz, 330 μm on a side) induced EPSPs, and sometimes spikes, that were readily detected on a single-trial basis (**Figure 2.4**d). Addition of NBQX (10

μM) and 3-((R)-2-carboxypiperazin-4-yl)-propyl-1-phosphonic acid (CPP) (10 μM) eliminated the fluorescence transients in the QuasAr2-expressing cells, confirming that the signals were due to synaptic transmission (**Figure 2.4**d, e).

Only one in 14 cells showed an IPSP, which was eliminated by gabazine (**Figure 2.4**f). We hypothesized that the rarity of inhibitory signals arose because the reversal potential for Cl^-, the main ion transported by gamma-aminobutyric acid (GABAA) receptors, was close to the resting potential in most cells. In patch clamp measurements, the membrane potential and intracellular chloride concentration are typically set by the patch pipette to reveal inhibition[79]. Lacking control of these parameters, we instead increased the extracellular K^+ concentration from 2.5 to 5 mM, raising the resting voltage by an estimated 14 mV[80]. Under high K+, NBQX (10 μM) and CPP (10 μM), blue light stimulation induced clear IPSPs in 8 of 10 cells (**Figure 2.4**g, Supplementary Fig. 10). Of these responding cells, some (5 of 8) also showed spontaneous activity, which was transiently suppressed by blue light stimulation. These results demonstrate the feasibility of all-optical assays for inhibitory transmission in acute brain slice.

2.2.6 SynOptopatch dissection of ketamine-induced disinhibition

We used the robust disynaptic inhibition in cultured networks (**Figure 2.2**h) to explore the mechanism of ketamine-induced disinhibition. In cultured rat hippocampal neurons, we measured PSPs before and after applying 50 μM ketamine.

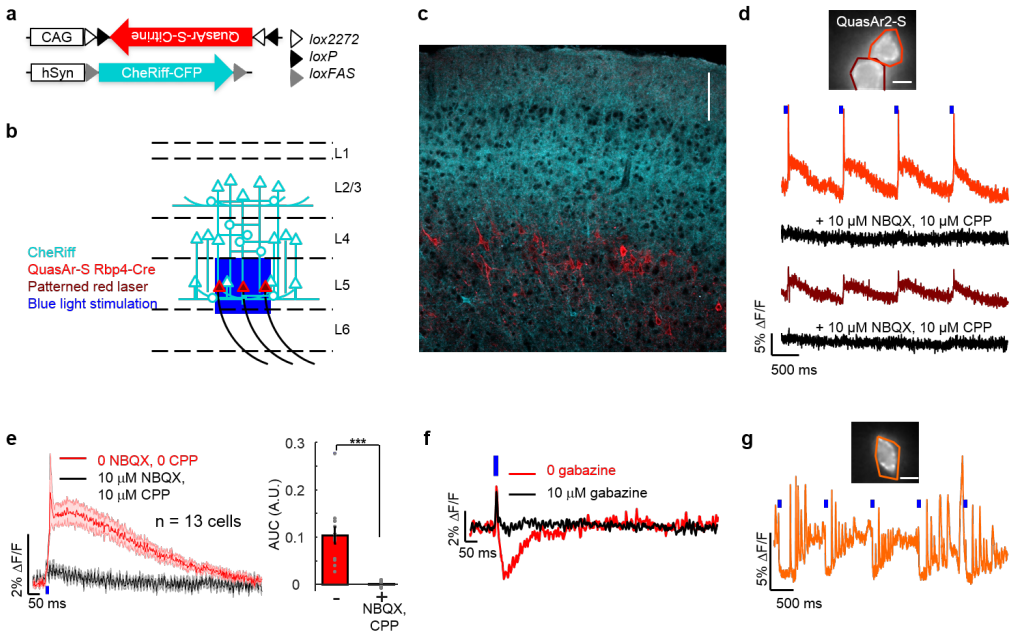

Figure 2.4: SynOptopatch detected EPSPs and IPSPs in acute mouse brain slice. (**a**),(**b**) Schematic showing experimental design. Rbp4-Cre mice were injected with hSyn-Cre-off CheRiff-CFP and CAG-Cre-on soma-localized QuasAr (QuasAr-S) leading to QuasAr-S expression in Layer 5 pyramidal neurons and CheRiff expression throughout the cortex. (**c**) Confocal image of a fixed brain slice. Scale bar 100 μm. (n = 3 times; representative data are shown). (**d**) Top: Fluorescence of QuasAr-S. Bottom: fluorescence traces of the two circled cells before (red) and after (black) addition of NBQX (10 μM) and CPP (10 μM). (n = 13 cells; representative data are shown). (**e**) Average PSPs of 13 cells before (red) and after NBQX and CPP (black). Shaded error bars, s.e.m. Right: quantification of AUC before and after addition of NBQX and CPP (0.1 $\pm$ 0.017 A.U. vs 0.002 $\pm$ 0.002 A.U., n = 13 neurons, ***p = 1×10^{-4}, two-sided paired-sample t-test). (**f**)IPSP before (red) and after 10 μM gabazine (black). Five-trial average. (n = 1 in 14 cells). (**g**) Single-trial IPSP detected under elevated (5 mM) extracellular K+ and 10 μM NBQX, 10 μM AP5. Scale bars in (d, g): 10 μm. (n = 8 cells; representative data are shown). All statistics are mean $\pm$ s.e.m.

For cells with purely excitatory inputs, ketamine suppressed the slow NMDAR component (AUC decreased from 1.08 ± 0.08 to 0.73 ± 0.05 A.U., n = 143 neurons, p = 2×10-6, two-tailed t-test; **Figure 2.5**a, b), as expected for an NMDAR blocker. In cells with mixed excitatory and inhibitory inputs, ketamine largely abolished the IPSP (AUC increased from -6.1 ± 0.8 to 0.7 ± 1.2 A.U., n = 56 neurons, p = 3×10-6, two-tailed t-test; **Figure 2.5**c, d). Thus acute ketamine administration in vitro largely suppressed inhibitory feedbacks, consistent with data from acute brain slices[63].

We reasoned that ketamine-induced disinhibition could come from: 1) blockade of E-to-I synapses; 2) decreased intrinsic excitability of inhibitory neurons; 3) increased excitability of excitatory neurons; or 4) blockade of I-to-E synapses (**Figure 2.5**e). We conducted optogenetic experiments to test each hypothesis independently.

To determine the identity of the postsynaptic neurons we used an enhancer derived from the mouse Dlx1 and Dlx2 transcription factors, mI12b, to drive expression of eGFP in inhibitory neurons[81–83]. We confirmed via immunostaining, Optopatch, and synOptopatch measurements that the enhancer drove expression in an inhibitory sub-population (Supplementary Fig. 11).[84,85]

To study the effect of ketamine on monosynaptic excitatory transmission, we performed measurements in the presence of TTX and 4-AP (to block polysynaptic transmission) and gabazine (to block inhibitory transmission). We used mI12b-

eGFP to distinguish postsynaptic responses in excitatory vs. inhibitory neurons and measured each postsynaptic cell before and after ketamine addition. Ketamine blocked E-to-I transmission significantly more strongly than E-to-E transmission, as measured by the slope of the plot of postsynaptic AUC after ketamine vs. before ketamine (inhibitory postsynaptic neurons, slope, 0.32 ± 0.05, n = 10 neurons; excitatory postsynaptic neurons, slope, 0.52 ± 0.04, n = 17 neurons; ANCOVA analysis of inhibitory vs. excitatory postsynaptic neurons, p = 0.001, **Figure 2.5**f). These findings are consistent with the prevailing model that E-to-I transmission is a strong site of ketamine action.

To study the effect of ketamine on intrinsic excitability, we co-expressed CheR-iff and QuasAr2-dark Citrine in the same cells (the 'Optopatch' configuration), and used ml12b-eGFP to identify neuron sub-types. Under a wide variety of optogenetic stimulus patterns, ketamine did not significantly affect spike rate or action potential waveform in either inhibitory or excitatory neurons (**Figure 2.5**g). Thus ketamine is unlikely to exert its disinhibitory effect by modulating intrinsic excitability of either excitatory or inhibitory neurons. To investigate the effects of ketamine on GABAergic synapses, we added NBQX and AP5 to block excitatory transmission. Regression fit showed ketamine slightly but significantly increased the AUC of GABAergic synaptic transmission (n = 11 neurons, R2 = 0.8, p = 2×10-4, F-test) (**Figure 2.5**h), by slowing the kinetics of GABAergic synaptic transmission (**Figure 2.5**i). This effect is consistent with prior observations in acute slice[86], but

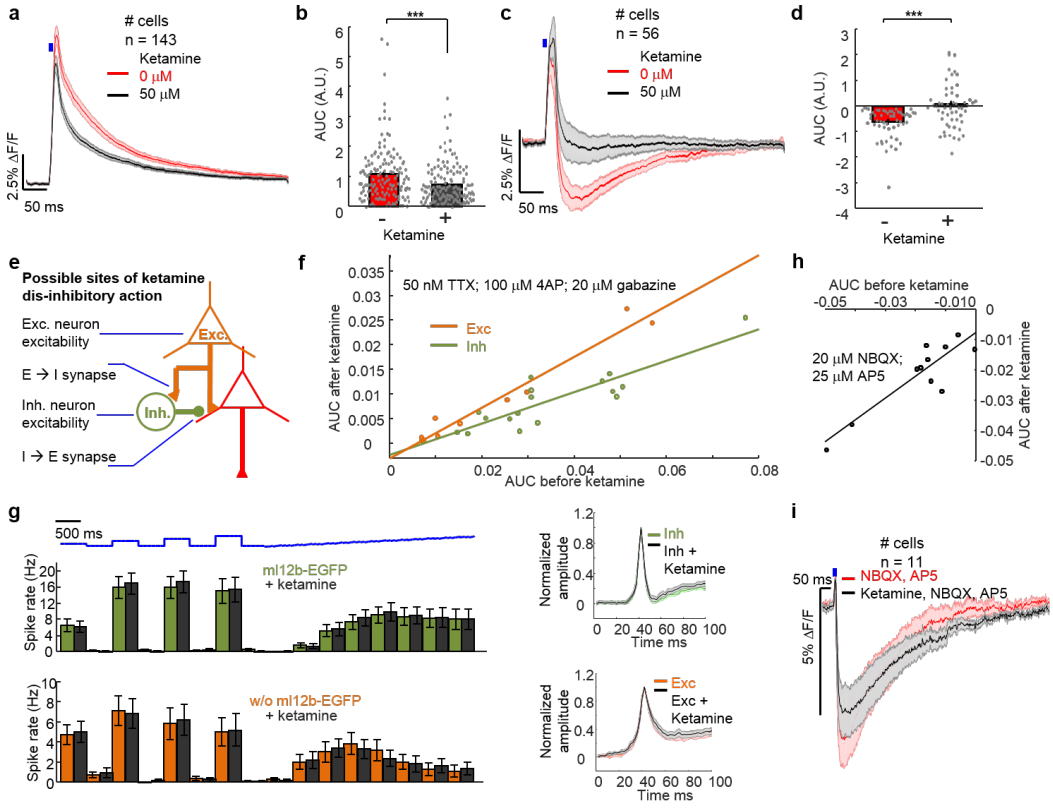

Figure 2.5: Mechanistic analysis of ketamine-induced disinhibition. (**a**) For cells with pure EPSPs (red), ketamine (50 μM, black) decreased the slow component of the EPSP (n = 143 neurons). (**b**) Quantification of the AUC in (a) (***p = 2×10^{-6}, two-tailed t-test). (**c**) For cells with mixed EPSP and IPSP, the mean IPSP decreased after ketamine addition (n = 56 neurons). (**d**)Quantification of AUC in (b). (***p = 3×10^{-6}, two-tailed t-test). (**e**) Possible sites of ketamine disinhibitory action: glutamatergic synapses onto inhibitory neurons; intrinsic excitability of excitatory or inhibitory neurons; GABAergic synapses. (**f**) Under conditions of monosynaptic excitatory transmission (50 nM TTX, 100 μM 4-AP, 20 μM gabazine), ketamine (50 μM) induced a larger decrement in the EPSP in inhibitory neurons (green, n = 17 neurons) than in excitatory neurons (orange, n = 10 neurons). ANCOVA analysis comparing the slopes, p = 0.001. (**g**) Left: In inhibitory neurons (green) the mean firing rate during a series of optogenetic stimuli was 12.9 $\pm$ 2.2 Hz before ketamine and 13.4 $\pm$ 2.2 Hz after ketamine (n = 27 neurons, p = 0.86). In excitatory neurons (orange) the mean firing rate was 5.1 $\pm$ 1.1 Hz before ketamine and 5.1 $\pm$ 1.1 Hz after ketamine (n = 22 neurons, p = 0.98). Right: In inhibitory neurons (green) the mean AP width before ketamine was 6.9 $\pm$ 0.3 ms, and after ketamine it was 6.8 $\pm$ 0.3 ms (n = 27 neurons, p = 0.81, two-sided paired-sample t-test). In excitatory neurons (orange) the mean AP width before ketamine was 9.3 $\pm$ 0.5 ms, and after ketamine it was 8.2 $\pm$ 0.8 ms (n = 22 neurons, p = 0.30, two-sided paired-sample t-test). (**h**) Effect of ketamine on inhibitory transmission. IPSPs were probed in the presence of NBQX (20 μM) and AP5 (25 μM). Regression fit of AUC before and after ketamine of inhibitory synaptic transmission (slope = 0.72 $\pm$ 0.12, R2 =0.8, n = 11 neurons). (**i**) Red: IPSP before ketamine. Black: IPSP after ketamine. All shaded error bars and error bars, s.e.m. All statistics are mean $\pm$ s.e.m.

is of the wrong sign and too small to account for the overall dis-inhibitory effect of ketamine.

Together, these results show that the disinhibitory action of ketamine is primarily via blockade of E-to-I transmission. More importantly these results demonstrate a robust in vitro all-optical assay of disynaptic inhibition, a core circuit function that is hypothesized to be dysregulated in schizophrenia-associated psychosis[64].

2.3 Discussion

The combined voltage and Ca^{2+} measurements revealed phenomena which merit further exploration. Although the mechanism of bAP failure in dendritic spines is unknown, we speculate that this effect may arise in spines where the neck electrical resistance is large compared to the membrane resistance of the spine head, leading to significant attenuation of the bAP amplitude in the spine, and therefore failure to activate voltage-gated Ca^{2+} channels.

A specific action of ketamine on E-to-I synapses has been hypothesized[64], but our experiments localize the disinhibitory effect to these synapses. Though parvalbumin interneurons express more NR2A and NR2C than do pyramidal neurons[87,88], heterologously expressed NMDAR subunits show little difference in ketamine sensitivity between subunits[89]. Furthermore, the concentration of ketamine used in this study, 50 μM, was far beyond the IC50 reported for

heterologously expressed NMDARs (0.5 – 0.7 μM)[89]. Thus the selectivity for E-to-I synapses likely comes from the fact that NMDARs contribute more to the EPSP in fast-spiking interneurons than in excitatory neurons[90]. These findings highlight the importance of measuring the functional effects of channel block in the neuronal context and not just on heterologously expressed channels.

We anticipate that the synOptopatch toolkit will be useful across a range of neuroscience applications, though some applications remain challenging. Direct measurements of spine voltage in primary neurons or acute slices will require improvements in sensitivity of the voltage indicator. Measurements of minis (PSPs induced by single vesicle releases) are also beyond the sensitivity of the existing indicators.

The acute slice measurements open the door to all-optical circuit mapping. In the present work, the GEVI expression was set by expression of the Cre recombinase, while the CheRiff expression was excluded from the Cre-expressing cells but not otherwise genetically targeted. A Cre-off-Flp-on GEVI combined with Cre-on-CheRiff would allow independent genetic specification of pre- and post-synaptic cell types. We expect that uses of synOptopatch in vivo could open doors to explore synaptic plasticity in learning and memory.

2.4 Methods

2.4.1 Design of synOptopatch

We tried several strategies for mutually exclusive expression of CheRiff and QuasAr2. We found that electroporation of two populations of neurons with QuasAr2 or CheRiff and mixed co-culture led to insufficient survival of expressing neurons. We thus sought to take advantage of Cre recombinase-controlled gene expression.

Cre-on constructs. Double lox sites loxP and lox2272 were adopted from the vector pCAG-FLEX-fwd[Chrimson-tdT] (Addgene #59137). The vector was linearized by double digestion with NheI and KpnI and purified by the GeneJET gel extraction kit (Fermentas). Inverted CheRiff-CFP cDNA was generated by PCR amplification and then combined with the pCAG-FLEX backbone by Gibson ligation. The FLEX-DIO-CheRiff-CFP construct was then amplified by PCR and cloned into a modified FCK lentivirus backbone (Addgene #51694), FCAG backbone, in which the original CaMKII promoter was replaced by a CAG promoter.

Cre-off constructs. We tried several strategies to create a Cre-off construct. We first created a Cre-off QuasAr2-Citrine by flanking forward QuasAr2-Citrine sequence with parallel double lox sites loxP and lox2272. Upon lentiviral delivery to cultured rat hippocampal neurons, either with or without co-infection with a Cre-

expressing virus, the constructs individually showed the anticipated Cre-dependent expression (Supplementary Fig. 2a-c). We then used lentiviral vectors to co-infect neurons with both constructs, and delivered Cre virus at low multiplicity of infection (MOI) to activate CheRiff and inactivate QuasAr2 in a subset of the neurons. However, we observed many neurons that co-expressed actuator and reporter (Supplementary Fig. 2d,e).

We hypothesized that the co-expression might be due to the presence of loxP and lox2272 sites in both Cre-on and Cre-off constructs, leading to Cre-mediated cross-reactions between the two constructs. We then turned to orthogonal FAS lox sites. FAS lox sites were adopted from the vector pAAV-Ef1a-FAS-ChETA-TdTomato-WPRE-pA (Addgene #37089). The vector was linearized by double digestion with AscI and NheI and purified by the GeneJET gel extraction kit (Fermentas). QuasAr2-Citrine cDNA was generated by PCR amplification and combined with the Ef1a-FAS backbone via Gibson ligation. The sequence of FAS lox sites and QuasAr2 and Citrine was then amplified by PCR and cloned into a modified FCK lentivirus backbone (Addgene #51694), FSYN backbone, in which the original CaMKII promoter was replaced by a hSyn promoter.

When QuasAr2-Citrine was co-expressed with either mI12b-EGFP or spine-jRGECO1a, the Citrine fluorescence had spectral overlap with the other fluorescent marker. We found that the presence of the citrine tag was beneficial to trafficking. To keep the structural elements of the Citrine tag while eliminating its fluores-

cence we mutated the Citrine chromophore from GYG to GGG using site-directed mutagenesis (Agilent) to create a dark Citrine construct.

Cre constructs. Cre cDNA segments were generated from the template of pCAG-Cre (Addgene #13775) and cloned into FSYN backbone.

2.4.2 Virus production, primary neuronal culture and viral transduction

Experiments in cultured neurons were primarily performed with home-made lentiviral vectors to facilitate rapid testing of many constructs. Experiments in acute brain slices were primarily performed with commercially produced AAV2/9 vectors.

Low titer lentivirus production of synOptopatch. Plasmids encoding Cre-off QuasAr2-Citrine, Cre-off QuasAr2-dark Citrine and Cre-on CheRiff-CFP were used to produce low titer lentivirus according to published methods43. Briefly, low passage number HEK293T cells (ATCC, #CRL-11268) were plated onto gelatin-coated (Stemcell technologies, #07903) 10 cm dishes. When HEK cells reached 80% confluence, the medium was exchanged to a serum-free DMEM medium. After 0.5-1 hours, cells were transfected using polyethylenimine (PEI; Sigma 408727). 6.22 μg of the vector plasmid, 4 μg of the 2nd generation packaging plasmid psPAX2 (Addgene #12260), and 1.78 μg of viral entry protein VSV-G plasmid pMD2.G (Addgene #12259) were mixed into 540 μL serum-free DMEM, and 16 μL of 1 mg/mL PEI were added in the end. The mixture was incubated at room temperature for 10 min, and added dropwise to the plate. After 4

hours, the medium was exchanged back to 10 mL DMEM10. The supernatant was harvested at 36 hours post transfection, and another 10 mL DMEM10 were added to the cells and incubated for another 24 hours. At 60 hours post transfection, the supernatant was harvested again and combined with the first batch of supernatant, centrifuged 5 min at 500 g, and filtered through a 0.45 μm filter (EMD Millipore, #SE1M003M00). The un-concentrated virus was tested with Lenti-X^{TM} GoStix^{TM} (Clontech, #631243), aliquoted and stored at -80 °C for neuronal transduction.

AAV Cre virus. High titer AAV2/9 virus with hSyn Cre-GFP at a titer of 5.54×1013 GC/mL was obtained from UPenn Vector Core. High titer AAV2/9 virus with hSyn Cre at a titer of 2.30×1013 GC/mL was obtained from the Gene Transfer Vector Core at Massachusetts Eye and Ear Infirmary & Schepens Eye Research Institute (MEEI), Harvard Medical School.

Primary neuronal culture and viral transduction. All procedures involving animals were in accordance with the National Institutes of Health Guide for the care and use of laboratory animals and were approved by the Institutional Animal Care and Use Committee (IACUC) at Harvard University. Mouse experiments were performed on strain C57BL/6. Rat experiments were performed on strain sprague dawley.

Hippocampal neurons from P0 rat pups were dissected and cultured in NBActiv4 medium (Brainbits) at a density of 40,000 cm^{-2} on glass-bottom dishes (InVitro

Scientific) or pre-treated dishes (Ibidi 81156) pre-coated with poly-d-lysine (Sigma P7205) and matrigel (BD biosciences 356234). At 2-4 hours post plating, AAV or lenti Cre virus at MOI = 1 and Cre-on CheRiff-CFP low-titer lentivirus at MOI = 5 (typically 200 μL) were added into the neurons. At 1 day in vitro (DIV), plating medium with virus was aspirated and glia cells were plated on top of the neurons at a density of 7000 cm^{-2}. By DIV 5, glia grew into a monolayer and 2 μM AraC was added into the neuronal culture medium to inhibit glial growth. At DIV 5-7, 1 mL of the culture medium was removed and saved for later use. Cre-off QuasAr2-Citrine low-titer lentivirus at MOI = 5 (typically 200 μL) was added into the neurons. 24 hours after adding the virus, the medium was replaced with the 1 mL saved medium and 1 mL fresh medium.

The titer of AAV or lenti Cre virus was determined by titration in neurons as shown in Supplementary Figure 2c. The titer of low titer lentivirus was evaluated by Lenti-X GoStix (Clontech).

2.4.3 Imaging and electrophysiology in primary neurons

Imaging apparatus for primary neurons. Experiments were conducted on a home-built inverted fluorescence microscope equipped with 405 nm, 488 nm, 532 nm, 561 nm, 594 nm, and 640 nm laser lines and a scientific CMOS camera (Hamamatsu ORCA-Flash 4.0). Beams from lasers were combined using dichroic mirrors and sent through an acousto-optic tunable filter (AOTF; Gooch

and Housego TF525-250-6-3-GH18A) for temporal modulation of intensity of each wavelength. The beams were then expanded and sent either to a DMD (Vialux, V-7000 UV, #9515) for spatial modulation or sent directly into the microscope (to avoid power losses associated with the DMD). The beams were focused onto the back-focal plane of a 60× water immersion objective, numerical aperture 1.2 (Olympus UIS2 UPlanSApo 60×/1.20 W, for primary neurons). For CFP, Citrine and QuasAr2, fluorescence emission was separated from laser excitation using a quad-band dichroic mirror (Semrock, Di03-R405/488/532/635-t1-25x36). Imaging of fluorescent proteins was performed at illumination intensities of 2-4 W/cm^2. Imaging of QuasAr2 direct fluorescence was performed at an illumination intensity of 400 W/cm^2. Stimulation of CheRiff was performed at an illumination intensity of 20-120 mW/cm^2.

The optimal camera frame rate entails a balance of signal-to-noise ratio (favoring a slower rate when camera electronic readout noise is significant), field of view (favoring a slower rate) and temporal resolution (favoring a faster rate). We found that at room temperature, all action potentials had a full-width and half-maximum > 5 ms, leading to an optimal frame rate of 500 Hz. For measurements at elevated temperatures one may need to image faster.

Imaging of primary culture. Measurements were performed on primary cultures at DIV 14-21. Experiments were conducted in XC solution containing 125 mM NaCl, 2.5 mM KCl, 3 mM CaCl2, 1 mM MgCl2, 15 mM HEPES, 30 mM glucose (pH

7.3) and adjusted to 305-310 mOsm with sucrose. Experiments were performed at 23 °C under ambient atmosphere. For resolving presynaptic cell types with pharmacology, synaptic blockers were added to the imaging medium. The blockers were NBQX (20 μM, Tocris, #1044), CNQX (20 μM, Tocris, #0190), D-AP5 (25 μM, Tocris, #0106), gabazine (SR-95531, 20 μM, Tocris), and picrotoxin (50 μM, Tocris, #1128). For probing monosynaptic transmission, TTX (50 nM, Tocris, #1078) and 4-AP (100 μM, Tocris, #0940) were added to the imaging medium.

For probing the effects of ketamine, 50 μM ketamine (Zoetis) was added to the imaging medium.

Simultaneous electrophysiology recording and fluorescence imaging. Filamented glass micropipettes (WPI) were pulled to a tip resistance of 5–10 MΩ, and filled with internal solution containing 125 mM potassium gluconate, 8 mM NaCl, 0.6 mM MgCl2, 0.1 mM CaCl2, 1 mM EGTA, 10 mM HEPES, 4 mM Mg-ATP, 0.4 mM Na-GTP (pH 7.3); adjusted to 295 mOsm with sucrose. Pipettes were positioned with a Sutter MP285 manipulator. Whole-cell current clamp recordings were acquired using a patch clamp amplifier (A-M Systems, Model 2400), filtered at 5 kHz with the internal filter and digitized with a National Instruments PCIE-6323 acquisition board at 10 kHz. Simultaneous whole-cell patch clamp and fluorescence recordings were acquired on a home-built, inverted epifluorescence microscope, described above.

2.4.4 Immunostaining of ml12b labeled neurons

For experiments on primary culture, primary cultures were fixed and stained using primary mouse anti Gad67 (Millipore MAB5406) and secondary goat anti mouse 594 (Abcam ab150116) antibodies. The immunostaining followed a protocol described previously[55].

2.4.5 Optopatch measurement of ml12b labeled neurons

Neurons were transfected with lentivirus encoding Cre-off CheRiff-CFP, Cre-off QuasAr2-dark Citrine and ml12b-EGFP.

Synaptic blockers (NBQX, D-AP5, and gabazine) were added to block network activity. Cells were stimulated with 500 ms blue light (1 Hz) of increasing intensity (20 to 120 mW/cm^2) for four seconds and ramp blue light of increasing intensity (0 to 120 mW/cm^2) for another four seconds, while firing patterns were recording under continuous red illumination.

2.4.6 Simultaneous imaging of postsynaptic spine-jRGECO1a and QuasAr2 with optogenetic presynaptic stimulation

Construction of a bicistronic construct with spine-jRGECO1a and QuasAr2. To avoid spectral overlap of spine-jRGECO1a and the Citrine tag of QuasAr2, we used QuasAr2-dark Citrine. We used the porcine teschovirus-1 (P2A) sequence

to co-express spine-jRGECO1a and QuasAr2-dark Citrine.

Gene delivery. Cre-on soma-localized CheRiff-CFP was lentivirally delivered to presynaptic cells and the sparseness was controlled by the MOI of Cre virus (MOI = 0.5). The bicistronic construct with spine-jRGECO1a and QuasAr2-dark Citrine was delivered to neurons via calcium phosphate, as previously described5. Neurons expressing the reporters and not the actuator were selected for measurement.

Imaging apparatus. We modified the imaging apparatus for simultaneous spine-jRGECO1a and QuasAr2 imaging. We used a 40× silicone oil UPLSAPO objective, numerical aperture 1.25 (Olympus UIS2 UPLSAPO 40×/1.25). For CFP, spine-jRGECO1a and QuasAr2, fluorescence emission was separated from laser excitation using a quad-band dichroic mirror (Chroma, ZT405/488/561/640rpc). The 488 nm and the 561 nm light were sent through the DMD (Vialux, V-7000, #9515). Stimulation of soma-localized CheRiff was performed at an illumination intensity of 200 mW/cm^2. Imaging of spine-jRGECO1a was performed by using the DMD to pattern 561 nm light onto the postsynaptic cell while avoiding presynaptic CheRiff-expressing somata. The 561 nm light was at an intensity of 0.4 W/cm^2. Imaging of QuasAr2 direct fluorescence was performed with 640 nm light at an intensity of 400 W/cm^2.

A 640 nm dichroic beam splitter (Semrock, FF640-FDi01-25×36) in the emission path separated the QuasAr2 from the spine-jRGECO1a emission, sending each to a separate camera, a scientific CMOS camera (Hamamatsu ORCA-Flash 4.0) for

voltage imaging and an EMCCD camera (Andor iXonEM+ DU-897E) for Ca^{2+} imaging (20 Hz).

2.4.7 Virus production, hiPSC-derived neuron culture and viral transduction

Concentrating synOptopatch lentivirus. Lenti-X concentrator (Clontech, 631231) was used to concentrate low titer synOptopatch lentivirus. Concentrated lentivirus was then used for hiPSC-derived neuron experiments.

High titer lentivirus encoding Cre. For experiments in hiPSC-derived neurons, high titer lentivirus with Cre driven by a hSyn promoter were produced by Alstem LLC with a titer of 2.60×10^{9} IFU/mL.

HiPSC-derived neuron culture and viral transduction. To achieve orthogonal expression of actuator and reporter, we first tried lentiviral delivery of Cre-independent CheRiff and QuasAr2 to separate pools of hiPSCs in the stem cell state, followed by mixing and replating at the progenitor state. However, after 28 days of differentiation we only detected weak expression of both constructs, likely a consequence of gene silencing during differentiation. We then tried the Cre-dependent synOptopatch approach that had worked in primary neurons and achieved robust and non-overlapping expression of reporter and actuator (Supplementary Fig. 5g).

Neuronal differentiation of human stem cells was carried out as previously described44 with the following modification. Human iPSCs with TetO-NGN2-

PURO were plated onto plastic dishes. Doxycline (2 μg/mL) was added at 1 day (DIV 1) after plating to induce NGN2 expression. Puro was added at DIV 2 to kill the cells which did not express NGN2. On DIV 4, differentiated neurons were replated at a density of 80,000 cm^{-2} on preestablished rat glial monolayers grown on 8-well ibidi dishes (ibidi, 80826) in neural basal medium with B27. On DIV 10, lentivirus of Cre at MOI = 1 was added into the medium and incubated for one day. On DIV 14, concentrated lentiviruses of Cre-on CheRiff and Cre-off QuasAr2 at MOI = 5 were added and incubated for one day. 50% medium exchanges were done every 3-4 days. Two days before imaging, 200 nM all trans-retinal was added into the medium.

2.4.8 Imaging in hiPSC-derived neurons

Imaging apparatus for hiPSC-derived neurons. We used the same imaging apparatus as for primary neurons, but a 40× water immersion objective, numerical aperture 1.2 (Zeiss C-apochromat 40×/1.2 W). Stimulation of CheRiff was performed at a higher illumination intensity of 400 mW/cm^2.

Imaging of hiPSC-derived neurons. For hiPSC-derived neurons, measurements were performed at DIV30 - 42. Experiments were conducted in XC medium at 37 °C controlled by a Tokai Hit stage top incubator (Tokai Hit, WSKM).

For potentiating synaptic transmission of hiPSC-derived neurons, CTZ (50 μM, Tocris, # 0713) was added to the imaging medium.

2.4.9 Virus production, acute brain slices and viral injection

AAV virus preparation. FAS Cre-off CheRiff-CFP construct was cloned into an AAV vector, AAV2/9-hSyn-WPRE-SVPA, for custom AAV production. Cre-on soma-localized QuasAr2 was cloned into an AAV vector, AAV2/9-CAG-WPRE-SVPA, for custom AAV production.

All custom AAV production was by the Gene Transfer Vector Core at Massachusetts Eye and Ear Infirmary & Schepens Eye Research Institute (MEEI), Harvard Medical School.

Virus injection for acute slices measurement. AAV2/9 hSyn-Cre-off CheRiff-CFP (5.55×10^{13} GC/mL) and AAV2/9 CAG-FLEX QuasAr2S-Citrine (2.09×10^{12} GC/mL) were mixed in a 1:2 volume ratio for virus injection.

Rbp4-Cre+/- mice were crossed with wild-type C57BL/6 mice. Pups were cryo-anesthetized at P0-P2 and immobilized dorsal side up under a stereotaxic microscope. Injections were made using home-pulled micropipettes (Sutter P1000 pipette puller), mounted in a microinjection pump (World Precision Instruments Nanoliter 2010) controlled by a microsyringe pump controller (World Precision Instruments Micro4). The micropipette was positioned using a stereotaxic instrument (Stoelting Digital Mouse Stereotaxic Instrument). Pups were injected in the left hemisphere, 0.9 mm lateral and 0.7 mm anterior to lambda. Starting at a depth of 0.6 mm beneath the surface of the skull, virus injections (40 nL, 5 nL/s)

were performed at 0.1 mm increments as the pipette was withdrawn. Pups were placed back in their home cage once they were awake.

Genotyping. Genotyping for Rbp4 was performed with the PCR primer pairs: Cre 5': 5' TAT CTC ACG TAC TGA CGG TG 3' and Cre 3': 5' AGA CTA ATC GCC ATC TTC CAG C 3' to yield a 500 bp band from Cre. Acute slice preparation. Acute brain slices were prepared from P16–P28 Rbp4-Cre+/- mice. The mice were anesthetized by isoflurane and then perfused with carbogen (95% O2, 5% CO2)-saturated ice-cold slicing solution with the following composition (in mM): 110 choline chloride, 2.5 KCl, 1.25 NaH2PO4, 25 NaHCO3, 25 glucose, 0.5 CaCl2, 7 MgCl2, 11.6 Na-ascorbate, and 3.1 Na-pyruvate. Mice were then decapitated and the brains were rapidly coronally sliced with 300 μm thickness on a vibratome (Leica VT 1200S).

Slices were incubated for 45 min at 34 °C in a carbogenated artificial CSF (ACSF) with the following composition (in mM): 127 NaCl, 2.5 KCl, 1.25 NaH2PO4, 25 NaHCO3, 25 glucose, 2 CaCl2, and 1 MgCl2. The osmolarity of all solutions was adjusted to 300–310 mOsm and the pH was maintained at 7.3 under constant bubbling with carbogen.

2.4.10 Imaging in acute brain slices

Imaging apparatus for acute slices. Experiments were conducted on a home-built upright fluorescence microscope equipped with 488 nm, and 640 nm laser

lines and a scientific CMOS camera (Hamamatsu ORCA-Flash 4.0)[91]. Briefly, lasers beams were combined using dichroic mirrors, sent through an acousto-optic tunable filter (Gooch and Housego 48058-2.5-.55) for intensity modulation, and then expanded and focused onto the back-focal plane of a 20× water immersion objective, numerical aperture 1.0 (Olympus XLUMPLFLN 20×/1.0 W). Both 488 nm light and 640 nm light could go through an alternative optical path containing a digital micromirror device (DMD, Vialux, V-7000 UV, #9515) for patterned illumination. 640 nm light was patterned to only illuminate the somas of neurons, while 488 nm light was targeted to the whole field at intensity of 50-100 mW/cm^2.

For fast data acquisition, a small field of view around the cell of interest was chosen at the center of the camera to achieve a frame rate of 500 frames per second.

Imaging acute slices. For acute slices, measurements were conducted in ACSF at 23 °C under ambient atmosphere. The slice was immobilized in a Warner Instruments RC-27LD flow chamber using a slice anchor (Warner Instruments, SHD-27LH/2). ACSF, perfused with carbogen, was flowed through the chamber at a rate of 2 mL/minute and recycled through a flow pump (Fisher scientific, 13-876-2).

To confirm that fluorescence transients arose from synaptic transmission, synaptic blockers were added to the imaging medium. The blockers were NBQX (10

μM, Tocris, #1044), (R)-CPP (10 μM, Tocris, #0247), and gabazine (SR-95531, 10 μM, Tocris).

2.4.11 Confocal imaging

Acute slices were fixed and confocal fluorescence imaging was performed on an Olympus FV1000 confocal microscope at the Harvard Center for Brain Sciences microscope facility.

2.4.12 Data analysis

Data were analyzed with homemade code written in MATLAB.

Data analysis for primary culture. Fluorescence intensities from raw movies were extracted using a maximum likelihood pixel weighting algorithm described in Ref[33]. Traces showing spontaneous spikes or PSPs were rejected (5% of the data). The remaining traces were then averaged by aligning with each blue light stimulation.

We used several parameters to classify synaptic inputs. First, we calculated the area under the curve (AUC) of the fluorescence trace corresponding to the PSP. Next we calculated maximum height of the PSP (Amp). Cells that had AUC < 0 and Amp below the noise floor were classified as having purely inhibitory inputs; cells with AUC < 0 and Amp above the noise floor were classified as having mixed inputs; cells with AUC > 0 were classified as having purely excitatory inputs.

Data analysis for simultaneous spine Ca^{2+} and soma voltage recordings. Spines were identified by the amplitude of the fluorescence fluctuations at each pixel. A threshold was selected to identify up to 100 spines per neuron. Synaptically activated spines were identified by the following criteria: Ca^{2+} transients among the top 15% of all spines; above the noise level; and aligned with presynaptic stimulation. Fluorescence traces were corrected for photobleaching.

Data analysis for voltage recordings in hiPSC-derived neurons and acute brain slices. A region of interest comprising the cell body and adjacent neurites was manually defined, and fluorescence intensities were calculated from the unweighted mean of pixel values within the region of interest. Background fluorescence from a cell-free region was subtracted from the baseline fluorescence of the cell. Traces were then corrected for photobleaching and averaged by aligning with each blue light stimulation.

2.4.13 Statistics

All error ranges represent standard error of the mean, unless otherwise specified. For the same neurons before and after drug manipulation, paired sample t-test was used. For two-sample comparisons of a single variable, student's t-test was used. Comparisons of ketamine effects on excitatory monosynaptic transmission for inhibitory vs excitatory postsynaptic neurons were made using a one-way ANOVA analysis. Analysis of ketamine effect on GABAergic synaptic transmission

was made by linear regression fit. Probabilities of the null hypothesis $p < 0.05$ were judged to be statistically significant.

2.5 Data availability

The datasets generated during and/or analyzed during the current study are available from the corresponding author on reasonable request. Addgene numbers for constructs developed in this study are listed in Supplementary Table 1.

2.6 Supplemental Figures

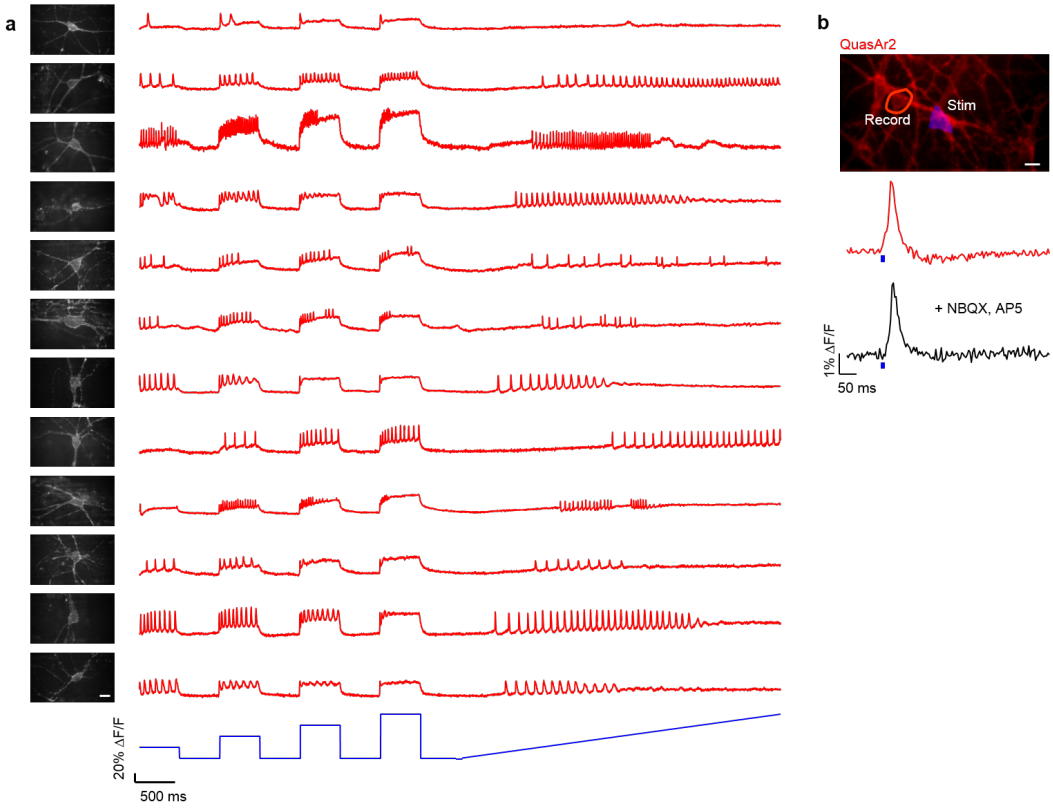

Figure 2.6: Co-expression of a CheRiff and QuasAr2 introduced optical crosstalk in measurements of synaptic transmission. (**a**) In neurons co-expressing CheRiff-CFP and QuasAr2-Citrine, the QuasAr2 citrine fluorescence reported action potentials with high SNR. Left: Images of QuasAr2 fluorescence. Scale bar 20 μm. Right: fluorescence of QuasAr2 during optogenetic stimulation, recorded at 500 Hz. Blue: Optogenetic stimulation waveform. (**b**) Top: red: QuasAr2 fluorescence, blue: DMD mask for patterned blue light stimulation. Scale bar: 10 μm. Bottom: fluorescence signal of the circled cells before (red) and after (black) addition of excitatory blockers NBQX (20 μM) and AP5 (50 μM). The persistence of the signal indicates that it arose from direct optogenetic stimulation of a post-synaptic neurite rather than from synaptic transmission.

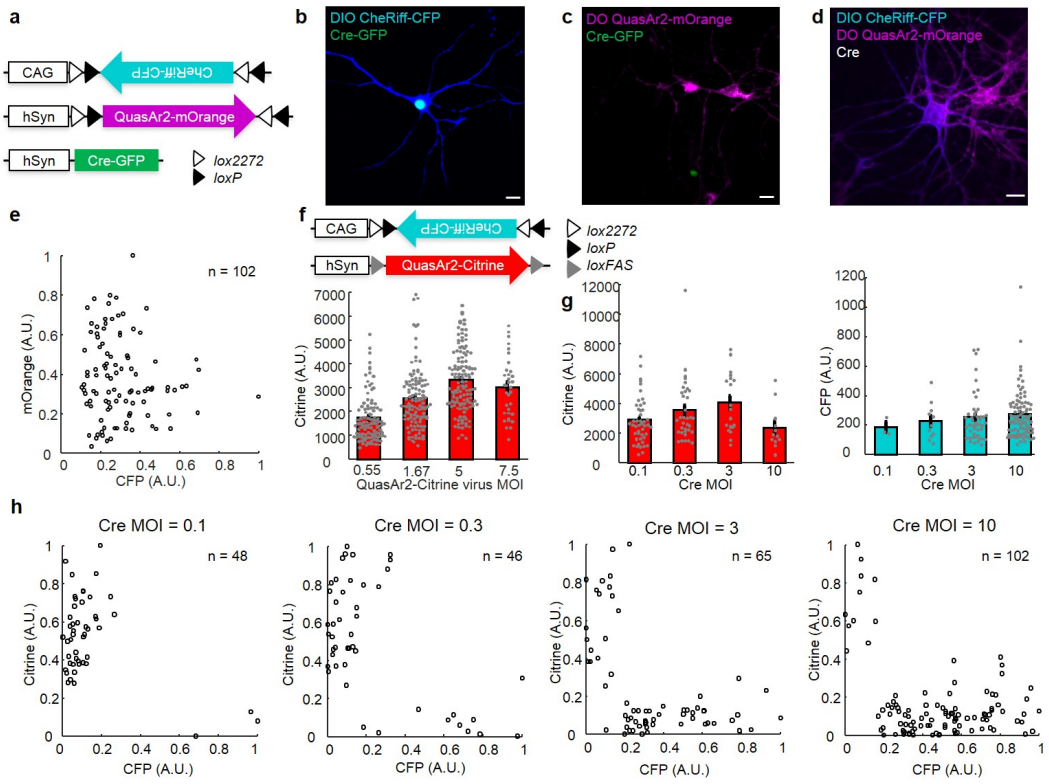

Figure 2.7: Redundant use of Cre recombination sites caused spurious cross-reactivity. (**a**) Schematic of DIO Cre-on CheRiff-CFP and DO Cre-off QuasAr2-mOrange. (**b**) Neurons co-infected with DIO Cre-on CheRiff-CFP and Cre-GFP showed Cre-activated expression. (**c**) Neurons co-infected with DO Cre-off QuasAr2-mOrange and Cre-GFP showed Cre-inactivated expression. (**d**) Neurons co-infected with DIO CheRiff-CFP, DO QuasAr2-mOrange and Cre did not show mutually exclusive expression of the actuator and reporter. Scale bars in (b)-(d) 20 μm. (n in (b)-(d) = 3 culture dishes; representative data are shown) (**e**) Quantification of the data in (d) showing lack of mutually exclusive expression (n = 102 neurons). (**f**) Top: schematic of DIO Cre-on CheRiff-CFP and FAS Cre-off QuasAr2-Citrine. Bottom: mean expression levels of FAS Cre-off QuasAr2-Citrine depended on the titers of the FAS Cre-off QuasAr2-Citrine lentiviruses. (n = 391 neurons) (**g**) Mean expression levels in expressing cells of (left, n = 112 neurons) FAS Cre-off QuasAr2-Citrine and (right, n = 149 neurons) DIO Cre-on CheRiff-CFP did not depend on the titer of the Cre virus. (**h**) SynOptopatch constructs mediated mutually exclusive expression of actuator and reporter. No co-expression of DIO Cre-on CheRiff-CFP and FAS Cre-off QuasAr2-Citrine was observed across a range of titers of Cre virus. All statistics are mean ± s.e.m. All error bars, s.e.m.

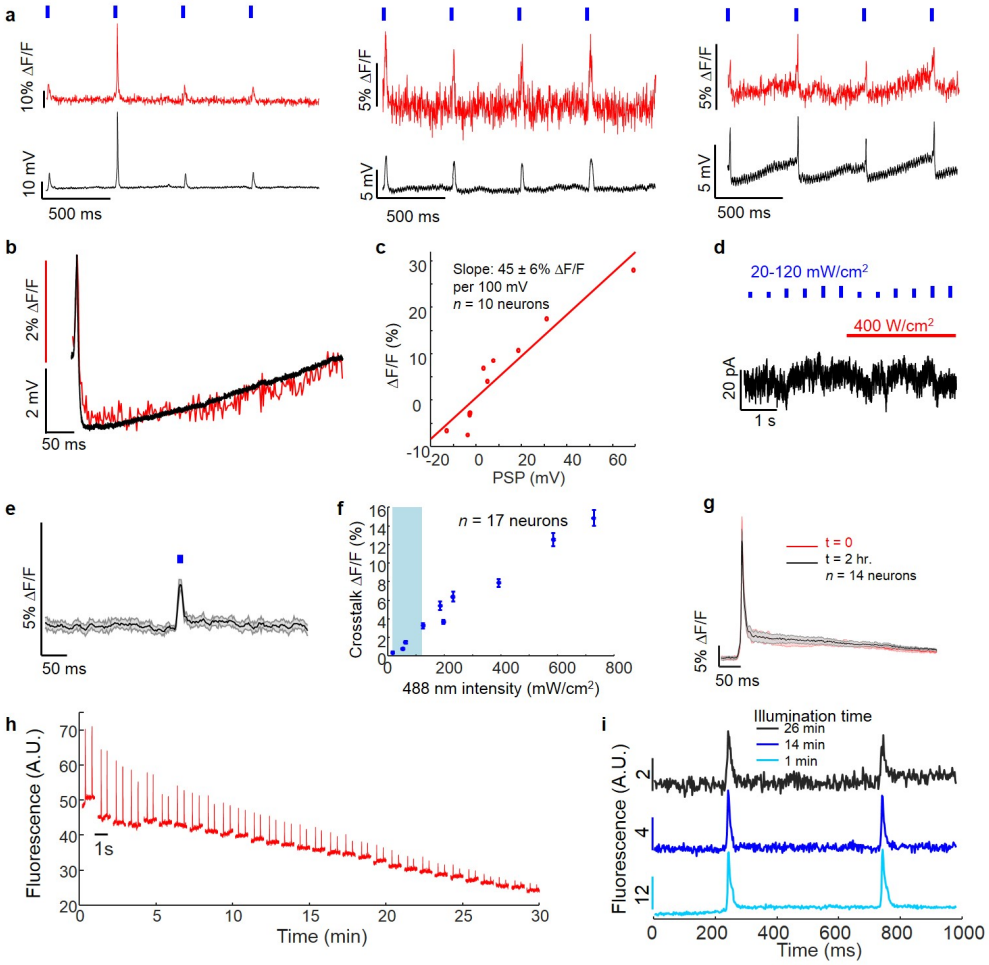

Figure 2.8: Calibration of the synOptopatch constructs. (**a**) Simultaneous fluorescence and manual patch clamp recordings of PSPs and APs evoked by presynaptic optogenetic stimulation. Blue, 10 ms blue light stimulation; red, whole-cell single-trial unfiltered fluorescence; black, patch-clamp recordings. (**b**) Overlay of mean optically and electrically recorded PSP waveforms from a single cell (n = 9 repeats). (**c**) Quantification of fluorescence vs. postsynaptic potential for synOptopatch recordings (n = 10 neurons, $R^2 = 0.9$). (**d**) Quantification of photocurrent of QuasAr2 under red and blue illumination (red: 400 W/cm^2; blue: 10 ms, 20 – 120 mW/cm^2). (e, f) Quantification of optical crosstalk of blue illumination into QuasAr2 fluorescence. (**e**) Neurons expressing QuasAr2 were exposed to continuous excitation at 640 nm and pulses of illumination at 488 nm (10 ms, 60 mW/cm^2) (n = 17 neurons). (**f**) Quantification of crosstalk amplitude as a function of blue light intensity. The shading represents the range of blue light intensity used for optogenetic stimulation of primary neurons. Error bars represent s.e.m. (**g**) SynOptopatch fluorescence recordings of EPSPs were stable for at least 2 h. (**h**) Photobleaching of QuasAr2 in the synOptopatch assay. A neuron was illuminated for 30 minutes continuously at 640 nm, 400 W/cm^2 and probed at 60 s intervals with blue light to induce PSPs (2 pulses of 10 ms, 2 Hz, 60 mW/cm^2). (**i**) Stability of PSP waveform recorded as a function of duration of continuous red illumination. (In (h,i), n = 3 neurons; representative data are shown). All shaded error bars, s.e.m.

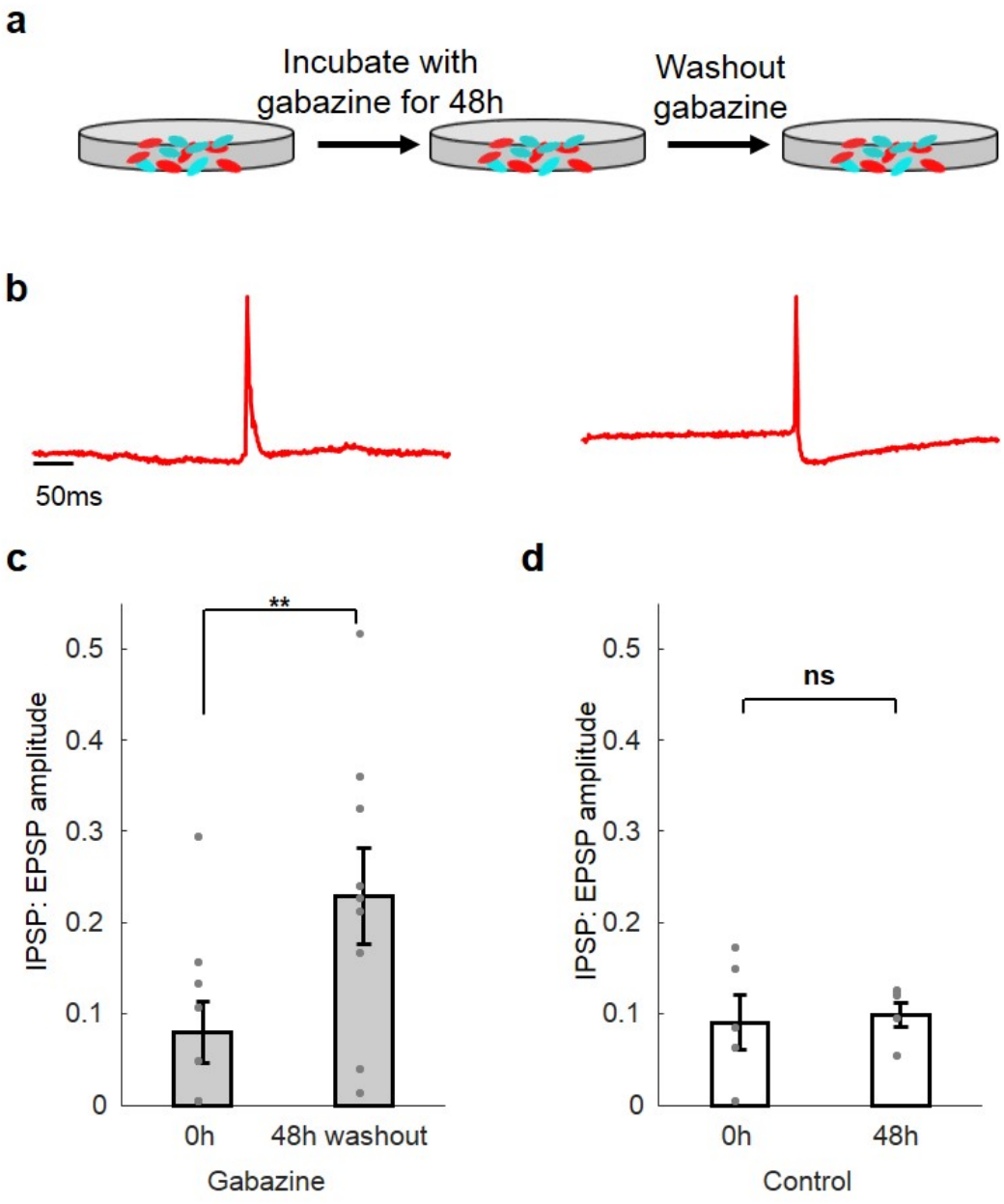

Figure 2.9: SynOptopatch detects synaptic plasticity. (**a**) Schematic showing protocol for inducing homeostatic plasticity. (**b**) A typical ten-trial average trace of a same neuron measured before gabazine incubation (left) and when wash-out after 48h incubation with gabazine (right). (**c**) Neurons incubated for 48h with gabazine had increased ratio of IPSP amplitude over EPSP amplitude (n = 9 neurons, **p = 0.04, two-sided paired-sample t-test), while (**d**) control cells did not show significant increase in the ratio of IPSP amplitude over EPSP amplitude (n = 5 neurons, p = 0.76, two-sided paired-sample t-test). All error bars, s.e.m. All statistics are mean ± s.e.m.

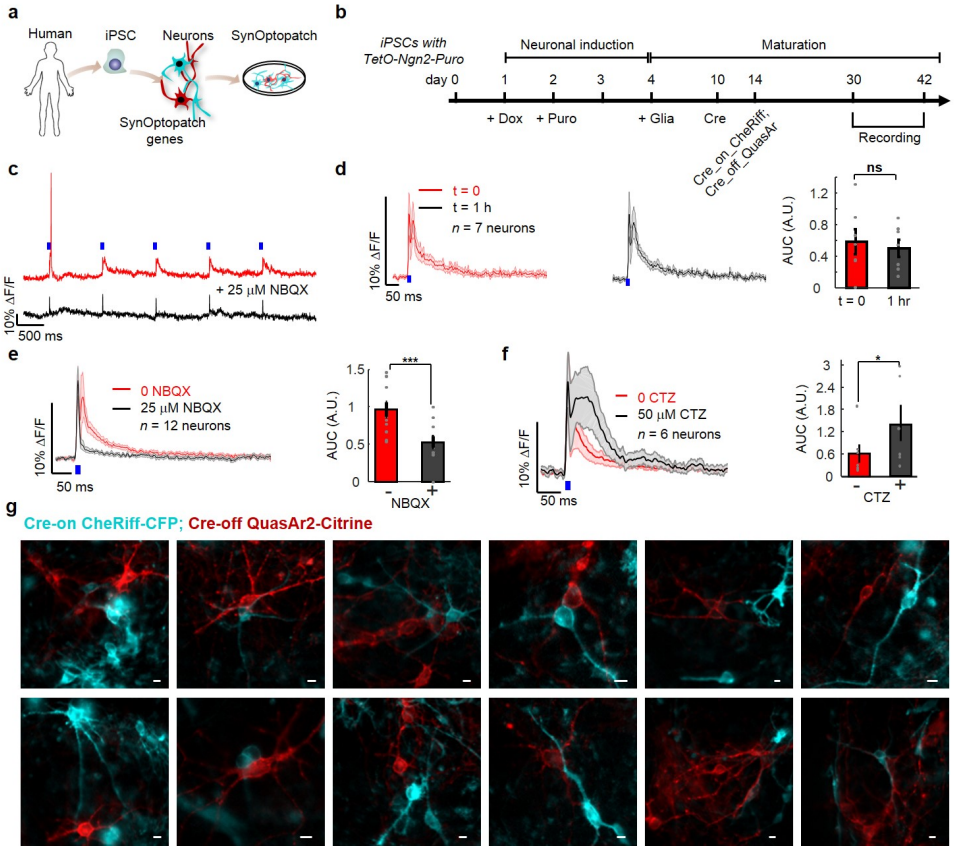

Figure 2.10: SynOptopatch in hiPSC-derived neurons. (**a**) Schematic of synOptopatch in hiPSC-derived neurons. (**b**) Schematic of excitatory cortical neuron differentiation, gene transduction, maturation and measurement. (**c**) Blue light stimulation induced single-trial PSPs and APs (red: before; black: after NBQX addition). Due to lower CheRiff expression than in primary neurons, stimulation required higher blue light intensities (400 mW/cm^2 vs. 20 – 120 mW/cm^2 for primary neurons) to evoke presynaptic APs. (n = 12 neurons; representative data are shown). (**d**) PSPs were stable for one hour (red: before; black: one hour without perturbation). Right: quantification of AUC before and after one hour (AUC, A.U., 0.58 ± 0.16 vs. 0.50 ± 0.11, n = 7 neurons, p = 0.4, two-sided paired-sample t-test). (**e**) A synaptic blocker (25 μM NBQX) largely eliminated the PSPs. The residual transient in the presence of NBQX occurred concurrent with the blue light stimulation, indicating that this signal arose from blue light crosstalk, a consequence of the higher blue stimulation power needed (also visible in (d) and (f)). Right: quantification of AUC before and after addition of NBQX (AUC, A.U., 0.97 ± 0.1 vs. 0.53 ± 0.07, n = 12 neurons, ***p = 2×10^{-5}, two-sided paired-sample t-test). (**f**) A positive allosteric modulator of AMPARs and kainate receptors (cyclothiazide (CTZ), 50 μM) increased the PSP amplitude. Right: quantification of AUC before and after addition of CTZ (AUC, A.U., 0.63 ± 0.26 vs 1.4 ± 0.48, n = 6 neurons, *p = 0.055, two-sided paired-sample t-test). (**g**) Exclusive expression of QuasAr2 and CheRiff in hiPSC derived neurons. Green: presynaptic cells expressing CheRiff-CFP. Red: postsynaptic cells expressing QuasAr2-Citrine, showing Citrine fluorescence. All scale bars 10 μm. (n = 3 culture dishes; representative data are shown) All shaded error bars and error bars, s.e.m. All statistics are mean ± s.e.m.

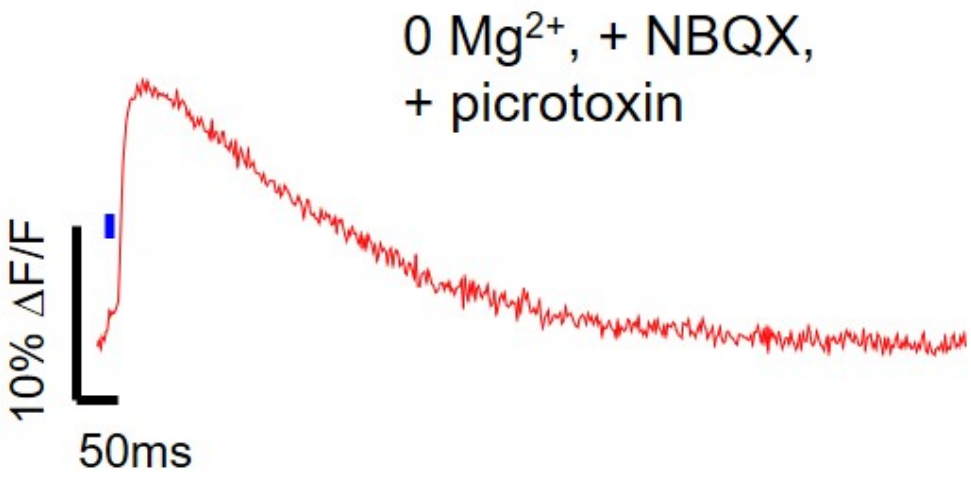

Figure 2.11: NMDAR component of post-synaptic potential. To isolate the NMDAR component of the PSP, we added 10 μM NBQX and 10 μM picrotoxin to block AMPA and GABAa receptors, respectively, and imaged in a medium containing 0 Mg^{2+} to remove the voltage-dependent Mg^{2+} NMDAR block. Ten-trial average. (n = 10 neurons; representative data are shown)

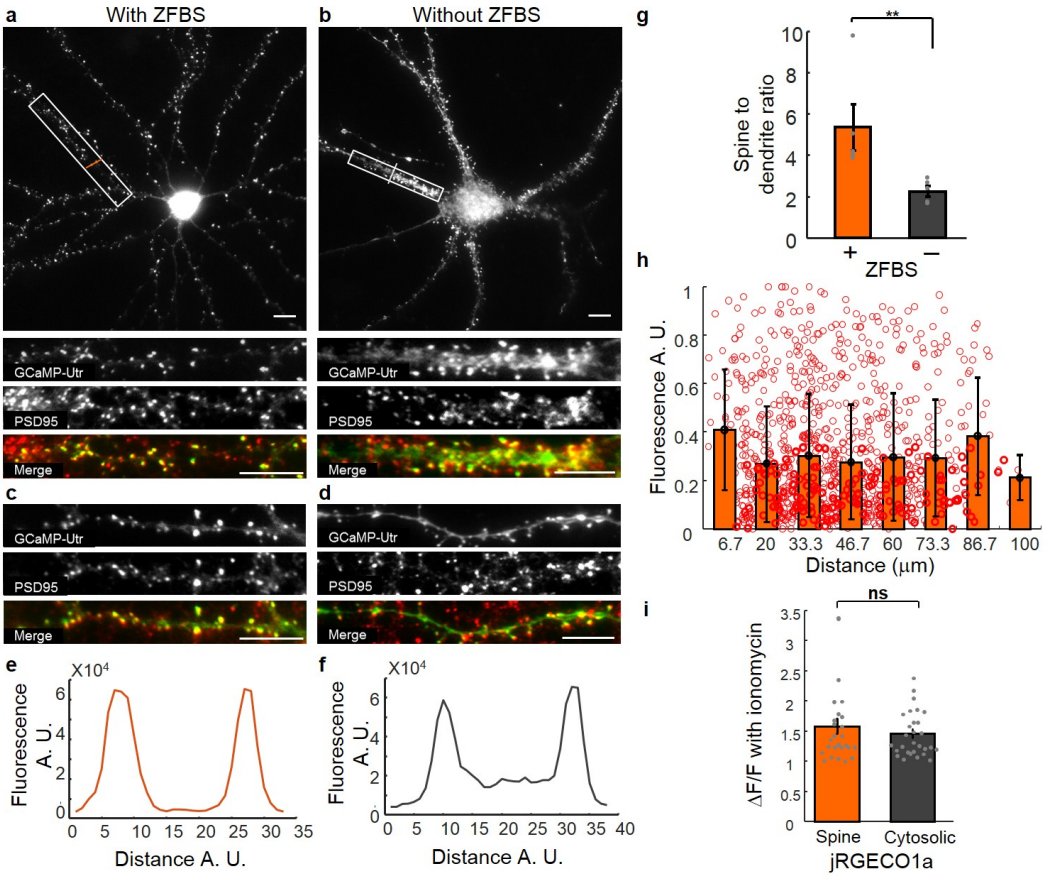

Figure 2.12: Targeting GCaMP6s and jRGECO1a to dendritic spines with and without transcriptional regulatory system. (**a**) Image of a neuron expressing GCaMP6s fused to the CH domain of Utrophin (GCaMP6s-Utr) with zinc finger binding sequence (ZFBS). GCaMP6s was stained with anti-GFP antibody. GCaMP6s co-localized with endogenous PSD-95, a marker for dendritic spines. PSD95 puncta not associated with GCaMP6s puncta were due to spines from neighboring neurons not expressing GCaMP6s. Scale bar: 10 μm. (**b**) GCaMP6s-Utr without ZFBS exhibited more diffuse localization compared to regulated GCaMP6s-Utr. (**c,d**) Examples from additional neurons as in a and b, respectively. (a-d, n = 5 neurons; representative data are shown). (**e,f**) Example fluorescence line sections transecting two spines and a parent dendrite along the lines shown in a and b, respectively. (**g**) Quantification of ratio of fluorescence in spines to adjacent parent dendrites in cells expressing GCaMP6-Utr with or without the ZFBS (n = 5 neurons of each type, 200 spines/neuron, **p = 0.027, two-sided t-test). (**h**) Quantification of spine fluorescence as a function of distance from the soma (n = 5 neurons of each type, 200 spines/neuron). (**i**) Spine-jRGECO1a and cytosolic jRGECO1a expressed in HEK293 cells gave the same fluorescence response to a Ca^{2+} transient induced by 10 μM ionomycin ($\Delta F/F$ 1.6 $\pm$ 0.1 vs. 1.5 $\pm$ 0.07, n = 26 cells for spine-jRGECo1a, n = 29 for cytosolic jRGECO1a, p = 0.4, two-sided student's t-test). All error bars, s.e.m. All statistics are mean $\pm$ s.e.m.

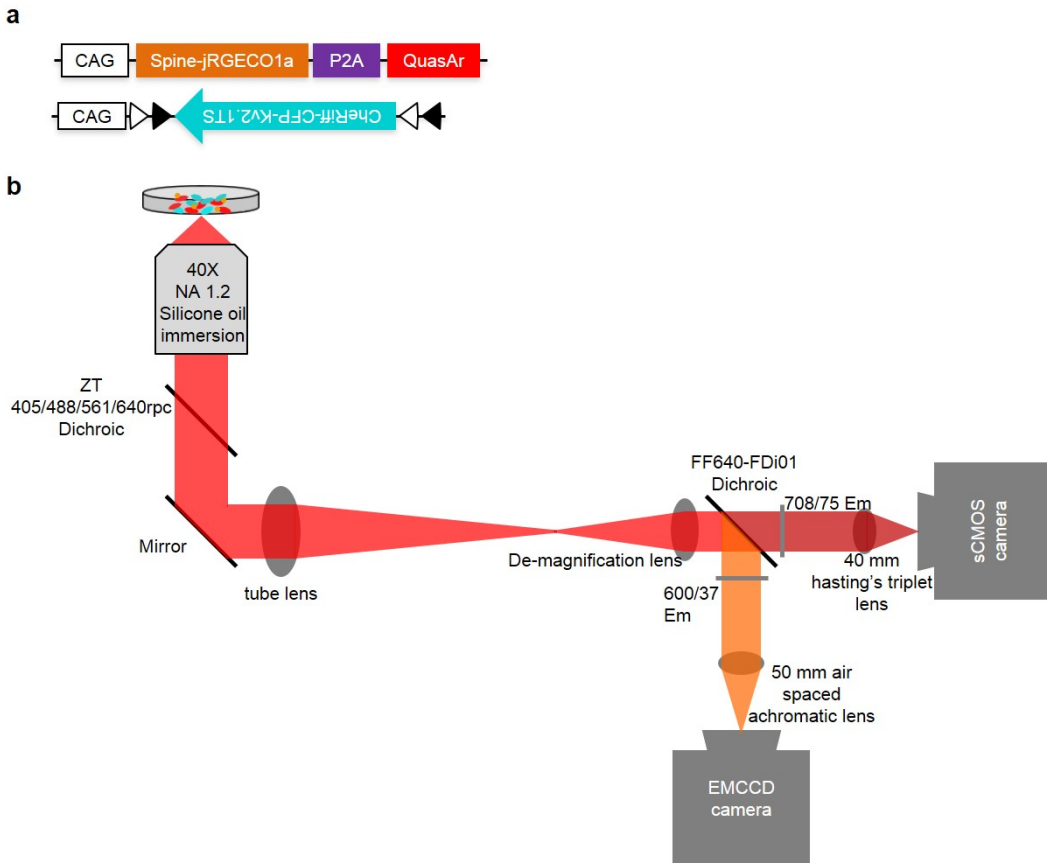

Figure 2.13: Simultaneous imaging of spine-jRGECO1a and QuasAr2. (**a**) Co-expression of spine-jRGECO1a and QuasAr2. Schematic showing three color imaging with blue light excitable soma-localized CheRiff in presynaptic cells, yellow light excitable spine-jRGECO1a and red light excitable QuasAr2 co-expressed in postsynaptic cells. (**b**) Dual-view microscope for simultaneous imaging of spine-jRGECO1a and QuasAr2. Fluorescence from spine-jRGECO1a and QuasAr2 were passed to EMCCD camera and sCMOS camera, respectively, by a 640 nm dichroic beamsplitter.

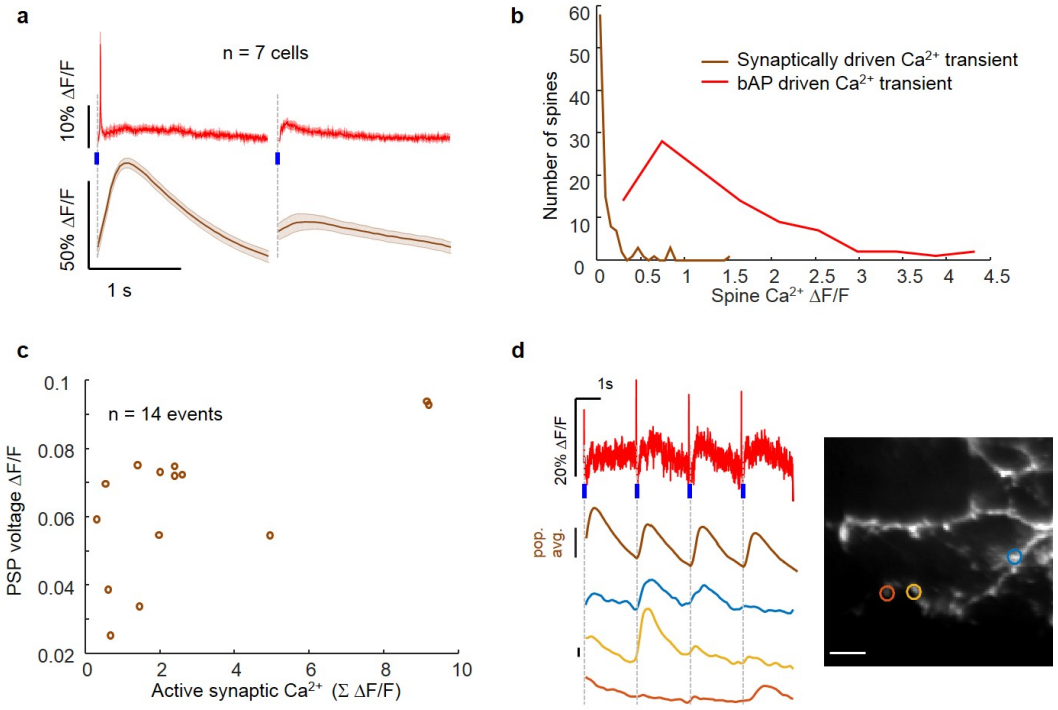

Figure 2.14: Correlation of synaptic and bAP induced Ca^{2+} activity in dendritic spines. (**a**) Red: mean AP and PSP reported by QuasAr2; orange: mean spine-jRGECO1a fluorescence induced by bAP and sub-threshold synaptic inputs, respectively. (**b**) Distribution of Ca^{2+} transient amplitudes in spines, induced by bAPs (red) or subthreshold synaptic inputs (brown). Synaptic inputs only drove Ca^{2+} transients in a subset of synaptic spines, while bAPs drove Ca^{2+} signals synchronously in almost all dendritic spines. (**c**) Correlation of somatic PSPs and sum of Ca^{2+} transient amplitude across all spines (n = 14, R2 =0.42, p = 0.01). (**d**) bAP failure in spines. Blue: 10 ms blue light stimulation of soma-localized CheRiff in a presynaptic cell. Red: Postsynaptic QuasAr2 fluorescence; dark yellow: average over all the spines of spine-jRGECO1a fluorescence (n = 100 spines). Right: Single-spine fluorescence traces within a single dendritic branch, corresponding to the regions circled in the figure. The orange trace shows an example of a bAP-induced spine Ca^{2+} transient distal to a spine which did not respond to the bAP. Scale bar 15 μm. All shaded error bars, s.e.m.

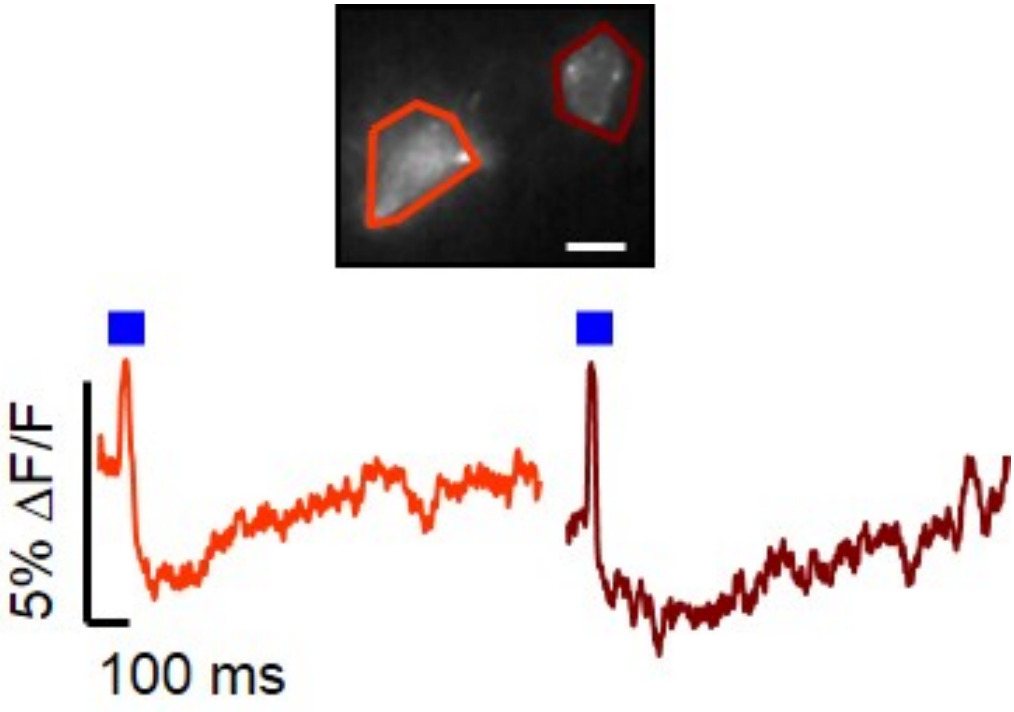

Figure 2.15: IPSPs in acute slices under high K^+ concentration. IPSP detected under the condition of 5 mM K+, twice higher than usual ACSF, and 10 μM NBQX, 10 μM AP5. Blue: 10 ms blue light stimulation. Light and dark red: IPSPs. Scale bar 10 μm. Five-trial average. (n = 8 cells; representative data are shown).

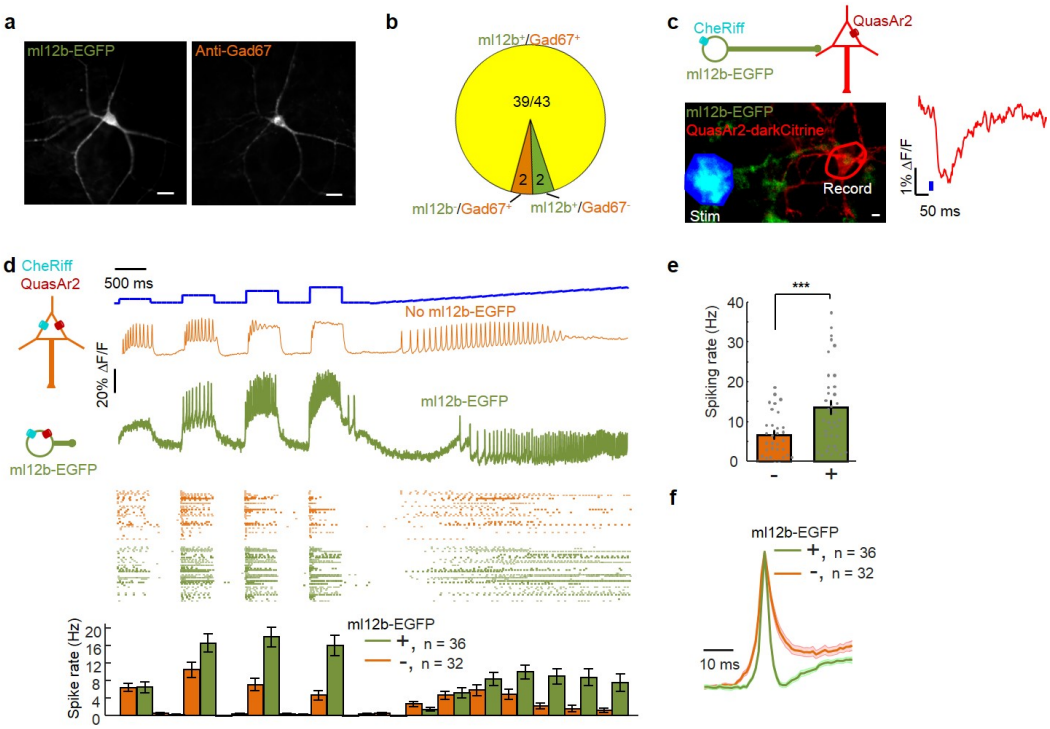

Figure 2.16: Development and characterization of an inhibitory neuron–specific enhancer. (**a**) The inhibitory marker Gad67 co-localized with eGFP expression. Left: mI12b-eGFP; Right: anti-GAD67 immunostaining (**Section 2.4**). Scale bars: 30 μm. (n = 39 cells; representative data are shown). (**b**) Correspondence of mI12b-eGFP fluorescence and Gad67 immunostaining in neurons that were positive for at least one of these reporters. Of n = 41 Gad67$^+$ neurons, 39 were mI12b-eGFP$^+$. Of n = 41 mI12b-eGFP$^+$ neurons, 39 were also Gad67$^+$. (**c**) Top: Schematic showing patterned light stimulation onto an mI12b-eGFP$^+$ neuron and voltage imaging from a nearby cell expressing QuasAr2. Middle: dark green: mI12b-eGFP, red: QuasAr2-dark Citrine, blue: DMD mask for patterned blue light stimulation. Right: IPSP was evoked by stimulation of the presynaptic cell expressing mI12b-EGFP. Scale bar: 10 μm. Two-trial average. (n = 3 cells; representative data are shown). (**d**) Optopatch measurements of spiking patterns and AP waveforms revealed differences between mI12b-eGFP$^+$ and mI12b-eGFP$^-$ neurons consistent with differences between inhibitory vs. excitatory neurons reported by patch clamp measurements (**Section 2.4**)[85,86]. Blue: blue light stimulation of cells expressing both CheRiff and QuasAr2. Example traces show QuasAr2 fluorescence from a nominal excitatory neuron (orange, mI12b-EGFP$^-$) and a nominal inhibitory neuron (green, mI12b-EGFP$^+$). Middle: raster plots of spiking. Bottom: spike rate of nominal excitatory neurons (orange, mI12b-EGFP$^-$) and inhibitory neurons (green, mI12b-EGFP$^+$). (**e**) Spiking rate and (**f**) spiking waveform of cells not expressing mI12b (orange) and expressing mI12b (dark green). All shaded error bars and error bars, s.e.m. mI12b-eGFP$^+$ neurons (putative interneurons) showed higher average evoked firing rates (13.6 $\pm$ 1.7 vs. 6.7 $\pm$ 1 Hz, p = 0.001, two-sided two-sample t-test), lower probability of depolarization block under strong stimulus, narrower action potentials (6.9 $\pm$ 0.2 ms vs. 9.4 $\pm$ 0.4 ms, p = 1$\times$10 -6 , two-sided two-sample t-test) and larger after-hyperpolarization compared to simultaneously measured mI12b-eGFP$^-$ cells (n = 36 mI12b-eGFP$^+$ and 32 mI12b-eGFP$^-$ neurons).

Table 2.1

synOptopatch constructs	Vector	Addgene
LZF40: hSyn-Cre	Lenti-vector	109378
LZF43: Cre-on CAG-CheRiff-CFP (DIO)	Lenti-vector	104114
LZF80: Cre-on CAG-CheRiff-soma-CFP (DIO)	Lenti-vector	104115
LZF42: Cre-off hSyn-QuasAr2-Citrine (FAS)	Lenti-vector	104116
LZF70: Cre-off hSyn-QuasAr2-dark Citrine (FAS)	Lenti-vector	104117
LZF39: Cre-off hSyn-CheRiff-CFP (FAS)	Lenti-vector	104118
LZF1718: Cre-off hSyn-CheRiff-CFP (FAS)	AAV vector	104119
LZF94: Cre-on CAG-spine-GCaMP6s	AAV vector	104120
LZF97: hSyn-spine-jRGECO1a	Lenti-vector	104121
LZF1604: CAG-spine-jRGECO1a-P2A-QuasAr2-dark Citrine	pcDNA	104122
LZF1723: ml12b-EGFP	Lenti-vector	104123

2.7 Supplemental Movies

https://www.nature.com/articles/s41592-018-0142-8#Sec54

https://static-content.springer.com/esm/art%3A10.1038%2Fs41592-018-0142-8/MediaObjects/41592_2018_142_MOESM3_ESM.avi

Spine-jRGECO1a in a cultured rat hippocampal neuron. The neuron receives uncorrelated synaptic inputs that activate a subset of spines and also produces action potentials that activate most spines synchronously. The movie was acquired at 20 frames·s^{-1} and is shown at 10 frames·s^{-1}.

2.8 Manuscript Information

2.8.1 Previously published as

A version of this chapter appeared in[21]:

L. Z. Fan, R. Nehme, Y. Adam, E. S. Jeung, H. Wu, K. Eggan, D. B. Arnold, and A. E. Cohen. All-optical synaptic electrophysiology probes mechanism of ketamine-induced disinhibition. *Nature Methods*, 15(10):823-831, 2018.

2.8.2 Acknowledgements

We thank V. Joshi, K. Williams, M. Lee and S. Begum for technical assistance. We thank V. Parot for help with analysis of spine Ca^{2+} data, S. Turney and the Harvard Center Brain Science (CBS) for loan of optical equipment, B. Sabatini (Harvard Medical School) for Rbp4-Cre mice, and C. Werley and L. Williams (Q-State Biosciences) for the mI12b plasmid. This work was supported by the Howard Hughes Medical Institute and a grant from the Gordon and Betty Moore Foundation. Y.A. was supported by a long term fellowship from the Human Frontiers Science Program and by a postdoctoral fellowship from the Edmund and Lili Safra center for Brain Sciences. D.B.A. and E.S.J. were supported by NIH grant NS-089491. K.E. and R.N. were supported by the Stanley Center and NIMH grants (5U01MH105669-04 and 1U01MH115727-01).

2.8.3 The author's contribution

Linlin Z Fan and Adam E Cohen conceived synOptopatch. Linlin Z Fan designed the synOptopatch and system, built the dual-view system and acquired the optical electrophysiology data. Linlin Z Fan and Adam E Cohen analyzed the data and wrote the paper. Linlin Z Fan, Ralda Nehme, Kevin Eggan and Adam E Cohen designed approach for implementing in human neurons. Don B Arnold, Eun S Jung and Linlin Z Fan engineered spine-jRGECO1a. Yoav Adam created QuasAr2-Citrine, designed soma localized QuasAr2 and CheRiff, and developed the brain slice imaging system. Hao Wu set up the patterned illumination system. All authors participated in revising the manuscript.

3

All-optical electrophysiology reveals excitation, inhibition, and neuromodulation in cortical layer 1

Cortical layer 1 (L1) interneurons have been hypothesized to be a hub for attentional control by integrating bottom-up and top-down inputs and controlling the underlying cortex through inhibition or disinhibition. However, it is

unclear what their activity dynamics are in awake behaving mice during sensory processing and how they integrate the different inputs to produce the output. To study the input-output properties of L1 circuit, we developed all-optical electrophysiology in awake mice – simultaneous optical manipulation and recording of membrane voltage – to probe both spiking, and subthreshold excitation (E) and inhibition (I) individually, and neuromodulation in barrel cortex L1 neurons. Our studies reveal how the L1 microcircuit process sensory input by integrating thalamocortical excitation, lateral inhibition and top-down neuromodulatory inputs. We develop a simple computational model of the L1 microcircuit which captures the main features of our data. Together, these results suggest a model for computation in L1 interneurons consistent with their hypothesized role in attentional gating of the underlying cortex. Our results demonstrate that all-optical electrophysiology can reveal basic principles of neural circuit function in vivo.

3.1 Introduction

The brain receives myriad sensory inputs. It must distinguish the relevant from the irrelevant. An input can merit attention either through its intrinsic properties (novelty, salience) or through learned associations. The sparse interneurons of neocortical Layer 1 (L1) have been hypothesized as a hub for integrating these factors and modulating the underlying cortex to control attention[92–94]. L1

interneurons receive direct thalamic[93,95,96], cortico-cortical[97,98], and neuromodulatory (cholinergic[93,94,99] and serotonergic[99,100]) inputs, the last mediated by fast ionotropic receptors. Activation of L1 interneurons exerts powerful control of underlying cortex by inhibiting deeper-lying interneurons and thereby dis-inhibiting pyramidal neurons[92–94,97]. L1 interneurons also directly inhibit pyramidal neuron apical dendrites[93,101,102]. Despite the suggestive anatomy and influence on underlying cortex, little is known about information processing within L1, especially in awake animals.

A core principle of neuronal network dynamics is maintenance of balance between excitation (E) and inhibition (I). For instance, during sensory processing in cortical layer 4 (L4) excitation driven by thalamic inputs is countered by feed-forward inhibition from parvalbumin (PV) interneurons[103,104]. L1 interneurons receive inhibitory inputs both from other L1 interneurons[96,105,106] and from deeper Martinotti cells[102]. It is not known how these inputs influence L1 activity in vivo.

Electrophysiological studies in L1 in vivo have been challenging due to the sparseness of neuronal cell bodies. While a few whole-cell patch clamp recordings have been performed in anesthetized rats[92,95], technical difficulties have prevented similar acquisitions in awake animals. Due to their multimodal, temporally precise inputs[107] and temporally precise outputs, one would like to measure the sub-threshold dynamics and spike timing of L1 neurons with high precision in voltage and time. Recent advances in genetically encoded voltage indicators

(GEVIs) enabled voltage imaging with single-neuron, single-spike resolution in hippocampus[65,26,108,109] and in superficial cortex[26,108] in vivo, opening the possibility for optical explorations of L1 circuit function in vivo.

Voltage alone does not distinguish the relative contributions of E and I synaptic inputs, yet this distinction is critical for understanding circuit mechanisms. A commonly used patch clamp technique is to inject current to achieve different levels of baseline depolarization and thereby to shift the relative driving force of E vs. I post-synaptic currents, revealing their distinct contributions[110]. We previously paired near infrared GEVIs based on Archaerhodopsin 3 (Arch) with channelrhodopsin stimulation for optical measurements of excitability in vivo (Optopatch)[65,55] and of synaptic transmission in primary culture and acute slices[21]. Here we show that optogenetic depolarization of a postsynaptic neuron during sensory processing in vivo can unmask otherwise hidden inhibitory inputs.

We combine a novel holographic structured illumination imaging system, an Archaerhodospsin-derived GEVI optimized for crosstalk-free in vivo Optopatch, and patterned optogenetic stimulation to study the role of excitatory, inhibitory and neuromodulatory inputs on the function of the cortical L1 microcircuit during sensory processing in awake mice. A simple computational model that incorporates the known morphology, electrophysiology, and connectivity of L1 interneurons captures the main features of our data and suggests an intuitive picture for novelty detection in L1.

3.2 Results

3.2.1 In vivo Optopatch with holographic patterned illumination

Archon1 is an Arch-derived GEVI with improved trafficking and brightness[35]. A soma-localized variant, SomArchon, enabled voltage imaging in vivo with good signal-to-noise ratio[109]. We made a Cre-dependent bicistronic construct for co-expression of SomArchon and a blue light-activated soma-localized channelrhodopsin, CheRiff[34]. We call this combined construct Optopatch4.

Voltage signals in tissue arise solely from the neuronal membrane. Illumination that enters the tissue but misses the membrane of interest contributes to background fluorescence and heating, but not to signal. In epifluorescence images of membrane-labeled neurons, the soma perimeter appears brighter than the center, a geometrical projection effect from viewing membranes edge-on. We thus reasoned that incident photons would most efficiently produce signal if targeted to the soma perimeter. Confocal-like excitation combined with spatially filtered emission would also minimize optical crosstalk from out-of-focus cells. We built a holographic structured illumination system, similar to Ref.[111], to achieve this precisely targeted illumination with red (λ = 635 nm) light for excitation of SomArchon (Fig. 3.1A, Fig. 3.6, Table 3.3, Methods). SomArchon fluorescence from all holographically targeted spots was recorded simultaneously on a scientific

CMOS camera. Spatial filters were applied digitally in post-processing to separate signal from background (Methods). A digital micromirror device (DMD) patterned blue illumination for targeted optogenetic stimulation (Fig. 3.1A, Fig. 3.6, Table 3.3).

We characterized the performance of the system by imaging SomArchon-expressing neurons in vivo in the cortex. Under wide-field red illumination, the cells were not visible due to high background from scattered light (Fig. 3.1B). Illumination targeted to the somas revealed individual cells (Fig. 3.1B, Fig. 3.7). Holographic membrane-targeted illumination provided substantially better optical sectioning and signal-to-background ratio than did soma-wide illumination (Fig. 3.7). The combination of SomArchon and the holographic optical system enabled recording of spontaneous action potentials with SNR 12 ± 4 (mean ± s.d., n = 16 cells) at depths between 20 and 150 μm and SNR 6.7 at a depth of $\sim$200 μm at a 1 kHz frame rate in awake head-fixed mice (Fig. 3.8, Methods).

To target expression to L1, we expressed Optopatch4 in $5HT_{3A}$R-Cre mice (Fig. 3.1C, D). This line drives expression predominantly in supragranular layers, including in $\sim$90% of L1 interneurons[93,100]. Two-photon fluorescence images of an appended eGFP tag showed membrane-localized and somatically restricted expression in L1 (Fig. 3.1E). In acute slices, targeted optogenetic stimuli evoked characteristic firing patterns in L1 neurons, including previously reported bursting adapting and late-spiking non-adapting phenotypes[105] (Fig. 3.9), though not all

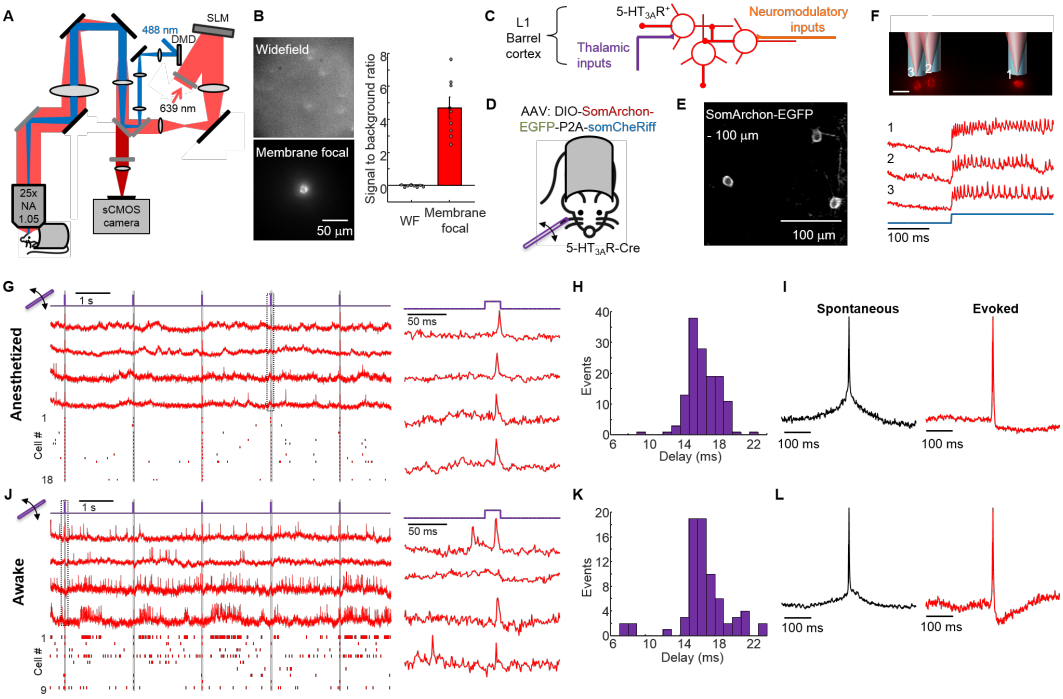

Figure 3.1: All-optical electrophysiology in L1 neurons in vivo. (**A**) Optical system for holographic structured illumination voltage imaging (red light) and micromirror-patterned optogenetic stimulation (blue light). Details in Methods. (**B**) Comparison of widefield epifluorescence and membrane-targeted holographic illumination of the same field of view containing a SomArchon-expressing L1 neuron. Scale bar 50 μm. Right: quantification of the signal-to-background ratio for the two imaging modalities. (**C**) 5-HT$_{3A}$R-positive interneurons in L1 of the barrel cortex receive sensory inputs from the thalamus, neuromodulatory inputs from higher brain regions, and lateral inhibition from other L1 interneurons. (**D**) Virus encoding a cre-dependent construct for co-expression of a voltage indicator (SomArchon-EGFP) and an optogenetic actuator (somCheRiff) were injected into barrel cortex of 5-HT$_{3A}$R-Cre mice. A glass capillary delivered small stimuli to an individual whisker. (**E**) Two-photon microscopy image of GFP fluorescence from SomArchon-EGFP in barrel cortex L1 showing good trafficking and soma localization. Scale bar: 100 μm, image depth 100 μm below dura. (**F**) Combination of patterned optogenetic stimulation (blue) and holographic illumination (red) for voltage imaging. Scale bar 20 μm. Bottom: fluorescence traces from the three indicated cells in response to a step in blue illumination in an anesthetized mouse. (**G**) Fluorescence transients in single L1 interneurons evoked by whisker stimuli (20 ms deflections at 0.5 Hz) in anesthetized mice. Left, top: examples fluorescence traces recorded at 1 kHz frame rate. Traces have been corrected for photobleaching but not otherwise filtered. Bottom: raster plot showing spikes from n = 18 neurons. Right: Fluorescence waveforms from the boxed region at left. (**H**) Distribution of delays between stimulus onset and peak of evoked spike. (**I**) Spike-triggered average waveform of spontaneous (left, n = 17 neurons) and whisker stimulus-evoked (right, n = 24 neurons) action potentials. A spike was classified as 'evoked' if it occurred within 30 ms of stimulus onset. (**J-L**) Same as G-I but in an awake mouse. Spontaneous: n = 22 neurons. Evoked: n = 21 neurons. Data in G-L recorded from 3 mice.

neurons had a clear electrophysiological classification.

In head-fixed mice, targeted optogenetic stimuli evoked spikes which were clearly resolved via holographically targeted voltage imaging in recordings acquired at a 1 kHz frame-rate (Fig. 3.1F). We measured excitability and firing properties of L1 neurons (depth < 150 μm) in mice anesthetized with isoflurane, and then later re-measured the same neurons in awake mice (Fig. 3.10). While awake mice tended to show higher excitability and more variable subthreshold dynamics, the core firing properties (e.g. bursting, adaptation) were qualitatively preserved within each cell between the two brain states (Fig. 3.10). Consistent with prior reports of in vivo patch clamp measurements in L1 interneurons [112,113], the firing patterns did not clearly resolve into distinct sub-classes. We therefore treated all measured neurons as a single population.

3.2.2 Voltage imaging of whisker stimulus-triggered activity in L1 neurons

Barrel fields corresponding to individual whiskers (B2, C2, D2) were identified by intrinsic imaging (Fig. 3.11, Methods). We then used voltage imaging to characterize the sensory-evoked responses in L1 interneurons. In both anesthetized and awake mice, brief stimuli to individual whiskers ($\sim$1 mm deflection, $\sim$8 mm from the base, 20 ms duration, repeated at 0.5 Hz, Methods) elicited excitatory post-synaptic potentials (EPSPs) and often spikes in L1 neurons in the corresponding barrel fields (Fig. 3.1G, H). The delay from stimulus onset to spike peak was 16

± 2 ms (mean ± s.d., n = 135 events, 24 neurons, 3 mice) in anesthetized mice and 16 ± 3 ms in awake mice (mean ± s.d., n = 73 events, 21 neurons, 3 mice, Fig. 3.1J, K). Similar delay and jitter were previously reported in L4 pyramidal neurons and fast-spiking neurons, both of which receive direct thalamic inputs[103].

In a comparison between spontaneous and whisker-evoked spikes, we observed striking differences in the mean subthreshold dynamics calculated via a spike-triggered average (STA, Fig. 3.1I, L). Spontaneous spikes rode atop a baseline depolarization that both preceded and followed the spike, whereas whisker-evoked spikes arose abruptly and were followed by a period of hyperpolarization (Fig. 3.1I, L). Stimulus-triggered average waveforms of whisker deflection trials that did not induce spikes also showed a depolarization followed by a hyperpolarization (Fig. 3.12). Together, these results implied that the subthreshold dynamics preceding and following spikes reflected distinct network states for spontaneous and sensory-evoked activity, rather than purely cell-autonomous effects of voltage-gated ion channels.

STA waveforms also differed between anesthetized and awake animals (Fig. 3.1I, L). For spontaneous spikes, the subthreshold depolarization was larger under anesthesia than wakefulness (anesthetized: 22 ± 2% of spike height, n = 17 neurons, 3 mice vs. awake: 10 ± 2% of spike height, n = 22 neurons, 3 mice, p = 3 × 10^{-4}, two-tailed t-test, mean ± s.e.m.). For whisker-evoked spikes, the after-spike hyperpolarization was smaller but longer lasting under anesthesia than

under wakefulness (anesthetized: 11 ± 2% spike height, n = 24 neurons, 3 mice vs. awake: 17 ± 1% of spike height, n = 21 neurons, 3 mice, p = 0.02, two-tailed t-test; anesthetized: 254 ± 15 ms recovery time vs. awake: 127 ± 14 ms, p = 1×10^{-7}, two-tailed t-test, all mean ± s.e.m). These observations are consistent with a more depolarized resting potential under wakefulness, consistent with prior reports[114].

3.2.3 Optical dissection of excitation and inhibition during sensory processing

Rapid inhibition is mediated by $GABA_A$ receptors, ligand-gated chloride channels with a reversal potential of ∼-70 mV. L1 interneurons in anesthetized rats have been reported to rest at -65 to -70 mV[95], suggesting that inhibitory inputs should have only small effects on membrane potential at rest. Borrowing from well-established patch clamp protocols[110], we reasoned that optogenetic depolarization would increase the driving force for inward chloride current, and thereby amplify the impact of $GABA_A$ receptor activation on the inhibitory postsynaptic potential (IPSP) (Fig. 3.2A,B).

In both awake and anesthetized mice, whisker stimuli in the absence of optogenetic stimulation evoked clear spikes or EPSPs in L1 interneurons, as in prior experiments (Fig. 3.2C, 3.13). Optogenetic stimuli targeted to the same cells one at a time (500ms duration, 1.8 to 21mW/mm^2, repeated at 1 Hz) reliably

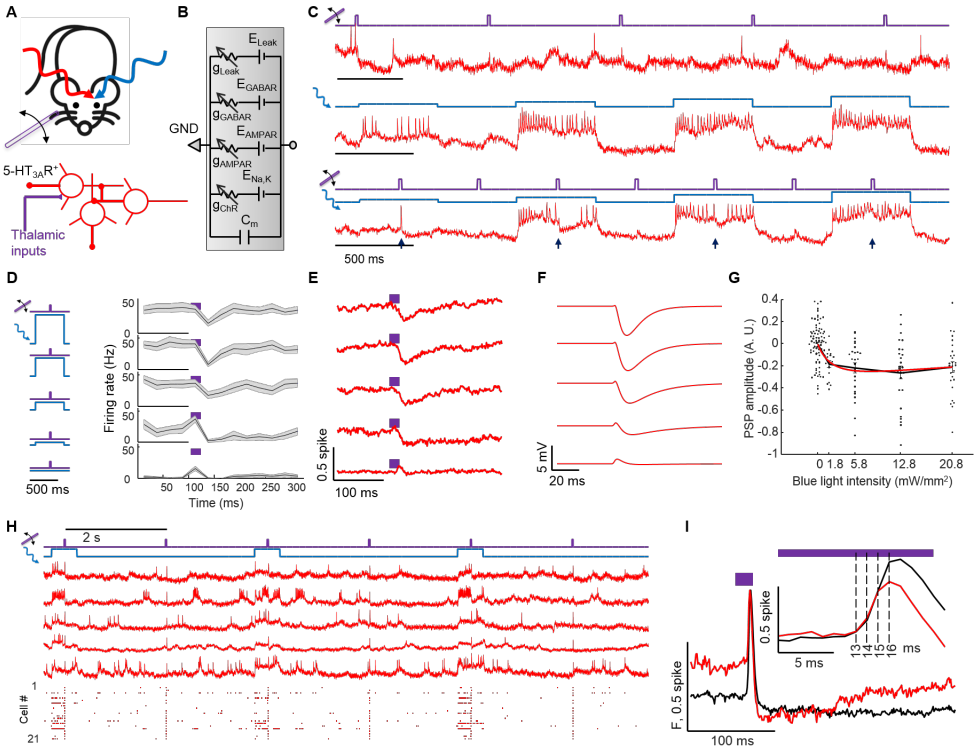

Figure 3.2: Optical dissection of excitation and inhibition in L1 interneurons in awake mice. (**A**) Whisker stimuli and single cell-targeted optogenetic stimuli were paired in 5HT$_{3A}$R-Cre mice expressing Optopatch4. (**B**) Conductance-based model of membrane potential. This simple model only contains passive conductances, with gating by light (Channelrhodopsin, ChR), glutamate (AMPAR), and GABA (GABAR). A leak conductance sets the resting potential of the cell in the absence of optogenetic or synaptic inputs. (**C**) Three recordings from a single neuron showing response to (top) whisker stimulus, (middle) optogenetic stimulus, and (bottom) simultaneous optogenetic and whisker stimuli. Arrows show whisker stimulus-evoked inhibition. (**D**) Mean spike rate evoked by whisker stimuli atop different levels of optogenetic stimulus. In the absence of optogenetic stimulation, whisker stimuli evoked precisely timed single spikes. In the presence of optogenetic stimulation, whisker stimuli suppressed spiking. The suppression decreased in amplitude and duration as the strength of the optogenetic stimulus increased. Shading represents s.e.m. from n = 27 neurons, 4 mice. (**E**) Mean whisker stimulus-evoked subthreshold waveforms at different levels of optogenetic drive. Spikes were digitally removed prior to averaging (Methods). (**F**) Simulated membrane voltage waveforms under different levels of optogenetic drive, using the model shown in (B). Excitation was assumed to lead inhibition by 2 ms. Details in Methods. (**G**) Comparison of PSP amplitude as a function of optogenetic stimulus strength with numerical simulation from a simple conductance-based model. (**H**) Repetitive measurements of whisker stimulus-evoked responses in anesthetized mice, with and without baseline optogenetic stimulation. Top: example recordings. Bottom: spike raster from n = 21 neurons, 3 mice. (**I**) Mean fluorescence responses to whisker stimulus without (black) and with (red) baseline optogenetic stimulation. Traces have been aligned to their peak. Inset: delay between onset of excitation (between 13 and 14 ms) and onset of inhibition (between 15 and 16 ms). To facilitate comparison, traces were vertically offset to align baseline values.

evoked stimulus intensity-dependent spiking. Remarkably, whisker stimuli applied during targeted single-cell optogenetic stimulation led to suppressed spiking, and hyperpolarization (Fig. 3.2C, D, E, 3.13). We quantified the sensory-evoked sub-threshold waveforms by digitally removing spikes (Methods) and calculating a stimulus-triggered average at different optogenetic stimulus strengths (Fig. 3.2E, 3.13). In both awake and anesthetized brain states, whisker stimuli had opposite effects in the absence vs. presence of baseline optogenetic stimulation, illustrating dramatic non-additivity of sensory and optogenetic inputs to the same neuron.

A simple biophysical model containing passive leak, channelrhodopsin, AMPA receptor and $GABA_A$ receptor conductances captured the main features of our data (Fig. 3.2F, G, Methods). We assumed a transient excitatory synaptic input followed shortly by a transient inhibitory input. The model confirmed that optogenetic depolarization increased the driving force for chloride, revealing the presence of otherwise hidden sensory-evoked inhibitory inputs. Depolarization via endogenous currents, as occurred in the transition from anesthesia to wakefulness, also amplified the impact of transient inhibition, explaining the difference in whisker-evoked subthreshold waveforms in Figs. 3.1I, L.

Despite lacking many details (e.g. active conductances), the biophysical model captured several subtle aspects of the subthreshold dynamics. In the anesthetized state, as the strength of the optogenetic drive increased, the sensory-evoked IPSP amplitude first increased – as explained above – but then decreased (IPSP

amplitude 29 ± 5% of spike height at low optogenetic drive (5.8 mW/cm^2) vs. 16 ± 4% of spike height at high optogenetic drive (21 mW/cm^2), n = 15 neurons, 3 mice, p = 0.001, two-sided paired-sample t-test, mean ± s.e.m.). A similar, but not statistically significant, trend occurred in the awake state (IPSP amplitude 28 ± 4% of spike height at low optogenetic drive vs. 23 ± 4% of spike height at high optogenetic drive, n = 27 neurons, 4 mice, p = 0.19, two-sided paired-sample t-test). The model revealed that these decreases were due to shunting of the membrane potential toward CheRiff reversal potential at high CheRiff conductance ($\sim$0 mV, Supplementary Text). The IPSP duration also became shorter under strong optogenetic drive in both awake and anesthetized brain states. The model ascribed this effect to a decreased membrane RC time-constant due to the high CheRiff conductance. Our simple model thus connected the complex context-dependent whisker-evoked responses in L1 interneurons to basic membrane biophysics.

3.2.4 Temporal dissection of excitation and inhibition

We next asked about the relative timing of excitatory and inhibitory inputs. We delivered whisker stimuli alternately with and without baseline weak optogenetic stimulation targeted to single neurons (5.8 mW/mm^2, Fig. 3.2H). We anticipated that the whisker-evoked responses in these two conditions would initially coincide and then would diverge upon arrival of the inhibitory inputs. We compared

stimulus-triggered average waveforms of trials that evoked spikes (Fig. 3.2I). The shape of the waveforms overlapped for the first 2ms after onset of whisker-evoked depolarization. Thereafter, the waveform in the presence of optogenetic stimulation fell below the waveform in the absence, signaling the onset of inhibition (Fig. 3.2I, inset). This finding implies a $\sim$2 ms delay between onset of excitation and inhibition, suggesting at most a difference of one synapse in the respective paths[103]. This result does not rule out the possibility that slower inhibitory signals (e.g. from $GABA_B$ receptors or polysynaptic mechanisms) also contributed to inhibition at later times.

3.2.5 Lateral inhibition

We sought to identify the source of the sensory-evoked inhibition. Patch clamp measurements in acute slices have identified inhibitory connections between L1 interneurons[96,105,106]. Since our whisker stimuli often evoked spikes in arbitrarily selected L1 interneurons, and inhibition lagged excitation by only $\sim$2 ms, we hypothesized that the rapid whisker stimulus-evoked inhibition was due to lateral connections within the L1 population.

To test this hypothesis, we performed an all-optical circuit-mapping experiment in vivo using patterned optogenetic stimulation (Fig. 3.3A). We expressed Optopatch4 in 5-HT_{3A}R-Cre mice and targeted voltage imaging to 1-3 L1 interneurons in the center of the field of view. We then defined two optogenetic stimulus pat-

terns. The first pattern comprised small disks targeted individually to the central neurons. These disks were stimulated with long pulses of blue light (500 ms, 25 mW/mm^2), with the goal to depolarize the targeted cells and to increase the driving force for inhibitory currents. The second pattern comprised an annulus (inner diameter $\sim$200 μm, outer diameter of $\sim$400 μm, Fig. 3.3B, C, Methods), surrounding the central neurons. Midway through the stimulation of the central neurons, a brief flash (20 ms, 25 mW/mm^2) was applied to the neurons in the surrounding annulus to evoke synchronized spiking of the surrounding cells.

Optogenetic stimulation of the central neurons evoked robust spiking (spike rate 41 ± 6Hz, n = 25 neurons, 3 mice, mean ± s.e.m.). Stimulation of the surrounding neurons transiently suppressed this spiking (spike rate 12 ± 4 Hz in the 25 ms following the annular flash, p = 4 × 10^{-4}, two-sided paired-sample t-test, Fig. 3.3D, E, F). The mean fluorescence waveform following the annular flash showed robust hyperpolarization of the central neurons (27 ± 3% of spike height, Fig. 3.3G, 3.14). (Control experiments without the central optogenetic stimulus revealed that the initial depolarization after the annular flash was an artifact from light scatter, Fig. 3.14). The spike patterns and subthreshold hyperpolarization dynamics in these experiments closely resembled the corresponding data for a sensory stimulus (Fig. 3.2E, F, I). These results are consistent with the model that sensory stimulation elicits rapid activation of L1 neurons followed by rapid lateral inhibition within the L1 microcircuit.

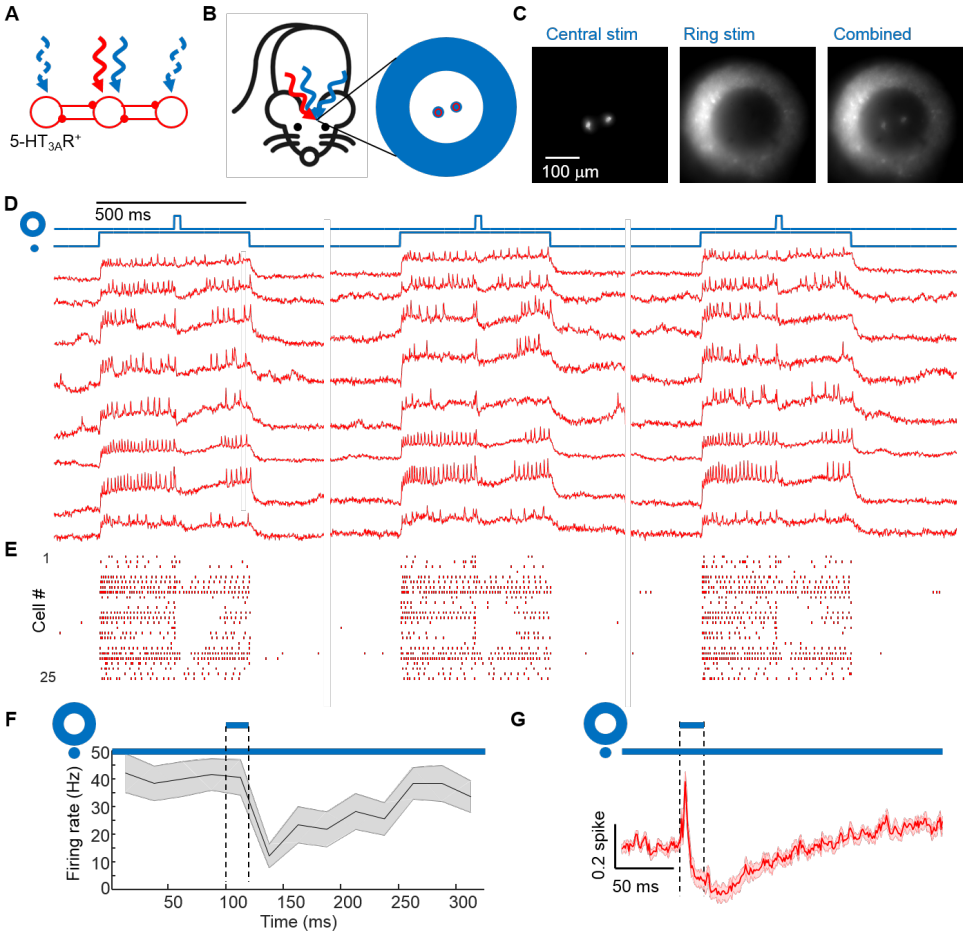

Figure 3.3: Center/surround optogenetic stimulation reveals lateral inhibition in L1. (**A**) Simple model of L1 circuit with lateral inhibition. Tonic optogenetic stimulation depolarizes the central neuron, increasing the driving force for inhibitory currents. Pulsed optogenetic stimulation of the surrounding neurons evokes lateral inhibition, revealed by voltage imaging (red) in the central neuron. (**B**) Experiment to probe lateral inhibition in L1. 5-HT$_{3A}$R-Cre mice expressed Optopatch4 in barrel cortex. Optogenetic stimuli were delivered separately to central and surrounding neurons. Voltage imaging was performed only in central neurons. Experiments were performed in anesthetized mice. (**C**) Epifluorescence images showing the illumination patterns in vivo. Scale bar 100 μm. (**D**) Fluorescence waveforms from the central neurons under center/surround optogenetic stimulation. Central stimulation depolarized the targeted neurons and evoked spiking. Surround stimulation hyperpolarized the targeted neurons and suppressed spiking. (**E**) Spike raster showing responses from n = 25 neurons, 3 mice. (**F**) Mean spike rate during central stimulation, before and after surround stimulation. Surround stimulation caused spike rate to drop from 40.5 $\pm$ 6.3 Hz to 12.3 $\pm$ 4.1 Hz, n = 25 neurons, 3 mice (p = 4×10^{-4}, two-sided paired-sample t-test). Shading represents s.e.m. (**G**) Mean subthreshold voltage during central stimulation, before and after surround stimulation. Surround stimulation caused inhibition in the central neuron. The initial spike in membrane voltage in the central neuron was due to scattered light from the surround which drove direct CheRiff activation. Shading represents s.e.m..

3.2.6 Neuromodulation

Finally, we explored the role of neuromodulatory activity on L1 dynamics (Fig. 3.4A). A mild air puff to the face has been shown to activate cholinergic neurons in basal forebrain[107], and these neurons are known to innervate cortical L1[94,115]. We imaged L1 neurons in awake mice while delivering a mild air puff (100 ms duration, $\sim$5 psi) to the ipsilateral eye (to avoid incidental stimulation of whiskers associated with the imaged neurons, Fig. 3.4B). In 15 of 21 L1 interneurons, the air puff evoked a clear depolarization. In 6 of these neurons the air puff evoked one or more spikes and in 3 of these neurons, the air puff evoked a barrage of firing that lasted $\sim$1 s, strikingly different from the precisely timed single spikes evoked by whisker stimulation (Fig. 3.4C). When the air puff was applied in the middle of an epoch of single cell-targeted optogenetic stimulation (500ms, 5.8mW/mm^2), we did not observe a significant change in mean spike rate of the optogenetically targeted neurons (Fig. 3.4D). Some neurons increased their spike rate while others decreased their spike rate (see e.g. Fig. 3.4C, second and fourth traces).

To resolve the subthreshold dynamics, we digitally removed spikes and calculated the air puff-triggered average across all imaged neurons. In the absence of optogenetic stimulation, the air puff evoked a depolarization that grew over $\sim$100 ms, reached 20 ± 3% of spike height, and decayed with a $\sim$1600 ms

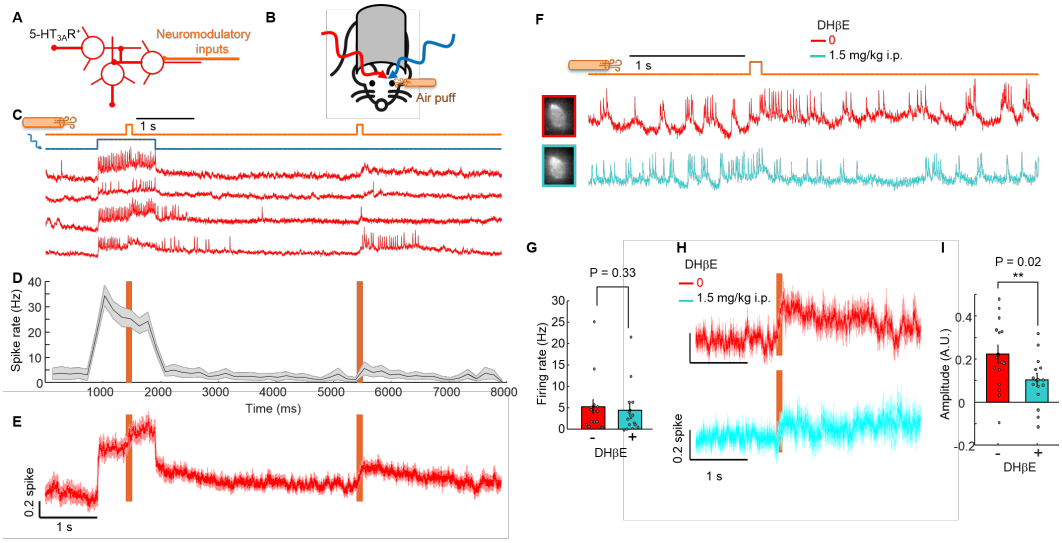

Figure 3.4: Cholinergic inputs drive excitation in L1 interneurons. (**A**) Schematic showing neuromodulatory inputs driving L1 interneurons. (**B**) Experiment to probe neuromodulatory effects in L1. Optopatch measurements were performed in barrel cortex L1 interneurons of awake 5-HT$_{3A}$R-Cre mice while a mild air puff was applied to the ipsilateral eye. (**C**) Fluorescence recordings from single cells showing responses to air puff stimulation in the presence and absence of baseline optogenetic stimulation. (**D**) Mean spike rate during air puff stimulation with and without baseline optogenetic depolarization (n = 21 neurons, 4 mice). (**E**) Mean subthreshold response to air puff. Spikes were digitally removed from the traces. (**F**) Effect of a cholinergic blocker, DHβE, on the air puff response. Paired measurements were performed returning to the same cell before and after drug administration. (**G**) DHβE did not significantly affect spontaneous spike rate. (**H**) Mean subthreshold responses to air puff before and after administration of DHβE. (**I**) DHβE significantly reduced the subthreshold response to air puff, as quantified by the amplitude of the subthreshold response to air puff. Data in (G – I) from n = 16 neurons measured before and after drug administration, 3 mice.

recovery time (Fig. 3.4E). In the presence of single-cell targeted optogenetic stimulation, the air puff evoked a depolarizing transient in the subthreshold voltage of the optogenetically targeted cell (Fig. 3.4E), opposite to the hyperpolarizing transient evoked by a whisker stimulus under comparable conditions (e.g. Fig. 3.2C). Together, these results implied that the air puff evoked a predominantly excitatory input to the L1 microcircuit.

The α4 nicotinic acetylcholine receptor is highly expressed in L1 interneurons[93,116], so we hypothesized that this receptor was mediating the neuromodulatory response. We made paired recordings of the same L1 interneurons before and after systemic administration of the α4 nAChR blocker dihydro-β-erythroidine hydrobromide (DHβE, 1.5 mg/kg i.p., Fig. 3.4F). This drug did not significantly affect the spontaneous spike rate (Fig. 3.4G), but it largely suppressed the air puff-induced depolarization, consistent with a cholinergic mechanism for this effect (amplitude, A. U., 0.22 ± 0.04 before vs 0.10 ± 0.03 after drug, n = 15 neurons, 3 mice, p = 0.02, two-sided paired-sample t-test, Fig. 3.4H, I).

3.2.7 Numerical model of L1 microcircuit

Prior studies have characterized the anatomical and electrophysiological properties of L1 interneurons in detail[93,96,105,95], and modeling efforts have led to anatomically and biophysically detailed simulations[112,117]. We sought to develop a numerical model of the L1 microcircuit that incorporated our data and prior

information. Such a model should be able to reproduce our experimental results and to generate testable predictions for future experiments. Rather than aiming for numerical precision, we sought to build a simple model which captured the main features of the data in an intuitive and computationally efficient format.

A variety of classification schemes have been proposed for L1 neurons based on electrophysiology, morphology, or molecular markers [102,106]. Here we consider two broad classes based on firing properties and morphology. Elongated neurogliaform cells (eNGC) are slow to spike near threshold, do not adapt, and primarily synapse within L1 [105,106]. Single bouquet-like (SBC-like) cells burst readily, quickly adapt, and primarily dis-inhibit underlying cortex [105,106]. Both cell types receive thalamic and neuromodulatory inputs [96]. Since the SBC-like cells do not synapse within L1, the dynamics can be split into the mutually inhibitory eNGC network, driven by thalamic and neuromodulatory inputs, and the SBC-like output, driven by the eNGC network, thalamic, and neuromodulatory inputs (Fig. 3.5). For present purposes we neglect cortico-cortical connections.

To capture the distinct firing properties of L1 interneurons, we used Izhikevich-type models [118,119], with parameters tuned to match the observed spiking properties of eNGC and SBC-like interneurons (Fig. 3.5B, Methods, Table 3.1). Though not explicitly conductance-based, Izhikevich models can accommodate synaptic inputs as ohmic conductances [120], a critical feature for recapitulating the non-additivity of sensory and optogenetic stimuli. We used literature values to set the

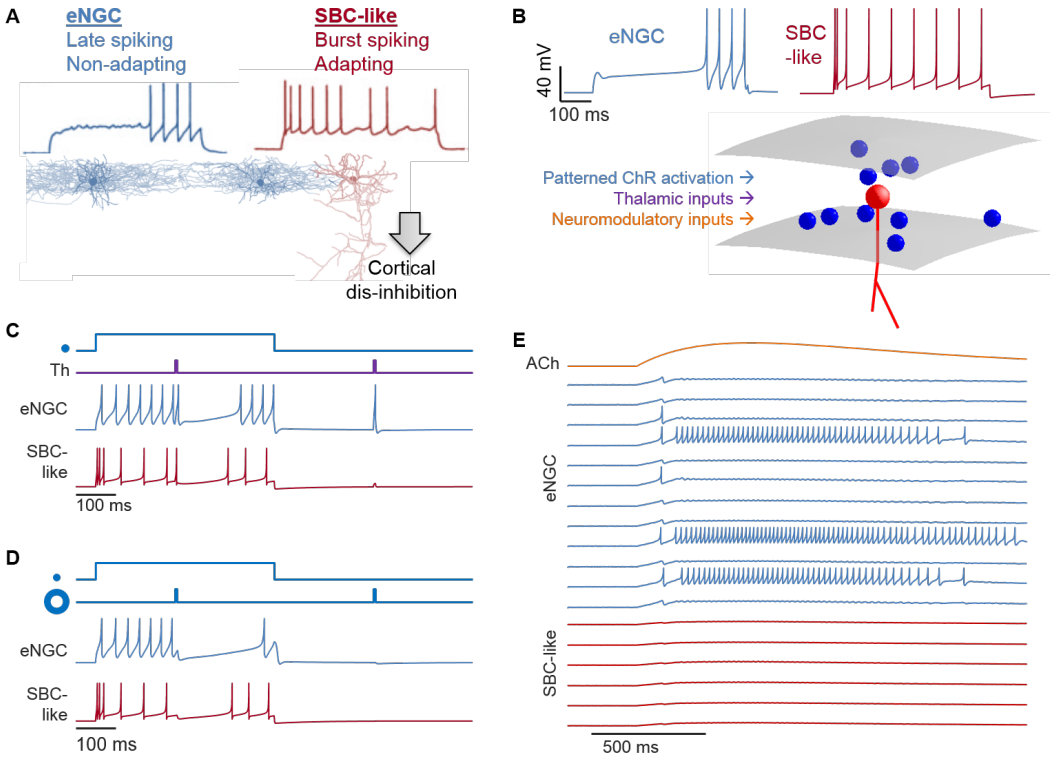

Figure 3.5: Computational model for the L1 micro-circuit. (**A**) Characteristic morphology and spiking patterns of L1 interneurons. Manual patch clamp recordings were acquired near rheobase. The eNGC cells form a mutually inhibitory network within L1. Downward-projecting SBC-like neurons receive inhibition from the eNGC network, and in turn dis-inhibit underlying cortex. Electrophysiology traces adapted from (Chu et al.J. Neurosci 23 (2003): 96-102.) and neuronal morphologies from (Jiang et al. Science 350 (2015): aac9462). (**B**) Model of L1 microcircuit. Neurons of both sub-types were randomly distributed within a disk-shaped barrel. Parameters of Izhikevich-type models were adjusted to mimic the characteristic firing patterns. Cells of both classes received optogenetic, thalamic, and neuromodulatory inputs. (**C**) Simulation of a complete L1 network for a single barrel (51 neurons). The network was exposed to network-wide thalamic excitation and single-cell targeted optogenetic stimulation. The traces show two simulations in which the optogenetic stimulation and voltage measurement were targeted either to an eNGC cell or to an SBC-like cell. Thalamic excitation alone induced spikes or sub-threshold excitation. In the presence of targeted optogenetic stimulation, thalamic excitation suppressed spiking. Compare to Figs. 3.2C, 3.13. (**D**) Simulation of an L1 network response to tonic optogenetic stimulation of a central neuron and pulsed optogenetic stimulation of the surrounding neurons. The traces show two simulations in which the central stimulation was targeted either to an eNGC cell or to an SBC-like cell. Surround stimulation hyperpolarized the targeted neurons and suppressed spiking. Compare to Fig. 3.3D. (**E**) Simulation of an L1 network response to a graded neuromodulatory input activating an excitatory conductance in all neurons. A few eNGC neurons spiked first, suppressing spiking of the rest of the network. The increased network inhibition blocked spiking of the output SBC-like neurons. The plots show a randomly selected subset of the 51 neurons in the circuit. Compare to Fig. 3.4C.

approximate density, length-scale, strength, and duration of synaptic connections (Methods, Table 3.2, Figs. 3.15-3.16). Detailed structural studies in rats have shown that each barrel contains ~40-50 L1 interneurons, consistent with our estimates based on published micrographs from mice[108]. The lateral extent of the axonal and dendritic trees is ~200 – 250 μm, comparable to the size of the barrel. Consistent with this broad arborization, patch clamp measurements in slices found that most nearby pairs of L1 eNGC interneurons had synaptic connections[106,121]. We assumed that neurons did not synapse onto themselves. The time-dependent strengths of optogenetic, thalamic, and neuromodulatory inputs were varied to mimic different experimental conditions.

To characterize the single-cell models, we simulated individual eNGC and SBC-like neurons exposed to combinations of tonic excitatory and inhibitory inputs. Both cell types showed Type II firing patterns[122], i.e. abrupt onset of spiking during smoothly increased excitatory drive (Fig. 3.17). We simulated single-cell behavior under step-wise increasing optogenetic stimulation and with pre-specified transient excitatory (mimicking thalamic) and inhibitory (mimicking local network) inputs. The simulated cells produced spike patterns and subthreshold dynamics (Fig. 3.17) that resembled the corresponding experimental results (Figs. 3.2C, 3.13).

We then simulated a full L1 network for a single barrel: 51 L1 interneurons (34 eNGC, 17 SBC), randomly distributed in a region 300 μm on edge and 150

μm thick, with biologically plausible synaptic weights. Thalamic excitation and targeted optogenetic stimulation remained as input parameters, while inhibition was solely due to internal network dynamics. The simulated dynamics (Fig. 3.5C) closely matched the experimental results (Fig. 3.2C, 3.13). At baseline the model yielded sensory-evoked sub-threshold depolarization or single spikes. In the presence of optogenetic drive, the model yielded sensory-evoked single spikes followed by hyperpolarization and spike suppression. We then reproduced the donut stimulation experiments from Fig. 3.3 (Methods, Fig. 3.18). As anticipated, when a central neuron was optogenetically depolarized, optogenetic activation of surrounding neurons induced hyperpolarization and suppressed spiking of the central neuron (Fig. 3.5D).

The experimental responses to the air puff stimuli were highly heterogeneous (Fig. 3.4C), an effect which we initially ascribed to variability in neuron sub-types or to specific patterns of connectivity not included in our model. Despite the overly simplistic model, we studied how the simulated network responded to neuromodulatory inputs. We modeled neuromodulation as a gradual activation of an excitatory conductance in all L1 interneurons (Methods). To our surprise, the simulations of a nearly homogeneous eNGC network recapitulated the highly heterogeneous responses observed experimentally (Fig. 3.5E), and even captured the approximate proportions of cells showing subthreshold depolarizations, isolated spikes, and tonic firing.

This surprising symmetry breaking (emergence of qualitatively distinct responses from a nearly homogeneous population) was explained by the mutually inhibitory nature of the L1 eNGC network. A few neurons, by chance, spiked first. These drove inhibition in their neighbors, suppressing spiking in response to the tonic excitation. Thus the highly heterogeneous single-cell responses to neuromodulatory inputs can be explained by an emergent network phenomenon and do not require sub-populations with specific wiring or electrophysiological properties (though our experiments do not inform whether functionally distinct sub-populations contribute to the heterogeneous responses in vivo).

Based on the success of the simple model, we suggest an intuitive picture for how sensory and neuromodulatory inputs interact in L1. We propose that a transient thalamic input initially activates the output (SBC-like) cells, while a sustained thalamic input predominantly drives eNGC-mediated inhibition and suppresses the output. Numerical simulations showed that this is the case within the model (Fig. 3.19). In this picture, the distinct intrinsic firing properties of the different L1 sub-types play a crucial role in tuning the circuit as a novelty detector. Our model predicts that under weak neuromodulatory excitation, the network becomes sensitized to thalamic inputs because all cells are closer to threshold; but under strong neuromodulatory excitation the emergence of sustained spiking in a subset of eNGC cells may suppress network responses to thalamic inputs. This is a testable prediction.

The L1 microcircuit is particularly suited for computational modeling due to the relative simplicity of the internal connectivity, the absence of recurrent excitation, and the sparse distributions of cells. Our computationally efficient model is readily applied to large-scale simulations. These simulations could be used to make testable predictions of how the L1 microcircuit would respond to various combinations of sensory and neuromodulatory inputs, patterned in space and time. While our simple model lacks many features of the real circuit, we suggest that this model is a useful starting point from which to add more realism.

3.3 Discussion

Our experiments revealed that lateral inhibition among L1 interneurons mediates precisely timed single-spike responses to abrupt sensory inputs. A striking aspect of these findings was that the same sensory input (a whisker deflection) could depolarize and elicit spikes in a hyperpolarized neuron, but hyperpolarize and suppress spikes in a depolarized neuron. This observation highlights the importance of considering electrophysiological context when interpreting functional data recorded in vivo.

Remarkably, this highly nonlinear effect (opposite sign response depending upon initial membrane voltage), was quantitatively explained by a simple biophysical model which only contained idealized batteries and linear, ohmic conductances.

The appearance of nonlinear responses in a linear membrane model is explained by the fact that, even in a linear model, the voltage is a nonlinear function of the conductances (see Supplementary Text). The oft-used approximation that excitatory and inhibitory inputs simply add to make a net synaptic current is clearly violated.

While our experiments used a channelrhodopsin to drive depolarization, ionotropic AMPA receptors[123], acetylcholine receptors[124], serotonin receptors[125] and channelrhodopsins[126] all have similar current-voltage relations, implying that baseline activation of any of these receptors could switch the sensory-evoked response of an L1 neuron from excitation-dominated to inhibition-dominated.

Our results further showed that thalamic and neuromodulatory excitation converge in L1 neurons, albeit with different temporal profiles and consequently different network effects. Whereas rapid thalamic excitation led to synchronous spiking followed by network inhibition, slower neuromodulatory excitation drove tonic spiking in a subset of cells which suppressed spiking in the majority.

Experiments in vivo[94] and in slices[127] have shown that cholinergic stimulation elicits complex effects on L1 interneurons, but how these effects modulate sensory-evoked responses in vivo remains to be determined. A clear goal for future work will be to characterize the role that each subclass of L1 interneurons plays in integration of sensory, neuromodulatory, and cortico-cortical inputs.

All-optical electrophysiology can report both the nature of the synaptic inputs

(E vs. I) and the spiking output of a cell, revealing the transformation that the cell implements. Optogenetic stimulation and voltage imaging in distinct neural populations can reveal cell type-specific connections and their role in circuit dynamics. While we focused on rapid sensory processing, these tools may also prove useful in studies of neural plasticity, development and disease mechanisms.

3.4 Methods

3.4.1 Design of Optopatch4

Optopatch4 construct (SomArchon-eGFP-P2A-somCheRiff) was cloned into an AAV vector with Cre-dependent expression driven by the hSyn promoter.

LZF1735 pAAV_hSyn-DiO-SomArchon-eGFP-P2A-somCheRiff (Addgene #126512)

LZF1733 pAAV_CAG-FLEX-SomArchon-eGFP

High-titer AAV2/9 virus with Optopatch4 (1.74×10^{13} GC/mL) was obtained from the Janelia Farm Vector Core. High-titer AAV2 virus with LZF1733 (6.30×10^{12} GC/mL) was obtained from the UNC Vector Core. High-titer AAV9 virus with CKII(0.4)-Cre (2.8×10^{13} GC/mL) was obtained from UPenn Vector Core.

3.4.2 Optical system for holographically targeted voltage imaging and patterned optogenetic stimulation

The optical system combined a red laser (λ = 639 nm) path for holographic targeted illumination voltage imaging, a blue laser (λ = 488 nm) path for micromirror-patterned optogenetic stimulation, a two-photon (2P) path for structural imaging, and a wide-field epifluorescence imaging path.

3.4.2.1 Red laser path

A red laser (CNI Inc., MRL-FN-639, λ = 639 nm, 700 mW single transverse mode) was coupled into the setup via a photonic crystal polarization maintaining fiber (NKT Photonics, LMA-PM-15). The fiber output was collimated with an f = 100 mm focal length lens (Thorlabs, AC254-100-A-ML) to form a beam with approximately $\sim$10 mm diameter. The polarization of the beam was set with a zero-order half-wave plate. The beam was directed onto a holographic reflection-mode liquid crystal spatial light modulator (SLM, Meadowlark 1920SLM VIS) with a resolution of 1920 x 1152 pixels. Zero-order diffraction was blocked by a home-made anti-pinhole comprised of a dot of solder on a glass slide, placed in a plane conjugate to the sample image plane. The SLM was re-imaged onto the back-focal plane of the objective via a series of relay optics. The objective lens was a 25× water immersion objective, numerical aperture 1.05 (Olympus

XLPLN25XWMP2). A mechanical shutter blocked the red laser between data acquisitions. A series of OD filters were placed after the red laser for modulating intensity.

In the first generation of the setup, we used a variable focal length camera lens (Sigma macro 18-200 mm) to control the magnification of the SLM at the back focal plane of the objective. Demagnifying the SLM decreased the effective numerical aperture of the illumination at the sample, leading to bigger spots in the sample, but also to a larger region that could be targeted with red light. In the second-generation system, we used a fixed lens after the SLM to minimize aberrations. All relay lenses are specified in Table 3.3.

The SLM device was controlled by custom software. A user specified a set of lines for the SLM to target by drawing on a wide-field epifluorescence image or a 2P fluorescence image. These lines were discretized into a set of spots. The SLM phased pattern was calculated using the Gerchberg-Saxton algorithm.

Red laser intensity was $\sim$ 3 mW per cell for in vivo imaging, $\sim$ 1 mW per cell for acute slice imaging.

3.4.2.2 Blue laser path

A blue laser (Cobolt, 06-01 series, λ = 488 nm, 60 mW) was modulated in intensity via an acousto-optic tunable filter (AOTF; Gooch and Housego TF525-250-6-3-GH18A). The beam was focused into a single-mode optical fiber. The

output was collimated with an f = 60 mm focal length lens (Thorlabs, AC254-060-A-ML) to form a beam with approximately a $\sim$17 mm diameter. The beam was then sent to a digital micromirror device with a resolution of 1024 x 768 pixels (DMD, Vialux, V-7001 VIS). The patterned blue beam was combined with the patterned red beam via a dichroic mirror. The DMD was re-imaged onto the sample at a magnification such that one DMD pixel corresponded to 0.62 μm in the sample plane. The DMD optical system enabled patterned blue light stimulation across a field of view of $\sim$450 x $\sim$520 μm.

The DMD was controlled by custom software. For excitability measurement, a pixel bitmap was preloaded onto and projected from the DMD. For lateral inhibition experiments, pixel bitmaps were loaded into the on-board RAM and digital clock pulses triggered the DMD to sequence through the pre-defined set of exposure patterns.

3.4.2.3 Wide-field fluorescence imaging path

The image was relayed from the objective to the camera via a series of three lenses. The final image formation step was performed by a 4x objective (Olympus XLFLUOR 4X/340) serving the role of the tube lens. Fluorescence was collected on a scientific CMOS camera (Hamamatsu ORCA-Flash 4.0). The final magnification of the optical system was 16.7, corresponding to 0.39 μm in the sample plane per camera pixel.

Fluorescence from the sample was separated from the blue and red excitation beams via a dichroic mirror (Di03-R405/488/561/635-t3-40x55). An emission filter (Semrock 635 nm long-pass, BLP01-635R-25) further separated SomArchon fluorescence from scattered excitation light. An IR-blocking emission filter (Semrock, FF01-842/SP-25) was placed for blocking scattered infrared excitation light.

All movies are acquired at 1 kHz. To image at 1 kHz, the camera region of interest (ROI) was restricted to typically 200 rows, centered on the image-sensor midline.

The imaging system was designed for a magnification lower than the nominal 25x of the objective for two reasons. First, lower magnification increased the number of neurons that could be imaged simultaneously onto the limited detector area accessible at 1 kHz. Second, by concentrating sample photons onto as few camera pixels as possible, we sought to minimize the contribution from camera electronic noise, so that all signals would be in the shot noise-limited regime.

3.4.2.4 Two-photon imaging path

Light from a femtosecond tunable pulsed infrared laser (Spectra Physics DeepSee) was sent to a pair of galvo mirrors (Cambridge Technologies 6215H). The galvos were re-imaged onto the back focal plane of the objective via an optimized scan lens (Thorlabs, SL50-CLS2) and tube lens (Thorlabs, TL200-CLS2). The visible (blue and red) and near-infrared beams were combined using a 785 nm long-pass

dichroic mirror (Semrock, Di03-R785-t3-40x55). GFP fluorescence was directed to the 2P detection path via a removable 550 nm short-pass dichroic. Scattered excitation light was blocked by a 633 nm short-pass emission filter, an IR-blocking emission filter (BSP01-785R-25) and a band-pass emission filter (FF03-525/50-25). A pair of lenses (focal lengths 75 mm and 16 mm) re-imaged the back-aperture of the objective onto a photomultiplier tube (Hamamatsu, H11706P-40). The output of the photomultiplier was amplified and low pass filtered through an amplifier unit (Hamamatsu C7319) and then digitized.

3.4.2.5 Control software

The entire setup was controlled by custom software written in LabView. Interfacing was via a National Instruments DAQ (NI PCIe-6363).

The software contained routines for registration of the DMD, SLM, 2P microscope coordinates to the camera via affine transformations. The camera served as the global reference coordinate system.

Experimental protocols were specified by a set of images (to the SLM and the DMD), output waveforms (to the galvos, the AOTF, the shutters, the update clock on the DMD, the piezo whisker stimulator, and the air puff controller), and analog input streams (from the PMT, the camera exposure clock, and a patch clamp electrophysiology setup not used in the present work).

The Hamamatsu camera uses an internal 100 kHz clock to synchronize image

row readout. We found that when the camera exposure times were triggered by the DAQ in synchronous mode, the camera rounded the exposure time to the nearest 10 μs, leading to 1% jitter in exposure time for 1 kHz imaging. To address this noise source, we used a custom firmware upgrade to access the 100 kHz camera clock. This clock became the master clock for the DAQ system, and all analog and digital input/output functions were synchronized to the camera clock.

3.4.3 Imaging in acute slices

All procedures involving animals were in accordance with the National Institutes of Health Guide for the care and use of laboratory animals and were approved by the Institutional Animal Care and Use Committee at Harvard University.

3.4.3.1 Virus injection for acute slice measurements

Virus comprising AAV2/9 hSyn-Dio-SomArchon-eGFP-P2A-somCheRiff (1.74×10^{13} GC/mL) was diluted in PBS and injected at a final titer of $\sim2\times10^{12}$ GC/mL.

$5HT_{3A}R\text{-}Cre^{+/-}$ mice were crossed with wild-type C57BL/6 mice. Pups were cryo-anesthetized at P0-P2 and immobilized dorsal side up under a stereotaxic microscope. Injections were made using home-pulled micropipettes (Sutter P1000 pipette puller), mounted in a microinjection pump (World Precision Instruments Nanoliter 2010) controlled by a microsyringe pump controller (World Precision

Instruments Micro4). The micropipette was positioned using a stereotaxic instrument (Stoelting Digital Mouse Stereotaxic Instrument). Pups were injected in the left hemisphere, 1 mm lateral and 1.2 mm anterior to lambda. Starting at a depth of 0.3 mm beneath the surface of the skull, virus injections (40 nL, 1 nL/s) were performed at 0.1 mm increments as the pipette was withdrawn. Pups were placed back in their home cage once they were awake.

3.4.3.2 Genotyping

Genotyping for $5HT_{3A}R$ was performed with the PCR primer pairs: Cre 5': 5' TAT CTC ACG TAC TGA CGG TG 3' and Cre 3': 5' AGA CTA ATC GCC ATC TTC CAG C 3' to yield a 500 bp band from Cre.

3.4.3.3 Acute slice preparation

Acute brain slices were prepared from P16–P28 $5HT_{3A}R\text{-}Cre^{+/-}$ mice. The mice were anesthetized by isoflurane and then perfused with carbogen (95% O_2, 5% CO_2)-saturated ice-cold slicing solution with the following composition (in mM): 110 choline chloride, 2.5 KCl, 1.25 NaH_2PO_4, 25 $NaHCO_3$, 25 glucose, 0.5 $CaCl_2$, 7 $MgCl_2$, 11.6 Na-ascorbate, and 3.1 Na-pyruvate. Mice were then decapitated and the brains were rapidly coronally sliced with 300 μm thickness on a vibratome (Leica VT 1200S).

Slices were incubated for 45 min at 34 °C in a carbogenated artificial CSF (ACSF)

with the following composition (in mM): 127 NaCl, 2.5 KCl, 1.25 NaH_2PO_4, 25 $NaHCO_3$, 25 glucose, 2 $CaCl_2$, and 1 $MgCl_2$. The osmolarity of all solutions was adjusted to 300–310 mOsm and the pH was maintained at 7.3 under constant bubbling with carbogen.

3.4.3.4 Imaging acute slices

Measurements were conducted in ACSF at 23 °C under ambient atmosphere. The slice was immobilized in a slice recording chamber using a slice anchor (Warner Instruments, SHD-40/2). ACSF, perfused with carbogen, was flowed through the chamber at a rate of 2 mL/minute.

3.4.4 Cranial windows and virus injections

3.4.4.1 Cranial window surgery and virus injection for imaging barrel cortex L1

Virus comprising AAV2/9 hSyn-Dio-SomArchon-eGFP-P2A-somCheRiff (1.74×10^{13} GC/mL) was diluted in PBS and injected at a final titer of $\sim3\times10^{12}$ GC/mL.

The procedure for surgery and imaging in barrel cortex L1 followed the protocol from Andermann[128]. 35-60-day-old heterozygous $5HT_{3A}$R-Cre mice (male and female) were deeply anesthetized with 2% isoflurane and maintained with $\sim$1% isoflurane throughout the surgery. Eyes were kept moist using ophthalmic eye

ointment. Body temperature was continuously monitored and maintained at 37 ^{o}C using a heating pad (WPI, ATC2000). The skull was exposed and thoroughly dried and a 3 mm round craniotomy (3.3 – 3.4 mm lateral, 1.6 mm caudal of bregma) was opened using a biopsy punch (Miltex). Virus was then injected in 4 - 8 locations in the center of the craniotomy. Starting at a depth of 0.2 mm beneath the surface of the dura, virus injections (60 nL, 1 nL/s) were performed at 0.1 mm increments as the pipette was withdrawn. Brain surface was kept moist with saline throughout the injection.

A window was prepared prior to the surgery and comprised two 3 mm round #1 cover glasses and one 5 mm round #1 cover glass (Harvard apparatus) cured together with UV curable adhesive (Norland Products, NOA 81). Following the virus injection, the window was then placed covering the barrel cortex and cemented to the skull with dental cement (C&B metabond, Parkell, No. 242-3200). After the window cured, a titanium headplate (similar to the design in Ref.[128]) was glued around the window and any exposed skull was covered with dental cement. Animals were returned to their home cage for recovery and treated for 3 days with Carprofen (5 mg/kg) and Buprenorphine (0.1 mg/kg) twice a day. To avoid damage to the implant, mice were housed in separate cages.

3.4.4.2 Cranial window surgery and virus injection for L1-3 imaging (Fig. 3.9)

Virus comprised AAV2 CAG-FLEX-SomArchon-eGFP (final titer $\sim$0.5×10^{12} GC/mL) mixed with CKII(0.4)-Cre virus (UPenn vector core, final titer $\sim$1×10^{11} GC/mL).

The procedure for surgery and imaging in visual cortical L1-3 followed the same protocol as above, except that 35-60-day-old wild-type C57BL/6 mice (male and female) were used. The coordinates for the 3 mm round craniotomy were 2.4 mm lateral and 2.7 mm caudal of bregma. Virus was then injected in 4 - 8 locations in the center of the craniotomy. Starting at a depth of 0.3 mm beneath the surface of the dura, virus injections (60 nL, 1 nL/s) were performed at 0.2 mm increments as the pipette was withdrawn.

3.4.5 Tracking, whisker stimulation, intrinsic imaging and in vivo voltage imaging

An IR LED light (850 nm) was placed in front of the animal. A PointGrey camera (GS3-U3-51S5M-C, Mono Grasshopper3 USB 3.0 Camera) with a Fuji lens (Fuji Photo Optical 1:1.4/25 Fujinon-TV Camera Lens) and an IR-passing optical filter (Thorlabs, FB850-40) was placed on the side to track the animal's face (whisker motion and eye blinks) during data acquisitions.

3.4.5.1 Whisker stimulation

An individual whisker (typically B2, C2 or D2; other whiskers were trimmed to prevent direct contact with the glass pipette) was inserted into a glass pipette glued to a piezoelectric actuator. The actuator was connected to an amplifier (Krohn-Hite 7602M) and controlled by the DAQ.

3.4.5.2 Intrinsic imaging

Intrinsic imaging was performed on the same setup as described above. A 4x objective (Olympus XLFLUOR 4X/340) was used to image the entire 3 mm cranial window. The whisker stimulation was 10 Hz for 4 s with a 16 s interstimulus interval. A red LED (625 nm) illuminated the window surface from the side. Reflected light was imaged onto the camera at 10 Hz frame rate. A decrease in reflectance from the brain indicated the barrel, which could be localized relative to the blood vessel pattern as visualized with 488 nm illumination.

3.4.5.3 Imaging anesthetized animals

Imaging started 3 weeks post-surgery. Mice were lightly anesthetized (0.7–1% isoflurane), head-fixed under the upright microscope using the titanium head plate and held in a body tube. Eyes were kept moist using ophthalmic eye ointment. Body temperature was continuously monitored and maintained at 37 ^{o}C using a

heating pad (WPI, ATC2000). A typical imaging session lasted 1–2 hours, and then animals quickly recovered and returned to their home cage. Recordings targeting L1 neurons in vivo were performed at a depth < 150 μm in both anesthetized and awake animals.

3.4.5.4 Habituation and imaging awake animals

Habituation started 2 weeks post-surgery. Each animal was acclimated to the head restraint in a body tube for at least 3 days before starting the imaging sessions. For imaging in awake animals, a 3D-printed paw blocker was placed in front of the forepaws to prevent them from pushing away the glass pipette for whisker stimulation.

3.4.5.5 Air puff

The timing of the air puff was controlled by a solenoid valve (WPI). The strength of the air puff was set $\sim$ 5 psi and controlled by a pressure regulator (Festo, pressure regulator LRP-1/4-4). The air puff was delivered through a blunt needle at $\sim$ 5 mm from the eye ipsilateral to the brain hemisphere used for voltage imaging (to avoid spurious whisker stimulation arriving in the imaged barrels). Air pressure and needle position were adjusted to achieve an air puff strength just strong enough to evoke an eye blink response and increase the pupil diameter.

3.4.5.6 DHβE administration

To modulate cholinergic signaling, dihydro-β-erythroidine hydrobromide (DHβE, Tocris; 2349) was diluted in saline. The drug was administered systemically (1.5 mg/kg i.p.). Optopatch and air puff measurements were performed before, and then 30 min. after drug administration, on the same sets of cells. The experiment was performed on each animal twice, on successive days.

3.4.6 Center/surround optogenetic stimulation

For lateral inhibition experiments, we defined two optogenetic stimulus patterns. "Central masks" covered individually the cell bodies of 1 – 3 neurons at the center of the field of view. We calculated the geometrical centers of these masks individually. The mean of these centers was set as the coordinates for the center for the surrounding "annulus mask".

The annulus inner radius was set to be $\sim$100 μm from the most non-centered central mask. This distance was selected to minimize the impact of scattered light from the annulus mask. The outer radius of the annulus mask was set as the largest value at which the annulus would be contained within the FOV. Typical outer radii were $\sim$200 μm.

The image sequence was composed of three composite masks: (1) central masks only; (2) central mask and annulus mask together; (3) annulus mask only.

These masks were preloaded into the on-board RAM and digital clock pulses triggered the DMD to sequence through the pre-defined set of exposure patterns.

3.4.7 Data analysis

Data were analyzed with homemade code written in MATLAB.

3.4.7.1 Corrections for photobleaching and motion artifacts

Movies were first corrected for motion using the NoRMCorre algorithm [129]. Movies were then corrected for photobleaching by dividing the movie by an exponential fit of the mean fluorescence.

3.4.7.2 Image segmentation and waveform extraction

We divided the movie into sub-movies based on patterns of illumination from the DMD masks and performed activity-based image segmentation separately in each sub-movie. Whereas subthreshold voltages could be correlated between a cell and out-of-focus background cells, we assumed that spiking was not correlated with background, and furthermore that the spatial footprint associated with spiking would be the same as for true subthreshold dynamics. To remove subthreshold signals for segmentation purposes, movies were filtered in time with a 100 Hz high-pass filter. Movies were then segmented semi-automatically using principal components analysis followed by time-domain independent components analysis

(PCA/ICA)[130]. The spatial masks from PCA/ICA were then applied to the original movies without high-pass filtering to extract fluorescence traces.

3.4.7.3 Removing scattering background for lateral inhibition measurements

Background fluorescence from the region surrounding the central imaged cells (due to the scattered light) was subtracted from the baseline fluorescence of the cell.

3.4.7.4 Spike finding and scaling of fluorescence recordings

A simple threshold-and-maximum procedure was applied for spike detection. Fluorescence traces were first high-pass filtered, and initial threshold was set at 3 times the noise level. This threshold was then manually adjusted if needed.

All fluorescence signals were normalized to spike height for spike triggered average or stimulation triggered average.

3.4.7.5 Spike removal for calculation of subthreshold waveforms

Spikes were digitally removed and replaced with interpolations of the surrounding data. Spike width was estimated by viewing individual fluorescence recordings. Linear interpolations were performed between data-points 1 ms beyond the edges of the spike.

3.4.8 Statistics

All error ranges represent standard error of the mean, unless otherwise specified. For the same neurons before and after drug administration, and in anesthetized and awake states, paired sample t-test was used. For two-sample comparisons of a single variable, student's t-test was used. Probabilities of the null hypothesis $p < 0.05$ were judged to be statistically significant.

3.4.9 Biophysical modeling of membrane potential

The evolution of membrane potential in the presence of synaptic inputs and optogenetic stimulation (Fig. 3.2) was simulated with a passive single compartment model using the following equation:

$$C_m \frac{dV}{dt} = g_e(E_e - V) + g_i(E_i - V) + g_l(E_l - V) + g_{ChR}(E_{ChR} - V), \quad (3.1)$$

where C_m is the membrane capacitance, g_e, g_i, g_l and g_{ChR} are the conductance of excitatory, inhibitory, leak and channelrhodopsin channels, and E_e, E_i, E_l and E_{ChR} are the respective reversal potentials. The time course of conductance upon

excitatory or inhibitory synaptic input was simulated using an alpha function:

$$g(t) = \begin{cases} g_{syn} \frac{t-t_0}{\tau} e^{1-\frac{t-t_0}{\tau}} + g_{baseline} & \text{for } t \geq t_0 \\ g_{baseline} & \text{for } t < t_0 \end{cases} . \quad (3.2)$$

Here g_{syn} is the strength of the synaptic input, t_0 is the time of the synaptic input, t is a time-constant of synaptic input, and $g_{baseline}$ reflects the tonic level of synaptic input excluding the event of interest.

In principle, the values of $g_{baseline}$ for the inhibitory and excitatory synaptic inputs could be wrapped into the definitions of g_l and E_l. Doing so would not affect the solutions to Eq. 3.1. We chose to keep the baseline synaptic conductances as separate parameters to facilitate explorations of the model under different brain states (e.g. anesthesia vs. wakefulness). In this approach, g_l and E_l reflect cell-autonomous leak conductances (e.g. K_{ir} channels), assumed to be independent of brain state, while $g_{baseline}$ captures the effect of network-dependent inputs.

To simulate lateral inhibition in L1, we assumed inhibition lagged excitation by 2 ms. Other parameters are listed below:

Equation 1 was numerically integrated using Euler's method.

The model above can be solved analytically for the steady-state voltage by

Parameter	Value
$g_{e\ syn}$	1.5 nS
$g_{e\ baseline}$	0.1 nS
$g_{i\ syn}$	5 nS
$g_{i\ baseline}$	0.1 nS
g_l	3.33 nS
g_{ChR}	0 – 10 nS
E_e	-5 mV
E_i	-70 mV
E_l	-70 mV
E_{ChR}	0 mV
C_m	150 pF
τ	1 ms

setting $\frac{dV}{dt} = 0$, which yields:

$$V = \frac{E_e g_e + E_i g_i + E_l g_l + E_{ChR} g_{ChR}}{g_e + g_i + g_l + g_{ChR}}. \tag{3.3}$$

The PSP amplitudes are obtained by calculating the difference in steady-state voltage, ΔV_{PSP}, after vs. before the sensory perturbations to g_e and g_i, assuming that all other parameters do not vary during the synaptic event. If one assumes that g_e and g_i are both zero before the synaptic event (i.e. by absorbing the pre-stimulus values of g_e and g_i into the definition of g_l and E_l), then one finds:

$$\Delta V_{IPSP} \approx \frac{g_{ChR}[g_e(E_e - E_{ChR}) + g_i(E_i - E_{ChR})] + g_l g_e(E_e - E_l) + g_l g_i(E_i - E_l)}{(g_l + g_{ChR})(g_i + g_l + g_{ChR})}. \tag{3.4}$$

Since only differences in voltage appear in Eq. 3.4, one can arbitrarily choose

to set one of the voltages to zero, and measure all other voltages relative to this reference. For convenience, we set E_l to zero for the fitting. Eq. 3.4 is linear in g_{ChR} in the numerator, and quadratic in g_{ChR} in the denominator, suggesting 5 fitting parameters to specify the function $\Delta V_{IPSP}(g_{ChR})$. However, the proportionality between ΔV and ΔF is not a priori known. Also the proportionality between g_{ChR} and I_{488} is not a priori known. Thus the shape of the function $\Delta F_{PSP}(I_{488})$ is governed by four fitting parameters.

To estimate the waveforms of the post-synaptic potentials, we first normalized all fluorescence traces by spike height. We then calculated the mean fluorescence over 10 ms before the whisker stimulus, and the mean fluorescence over 10 ms starting 30 ms after the whisker stimulus. The difference between these values was taken as the amplitude of the post-synaptic potential. Equation 4 was fitted to the data using the nonlinear least-squares method in Matlab.

3.4.9.1 Analytical approximation

To gain an intuition for the responses, one can make a simple estimate of the amplitude of the IPSP by assuming that g_e = 0 at all times, that g_i = 0 before the synaptic input, and that the resting potential is the same as the inhibitory reversal potential, i.e. $E_l \approx E_i$. One then obtains:

$$\Delta V_{IPSP} \approx \frac{g_i g_{ChR}(E_l - E_{ChR})}{(g_l + g_{ChR})(g_i + g_l + g_{ChR})}. \tag{3.5}$$

Within the blue light intensity range used in our experiments, the CheRiff conductance is well approximated by a linear function of the blue intensity, though the proportionality factor depends on the (unknown) CheRiff expression level and attenuation of the blue light by scattering.

Eq. 3.5 shows that for small g_{ChR} the amplitude ΔV_{IPSP} is linear in g_{ChR}, while for large g_{ChR} the quadratic term in the denominator dominates and ΔV_{IPSP} decreases inversely with g_{ChR}. The value of g_{ChR} that gives the largest amplitude IPSP is $g_{ChR}^{max} = \sqrt{g_l(g_l + g_i)}$, or for weak inhibition, $g_{ChR}^{max} \approx g_l$. If g_l is large, then the shunting from g_{ChR} is suppressed. The membrane time constant is approximately $\tau \approx \frac{C}{g_l + g_{ChR}}$. The inverse relation between τ and g_{ChR} is consistent with our observation of faster recovery at stronger stimulus strength.

3.4.10 Numerical model of L1 dynamics

3.4.10.1 Single-cell properties

We simulated dynamics of L1 interneurons using Izhikevich-type models[119]. We judged more detailed channel-based biophysical models to have too many unknown parameters and to be too computationally expensive for facile exploration of multiple conditions. Simpler spike rate-based models did not capture the details of the spike timing which we judged important for L1 circuit function.

We simulated the following dynamics for eNGC cells:

$$C\frac{dV}{dt} = k(V-V_r)(V-V_t)-u+I+G_{ds}(V_D-V)+g_{Exc}(V_{Exc}-V)+g_{Inh}(V_{Inh}-V) \tag{3.6}$$

$$\frac{dV_D}{dt} = G_{SD}(V - V_D)$$

$$\frac{du}{dt} = a(b(V - V_r) - u)$$

If $V > V_p$ then $V \leftarrow c, u \leftarrow u + d$

The dynamics of SBC-like cells followed the same equations, but without the dendritic compartment ($G_{SD} = G_{DS} = 0, V_D = 0$). The meanings and values of the parameters for the two cell types are given in Table 3.1. The a, b, c, and d parameters were randomized by 10% between cells to prevent numerical degeneracies.

The differential equations were integrated using the Euler method with a step size of 0.1 ms. Some ancillary results are useful in tuning the properties of this model. These are:

- In the absence of synaptic inputs ($g_{Exc} = g_{Inh} = 0$) or injected current (I = 0), the resting-state membrane resistance is:

$$\frac{dV}{dI}|_{I=0} = (b + k(V_t - V_r)).$$

- To change the membrane resistance while maintaining dynamical properties, one should scale b and k proportionally.

- To change the membrane capacitance while maintaining dynamical properties, one should scale C, b, d, and k proportionally.

3.4.10.2 Channelrhodopsin activation

The channelrhodopsin CheRiff was modeled as an excitatory conductance with reversal potential 0 mV and conductance proportional to blue light illumination intensity. Channel gating kinetics were assumed to be instantaneous. Patterns of blue light were targeted to one or more cells and modulated in time during the simulation.

3.4.10.3 Synaptic properties: Inhibition

Examination of patch clamp recordings of inhibitory post-synaptic potentials (IPSPs) in acute slices showed a rapid onset followed by a slow recovery. The recovery was not well captured by a single exponential. To approximate these dynamics we used the following function:

$$g_{inh}(t) = g^0_{inh}(\frac{t}{\tau_1}e^{1-\frac{t}{\tau_1}} + 0.6\frac{t}{\tau_2}e^{1-\frac{t}{\tau_2}})$$

τ_1 = 7 ms, τ_2= 35 ms. We found that the qualitative network dynamics were insensitive to variations in the functional form or time constants. One may think of

the two terms as representing $GABA_A$ and $GABA_B$ receptors respectively, though a more accurate implementation of a $GABA_B$-mediated hyperpolarization would use the K^+ reversal potential (-90 mV) rather than the Cl^- reversal potential (-70 mV).

To calibrate the value of g^0_{inh} for $eNGC \rightarrow eNGC$ and $eNGC \rightarrow SBC$ synapses, we set up a model circuit with one eNGC cell synapsing onto an eNGC cell and an SBC cell. In the simulations, we adjusted a channelrhodopsin conductance (V_{ChR} = 0 mV) to depolarize the downstream cells to -55 mV. We then triggered the upstream cell to spike. We adjusted g^0_{inh} to induce IPSP amplitudes of -1.5 to -2 mV, to match the patch clamp data. The model did not contain short term inhibitory synaptic plasticity.

The IPSP amplitudes recorded via patch clamp were assumed to represent the strongest possible IPSPs. The IPSP strength between each pair of neurons in the circuit was modulated by a Gaussian function of separation, with a length-scale set by the sum of sizes of the presynaptic axonal arbor and the postsynaptic dendritic arbor.

3.4.10.4 Synaptic properties: Excitation

We modeled thalmocortical excitation in L1 using the function:

$$g_{exc}(t) = g^0_{exc}\frac{t}{\tau}e^{1-\frac{t}{\tau}}$$

We calibrated the amplitude of g^0_{exc} and τ by simulating thalamic inputs to eNGC cells and SBC-like cells and matching to literature data which showed that whisker-evoked EPSP amplitudes in vivo were 3 – 7 mV. We assumed that the timecourse of thalamic excitation to all neurons was identical. Excitatory synaptic strengths were randomized by 20% between cells to prevent numerical degeneracies. The model did not contain short term excitatory synaptic plasticity.

3.4.10.5 Synaptic properties: Neuromodulation

The greatest uncertainty in the model surrounded the timecourse and strength of neuromodulatory inputs. We assumed that neuromodulatory inputs activated an excitatory conductance with reversal potential 0 mV. We assumed that the strength and timecourse of neuromodulatory action was the same on the eNGC and SBC-like neurons. If the coupling of neuromodulatory input to the SBC-like neurons was sufficiently strong, then these neurons could be activated by neuromodulatory inputs, even in the absence of thalamic inputs. We do not know whether this situation occurs in vivo.

3.4.10.6 Omissions from the model

Many possibly relevant features were omitted from the model. These include: gap junction connections between eNGC neurons[105], activation of $GABA_B$ receptors, activation of muscarinic acetylcholine receptors[131], and possible feedback inhibition

from deeper layer Martinotti cells[102]. We did not consider a finer classification of L1 interneurons into sub-types. Our model also did not include cortico-cortical inputs. We did not study or simulate the effects of L1 interneuron activation on apical dendrites of deeper layer pyramidal cells. Activation of $5HT_3A$ ionotropic serotonin receptors is expected to have similar electrophysiological effects to activation of nicotinic acetylcholine receptors, though the distribution of these two receptor-types in the different L1 interneuron sub-classes may be different.

3.5 Supplemental Figures

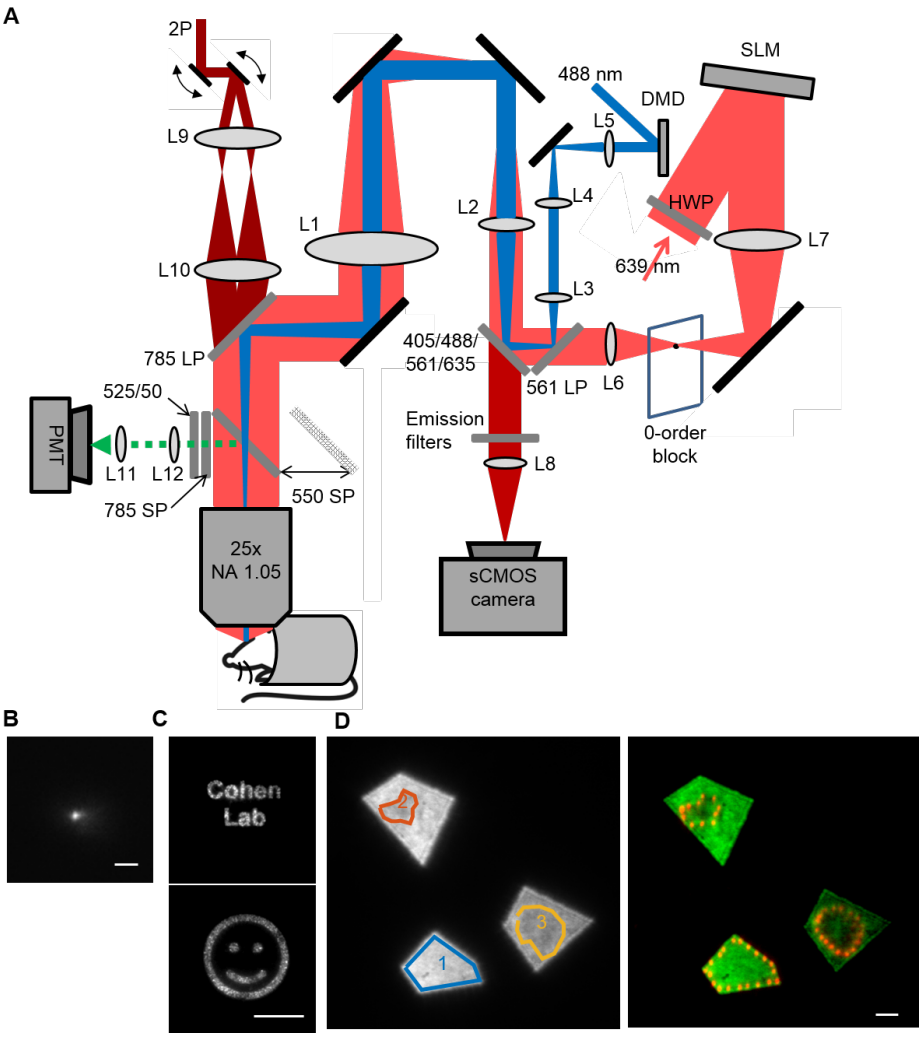

Figure 3.6: Instrument for all-optical electrophysiology in vivo. (**A**) Layout of the optical setup. The spatial light modulator (SLM) diffractively patterned the red laser (λ= 639 nm) into a set of discrete foci on the sample for holographic structured illumination excitation of a far red GEVI. The digital micromirror device (DMD) acted as a binary amplitude mask and projected a pattern of blue light onto the sample for targeted optogenetic activation of a blue-excited channelrhodopsin. Fluorescence from the sample was imaged onto a scientific CMOS camera. For two-photon (2P) imaging, pulsed infrared light (λ = 920 nm) was scanned by a pair of galvo mirrors. A dichroic mirror was inserted into the beam path to direct green fluorescence onto a photomultiplier (PMT). Parts list in Table 3.3. Not shown: beam expansion and polarization control optics for each of the laser beams. (**B**) Point-spread function of the red illumination. Scale bar 10 μm. (**C**) Diffractively patterned red light illumination patterns projected onto a homogeneous fluorescent test sample. Scale bar 50 μm. (**D**) Combination of patterned blue and red illumination. Left: Patterns of fluorescence excited by blue light projected onto a homogeneous fluorescent test sample. Target patterns for the red illumination were manually defined. Right: Superposition of image of the red illumination on the green fluorescence excited by blue illumination. Scale bar 10 μm.

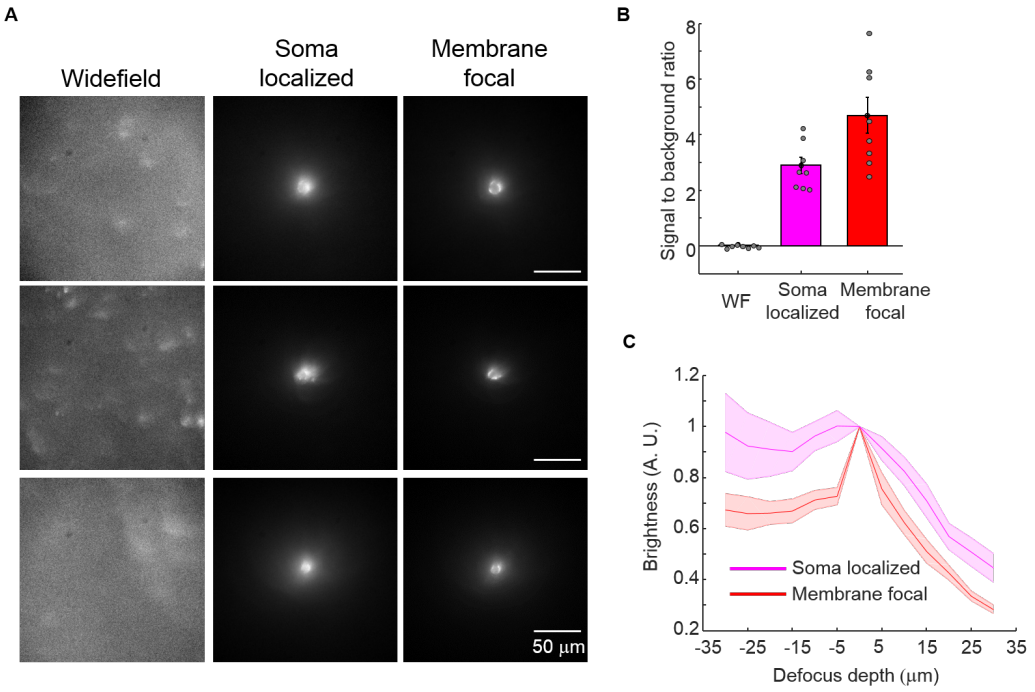

Figure 3.7: Holographic structured illumination microscopy improves signal-to-background ratio in vivo. (**A**) Representative images in the SomArchon fluorescence channel showing wide-field, cell-localized, and holographic focal illumination. (**B**) Quantification of the signal (cell area) to background (surrounding region) ratio for the three illumination schemes. (**C**) Quantification of the relative signal level as a function of defocus. Here a signal mask was defined on the in-focus image, and then applied to images taken at a series of defocus values.

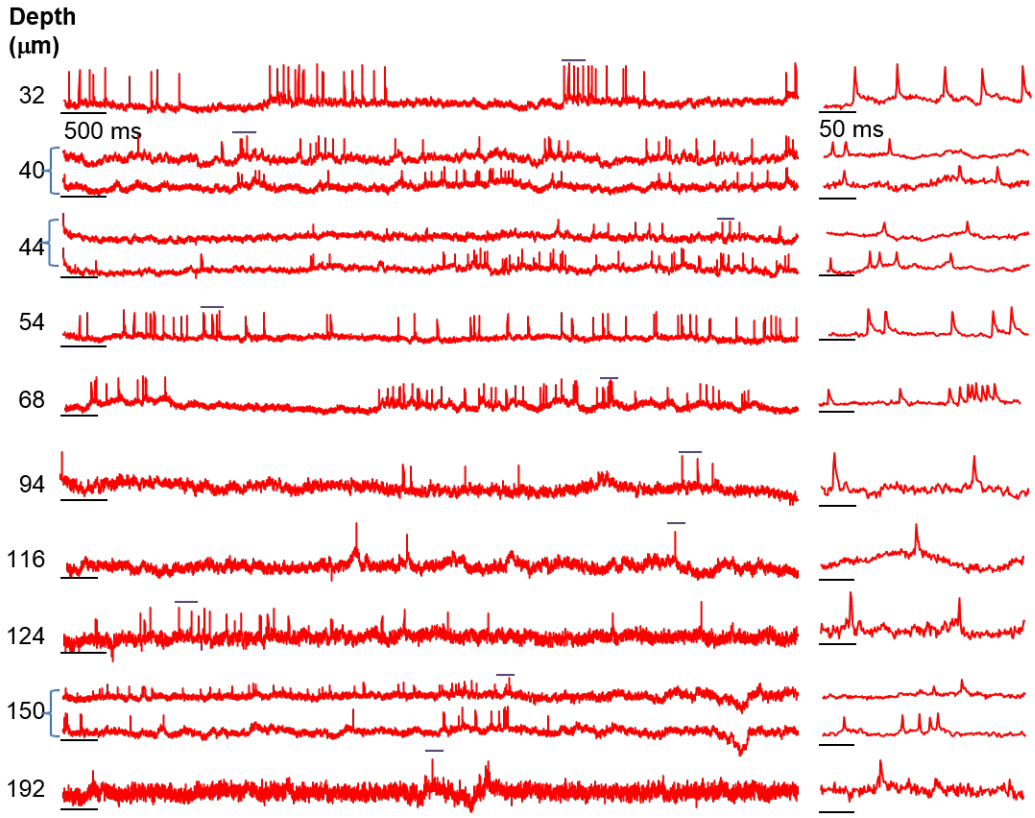

Figure 3.8: Voltage imaging in the cortical neurons at different depths in awake mice. Fluorescence recordings of neurons expressing SomArchon-eGFP in barrel cortex of awake mice. Neurons were located via 2P microscopy and then targeted with holographic 1P red illumination (3 mW/cell). Fluorescence was recorded at 1 kHz. Left: single-trial recordings of spontaneous activity. Pairs of simultaneously recorded cells shown with brackets. Right: magnified views of the regions indicated by the purple over-bars from the left. SNR values (spike height:baseline noise) were 20 at the shallowest depth and 6.7 at the greatest depth.

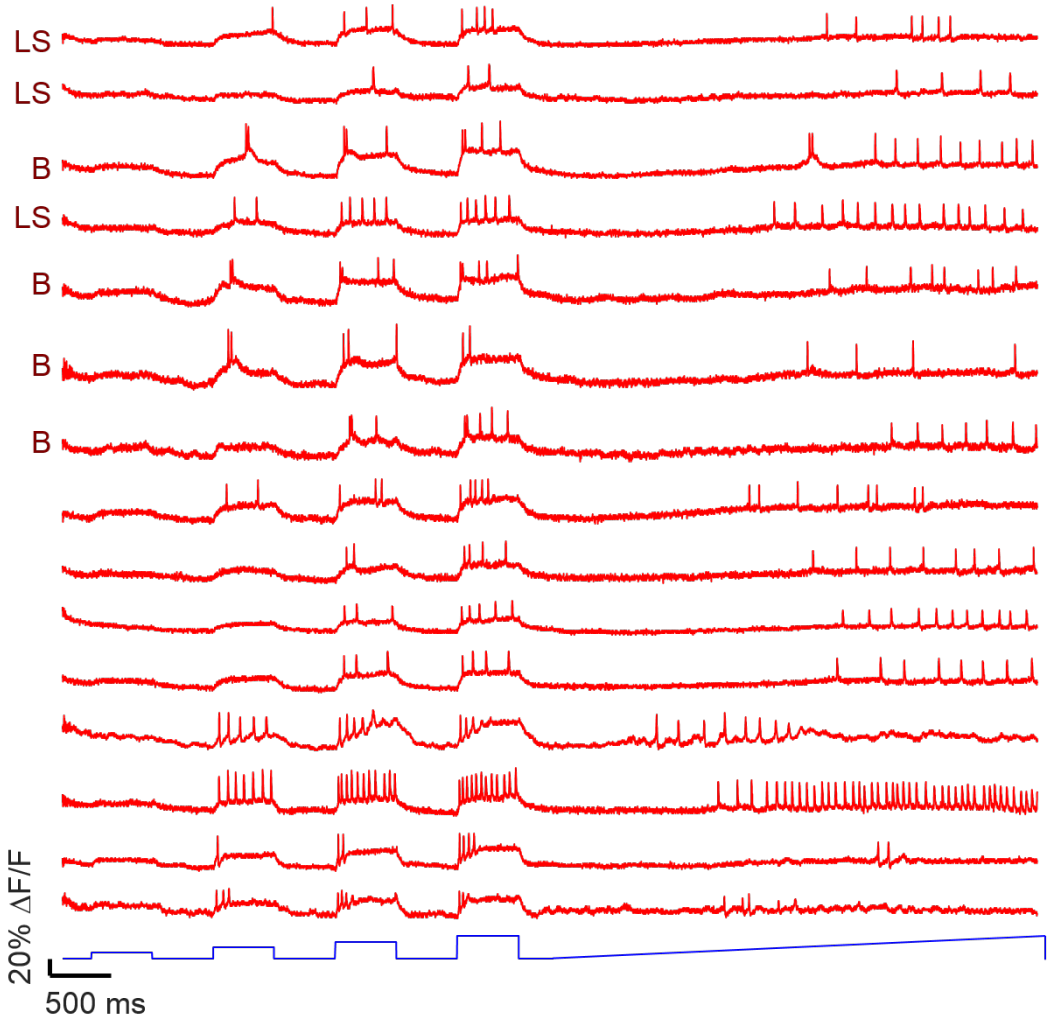

Figure 3.9: Optopatch excitability measurement of cortical L1 neurons in acute slices. In cortical L1 neurons from a 5-HT_{3A}R-Cre mouse expressing Optopatch4, the SomArchon fluorescence reported action potentials with high SNR. Red: fluorescence of SomArchon during optogenetic stimulation, recorded at 1 kHz. Blue: Optogenetic stimulus waveform (500 ms duration, 0.2 to 2.1 mW/mm^2, repeated at 1 Hz). The signal-to-noise ratio (spike:baseline noise) was 21 $\pm$ 1 in a 1 kHz bandwidth (n = 15 cells, 1 mW per cell, mean $\pm$ s.e.m.). Some of the spiking waveforms have been labeled as "Late spiking" (LS) or "Bursting" (B) in correspondence with established L1 firing phenotypes. Not all cells clearly fell into one of these classes.

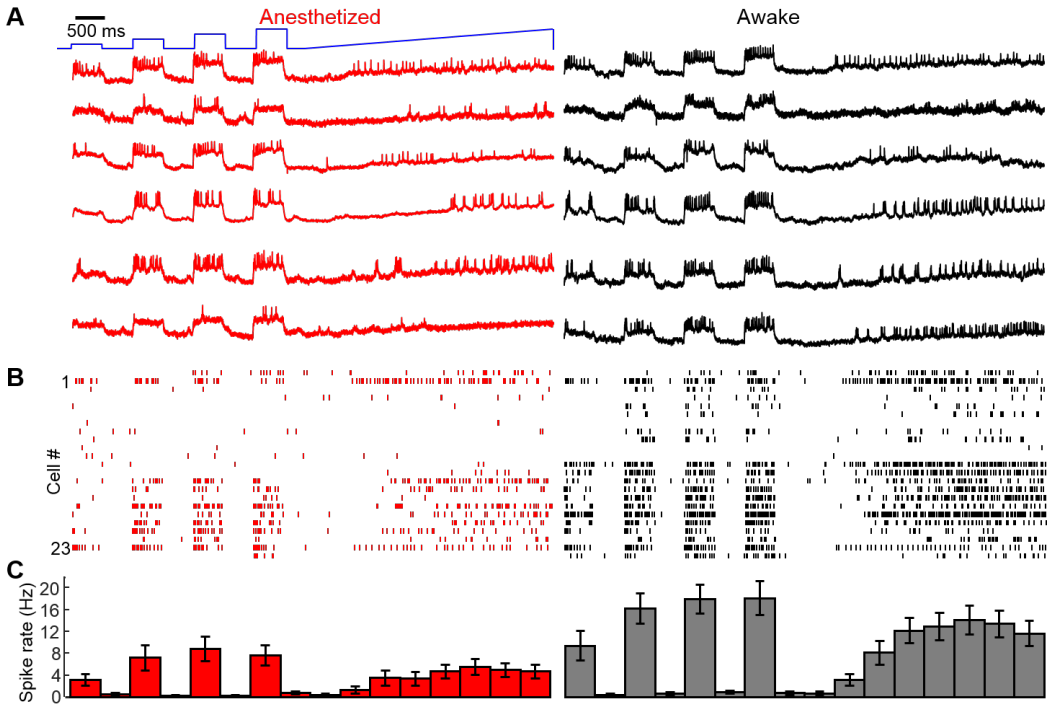

Figure 3.10: Paired recordings of L1 excitability under anesthesia and wakefulness. (**A**) Individual L1 neurons were illuminated with steps of blue light (500 ms duration, 1.8 to 21 mW/mm^2, repeated at 1 Hz), followed by a ramp of blue light. Voltage was recorded at 1 kHz via holographic focused excitation of SomArchon fluorescence. Neuron coordinates were recorded relative to blood vessel landmarks. Anesthesia was then ended. After the animal awoke the measurements were repeated on the same set of cells. Each row represents repeated recordings of the same cell (n = 23 neurons from 3 mice). (**B**) Spike raster for the complete dataset recorded under anesthesia and wakefulness. (**C**) Mean spike rate during each stimulation epoch. Error bars represent s.e.m..

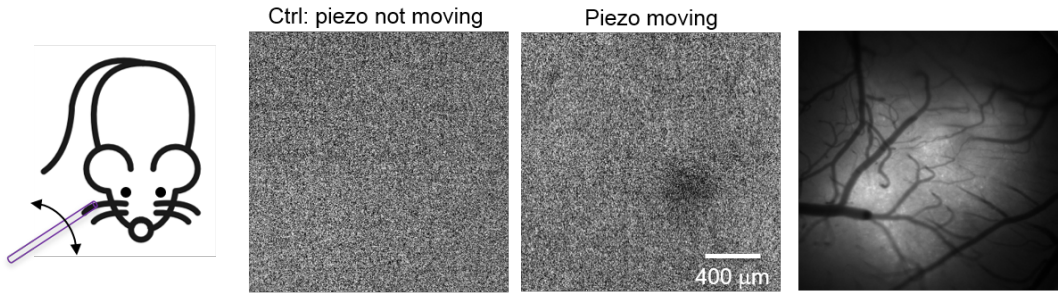

Figure 3.11: Intrinsic imaging to locate barrels corresponding to a single whisker. In an anesthetized mouse, the surface of the brain was imaged via 640 nm reflected light. A single whisker was periodically stimulated (10 Hz, 4 s, followed by 16 s rest) for 5 min. Images were acquired at 10 Hz. The mean of the image acquired during the stimulated epochs was subtracted from the mean of the image acquired during the rest epochs. A dark spot highlighted the active barrel. A reference image taken with back-scattered blue light identified the blood vessel landmarks around the active barrel.

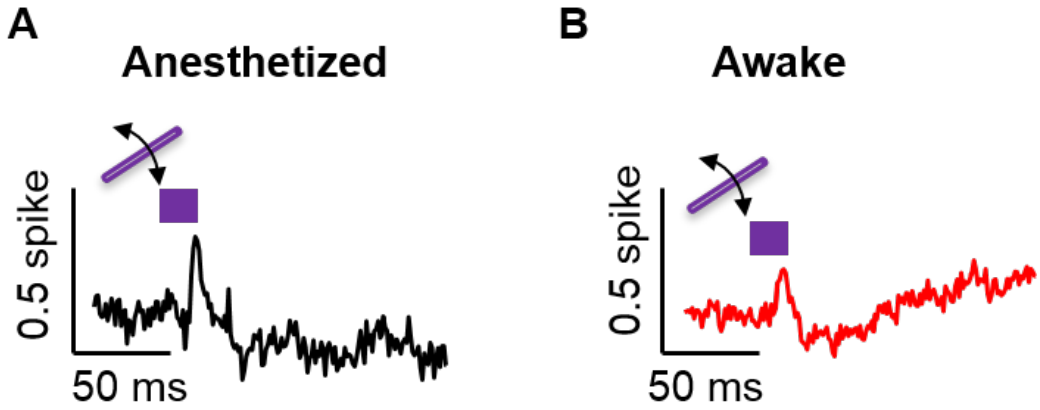

Figure 3.12: Whisker stimuli that failed to evoke spikes still evoked post-stimulus hyperpolarization. Stimulus-triggered average waveforms were computed for stimulus events that failed to evoke a spike in the measured neuron. In both (**A**) anesthetized and (**B**) awake animals, the stimulus evoked an EPSP followed by an IPSP. Post-stimulus hyperpolarization in the absence of a spike indicates that the hyperpolarization arose from network inputs rather than from cell-autonomous mechanisms. Data from n = 9 neurons (anesthetized) and n = 16 neurons (awake), 3 mice in both cases.

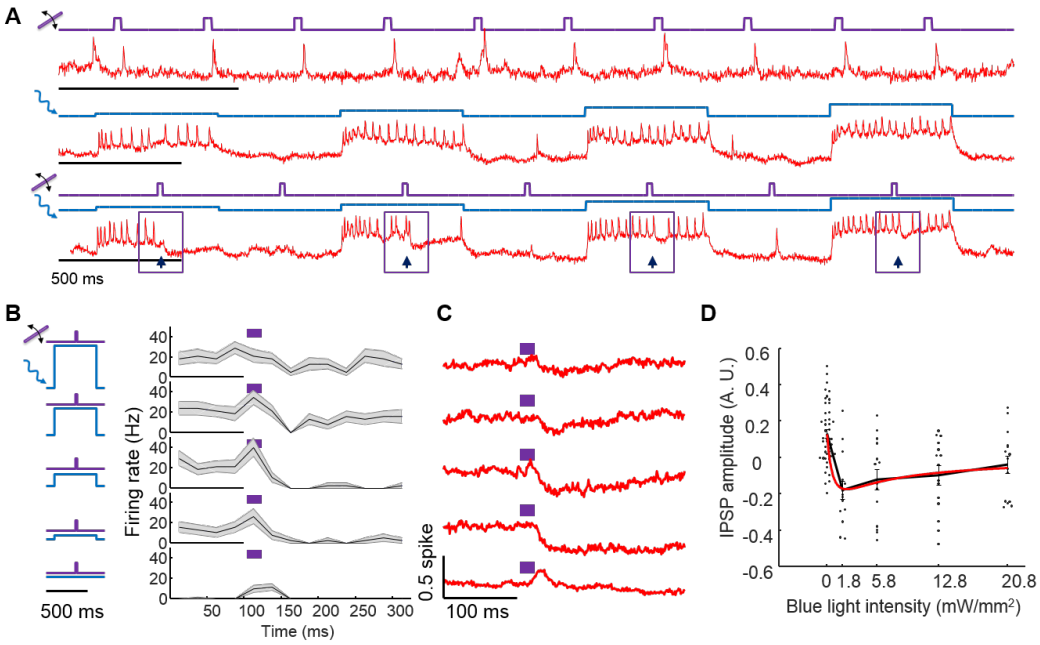

Figure 3.13: Optical dissection of E/I balance in L1 interneurons in anesthetized mice. (**A**) Three recordings from a single neuron showing response to (top) whisker stimulus, (middle) optogenetic stimulus, and (bottom) simultaneous optogenetic and whisker stimuli. Arrows show whisker stimulus-evoked inhibition. (**B**) Mean spike rate evoked by whisker stimuli atop different levels of optogenetic stimulus. In the absence of optogenetic stimulation, whisker stimuli evoked single spikes. In the presence of optogenetic stimulation, whisker stimuli suppressed spiking. The suppression decreased in amplitude and duration as the strength of the optogenetic stimulus increased. Shading represents s.e.m. from n = 15 neurons, 3 mice. (**C**) Mean whisker stimulus-evoked subthreshold waveforms at different levels of optogenetic drive. Spikes were digitally removed prior to averaging (Methods). (**D**) Comparison of IPSP amplitude as a function of optogenetic stimulus strength with numerical simulation from a simple conductance-based model.

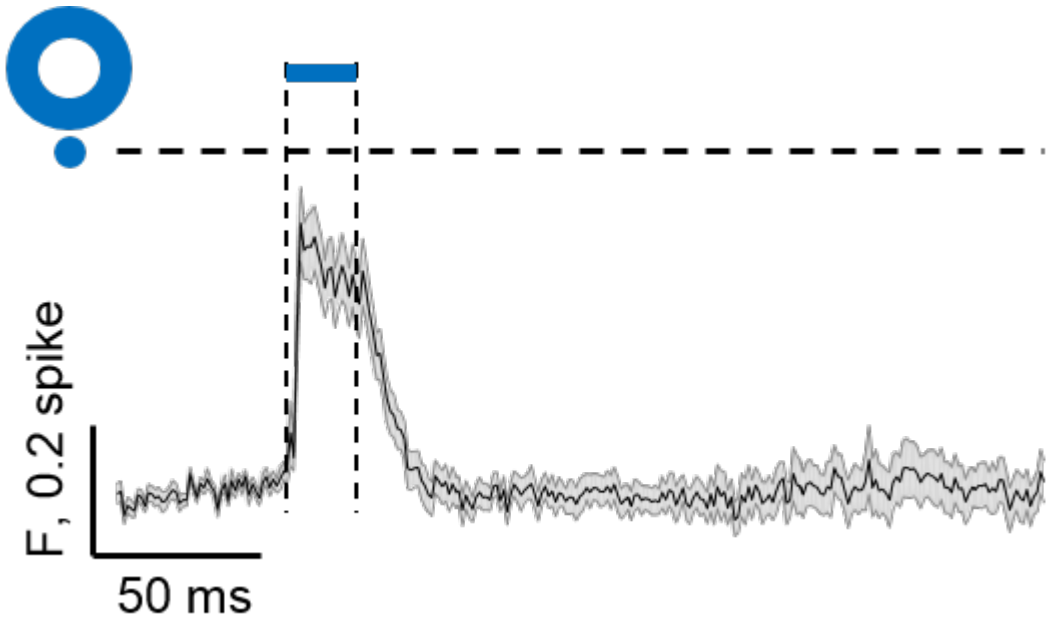

Figure 3.14: Light scatter contributes a depolarizing transient when a neuron is surrounded by a ring stimulus. Mean fluorescence response of a central neuron during a 20 ms annular stimulus to surrounding neurons (25 mW/mm^2). This experiment is the same as in Fig. 3.3G, except that the central neuron is not subject to optogenetic stimulation. The experiment shown here and in Fig. 3.3G were performed on the same set of neurons in interleaved trials +/- central optogenetic depolarization (n = 25 neurons, 3 mice). The time-course of subthreshold depolarization matches the expectation from direct stimulation of the central neuron via scattered blue light from the surrounding annulus.

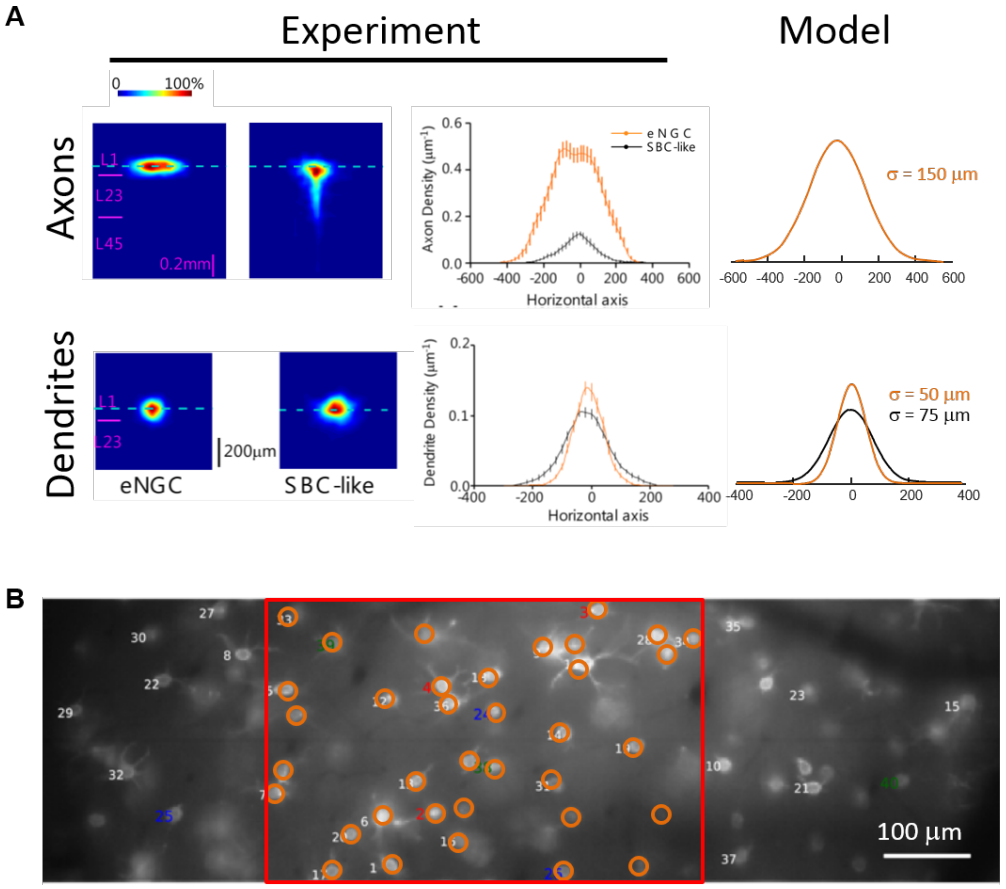

Figure 3.15: Calibration of morphological properties of L1 microcircuit. (**A**) Length-scale of connectivity. Data from[121]. Synaptic weights were set by gaussian distributions fit to the experimental data. The length-scale of each synaptic connection was set to the sum of the widths of the axonal and dendritic arbors. (**B**) Density of neurons in L1. Cell density was estimated from published images of fluorescently labeled L1 interneurons. Data from[108]. These results were consistent with precise counts taken in the rat[132].

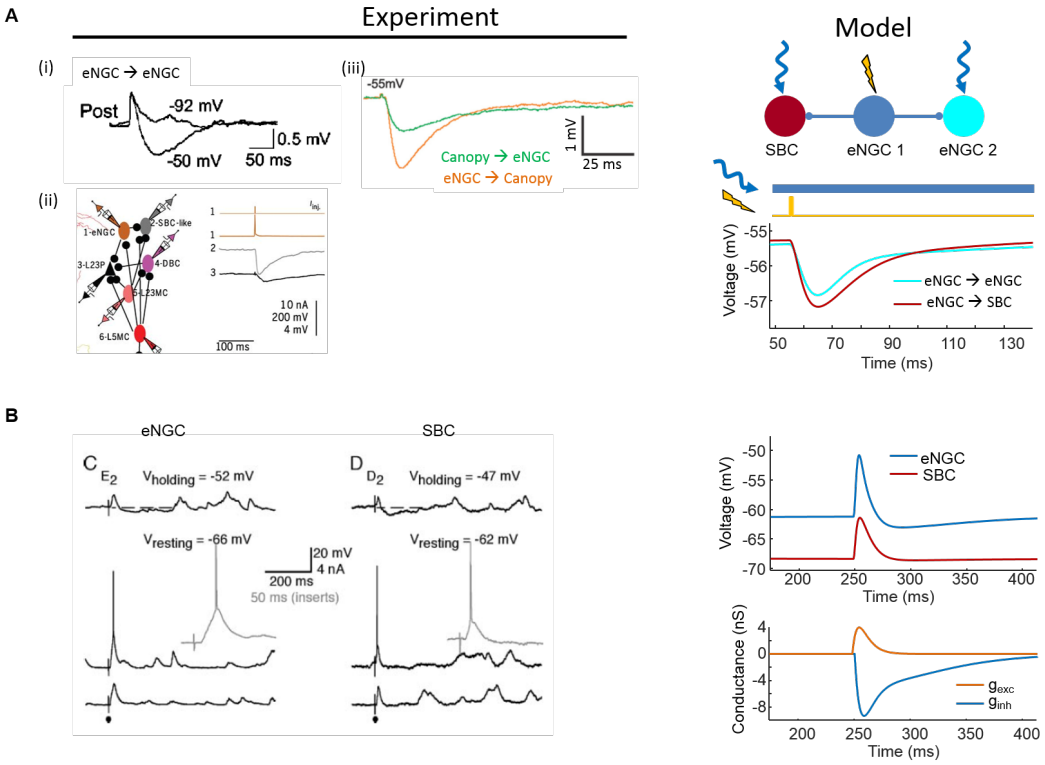

Figure 3.16: Calibration of synaptic properties of L1 model. (**A**) Calibration of inhibitory synaptic strengths. Data from (i)[105] (ii)[121] (iii)[106]. (**B**) Model for synaptic inhibition. An eNGC cell was stimulated to spike once. The timecourse and amplitude of the postsynaptic inhibitory conductances were adjusted to match approximately the experimental IPSPs. In the simulation, the postsynaptic cells were optogenetically depolarized to -55 mV to introduce a driving force for Cl^- entry. B) Calibration of excitatory thalamocortical synaptic strengths. Patch clamp recordings showed that whisker stimuli evoked EPSPs of 3 – 7 mV. In the model, excitatory synaptic strength was adjusted so that, in combination with sensory-induced lateral inhibition, the EPSP from baseline approximately matched the timecourse and amplitude observed experimentally.

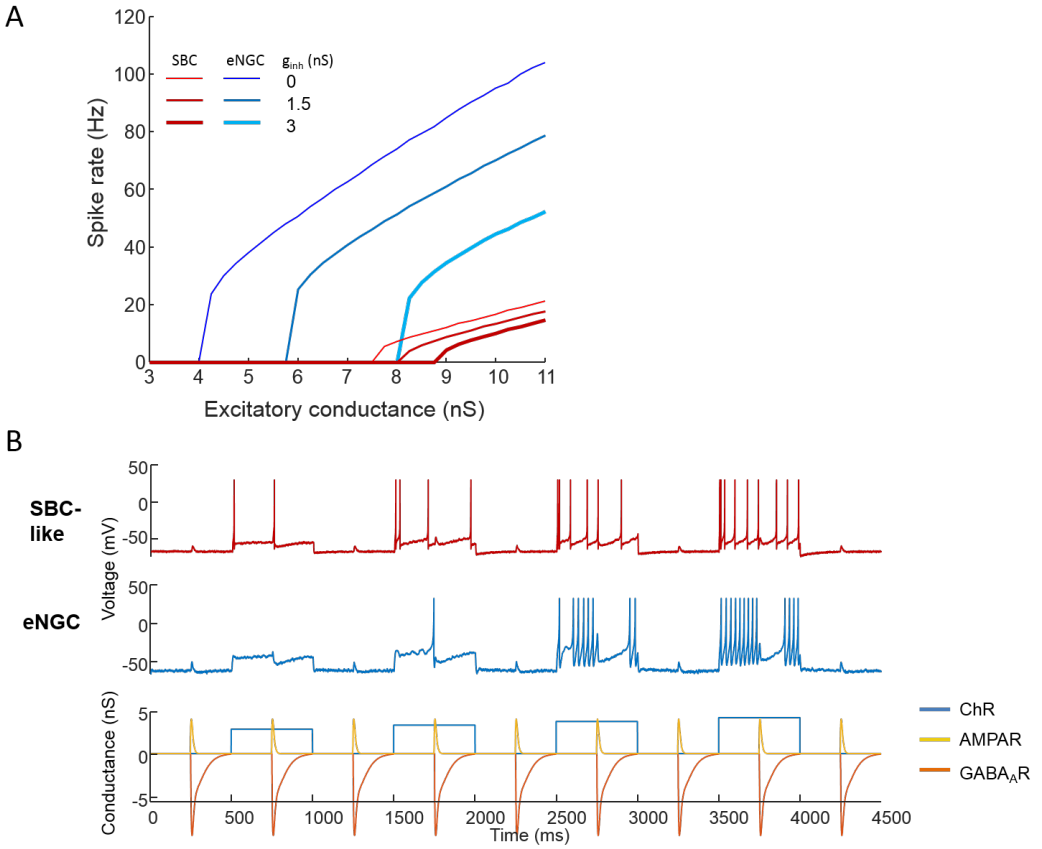

Figure 3.17: Characterization of single-cell firing properties in L1 model. (**A**) Steady-state spiking rate as a function of excitatory and inhibitory conductance. eNGC cells showed a clear threshold to activate spiking, while SBC cells showed a more graded response. The difference in activation threshold implied that the SBC output cells were never activated without simultaneous activation of the eNGC cells, i.e. that excitation of the output always occurred in the presence of lateral inhibition. VIP^+ interneurons (associated with the SBC-like population) have been shown experimentally to have a more hyperpolarized resting potential and a more depolarized threshold potential than other L1 interneuron classes[106]. (**B**) Numerical simulations in which single cells were exposed to step-wise increases in channelrhodopsin activation and paired excitatory and inhibitory inputs. In the absence of optogenetic stimulation, the synaptic inputs drove small depolarization. In the presence of optogenetic stimulation, the synaptic inputs drove primarily inhibition. The magnitude and duration of the inhibition decreased as the strength of the optogenetic stimulation increased.

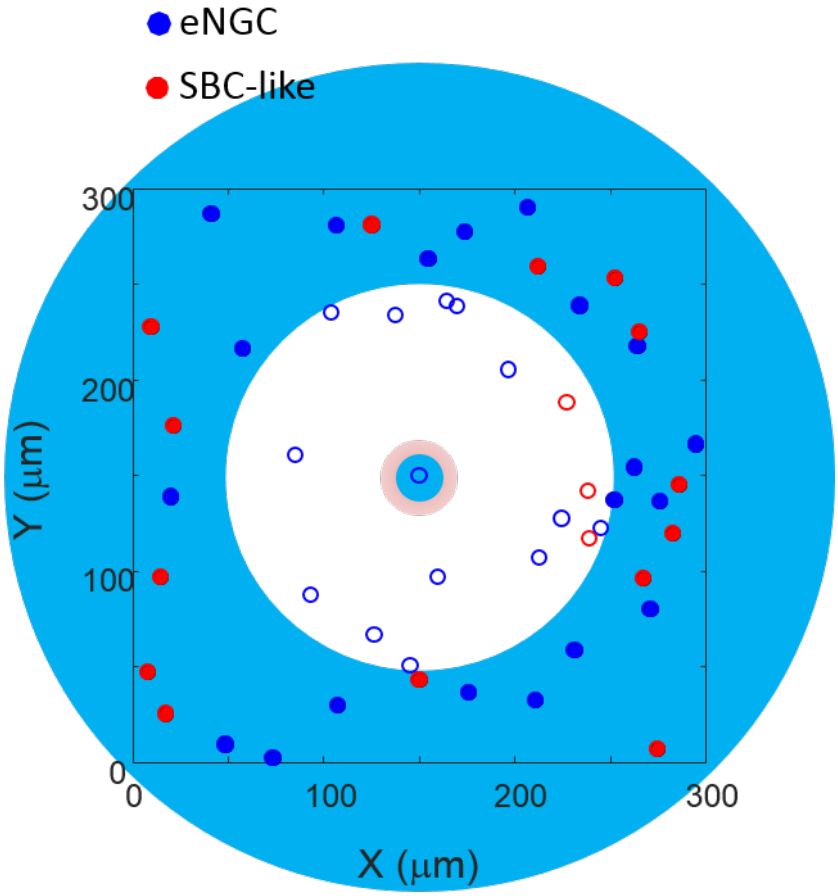

Figure 3.18: Geometry of annular optogenetic stimulation in a simulated L1 barrel. Cells were randomly positioned in a region 300 μm on an edge, 150 μm deep. A single cell (eNGC or SBC-like) was manually defined to reside at the center of the region. The central neuron was subjected to tonic optogenetic depolarization. Neurons at radii r $>$ 100 μm from the center were subjected to pulsed optogenetic stimulation. The voltage in the central neuron was plotted in Fig. 3.5D.

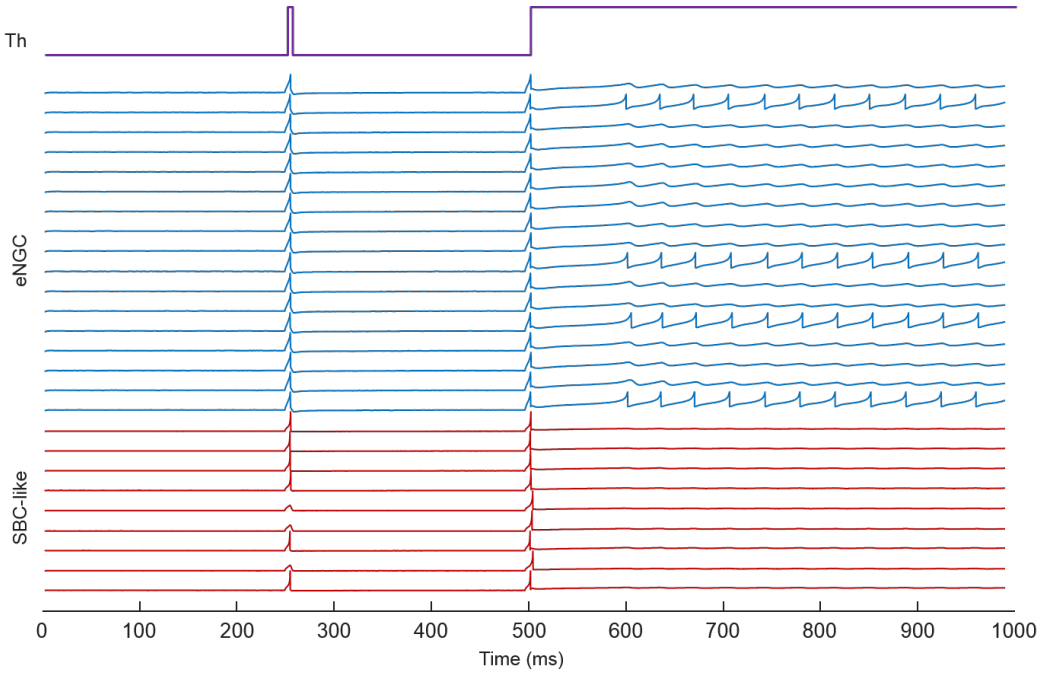

Figure 3.19: Comparison of L1 network responses to abrupt vs. sustained inputs. A thalamic input was delivered simultaneously to all eNGC and SBC-like neurons in an L1 simulation. Transient inputs activated all eNGC neurons and most SBC-like neurons. Sustained inputs of the same strength initially activated most neurons. After a period of global network inhibition, a subset of eNGC neurons became tonically active, suppressing activation of the other eNGC neurons and of the SBC-like population. Here a randomly selected subset of the neurons are plotted.

Parameter	eNGC neuron	SBC-like neuron	Meaning and comments
C	30 pF	30 pF	Membrane capacitance. Artificially low compared to patch clamp recordings, necessary for fast spikes.
k	0.3 pA/mV	1.2 pA/mV	Conductance of endogenous voltage-gated channels (pA/mV = nS)
V_r	-66 mV	-70 mV	Resting potential
V_t	-36 mV	-39 mV	Threshold potential
V_p	30 mV	30 mV	Spike peak potential
a	0.17 ms^{-1}	0.01 ms_{-1}	Recovery rate constant
b	5 pA/mV	6 pA/mV	Recovery conductance
c	-45 mV	-65 mV	Post-spike reset value for membrane voltage
d	100 pA	90 pA	Post-spike jump in adaptation variable, u.
G_{ds}	1.2 pA/mV	-	Dendrite-to-soma coupling strength
G_{sd}	0.01 pA/mV	-	Soma-to-dendrite coupling strength
V_{ChR}, V_{AMPA}, V_{nAchR}	0 mV	0 mV	Reversal potential of excitatory conductances
V_{Cl}	-70 mV	-70 mV	Reversal potential of inhibitory ($GABA_A$R-mediated) conductances

Table 3.1: Parameters of Izhikevich-type models of L1 interneurons. The eNGC cells were described by a two-compartment cell, with one active compartment and a passive dendrite. The SBC-like cells were described by a one-component model. Parameters were adjusted by hand to match the observed firing patterns.

Parameter	Source Data	Model
eNGC firing pattern	Chu et al. J. Neurosci. 23 (2003): 96-102. Fig. 1	Modified from Izhikevich, Dynamical Systems in Neuroscience, Eq. 8.28
SBC firing pattern	Chu et al. J. Neurosci. 23 (2003): 96-102. Fig. 1	Modified from https://www.izhikevich.org/publications/figure1.m Fig. 1E,F
IPSP waveform: eNGC $\rightarrow$ eNGC	Chu et al. J. Neurosci. 23 (2003): 96-102. Fig. 5	$g_{inh}(t) = g^0_{inh}(\frac{t}{\tau_1}e^{1-\frac{t}{\tau_1}} + 0.6\frac{t}{\tau_2}e^{1-\frac{t}{\tau_2}})$ g^0_{inh}=1nS, t_1= 7 ms, t_2 = 35 ms
IPSP amplitude eNGC $\rightarrow$ eNGC	Jiang et al. Science 350 (2015): aac9462. Table S6	-1.6 mV
IPSP waveform eNGC $\rightarrow$ SBC	Chu et al. J. Neurosci. 23 (2003): 96-102. Fig. 4 Jiang et al. Science 350 (2015): aac9462. Fig. 3a	$g_{inh}(t) = g^0_{inh}(\frac{t}{\tau_1}e^{1-\frac{t}{\tau_1}} + 0.6\frac{t}{\tau_2}e^{1-\frac{t}{\tau_2}})$ g^0_{inh}=1.6nS, t_1= 7 ms, t_2 = 35 ms
IPSP amplitude eNGC $\rightarrow$ SBC	Jiang et al. Science 350 (2015): aac9462. Table S6	-1.8 mV
Length scale of eNGC $\rightarrow$ eNGC coupling	Jiang et al. Science 350 (2015): aac9462. Figs. S2, S3	s = 200 μm (sum of axonal and dendritic length scales)
Length scale of eNGC $\rightarrow$ SBC coupling	Jiang et al. Science 350 (2015): aac9462. Figs. S2, S3	s = 225 μm (sum of eNGC axonal and SBC dendritic length scales)
L1 neuron density	Abdelfattah et al., BioRxiv: /10.1101/436840. Fig. S23 Meyer et al., PNAS 110 (2013) 19113-19118. Table S2	3000-7,000 mm^{-3}, 15 – 67 neurons/barrel (in rat)
Ratio of eNGC to SBC cells	Schuman et al. J. Neurosci. 39 (2019): 125-139. Fig. 2,4	$\sim$2:1

Thalamocortical EPSP waveform in eNGC	Zhu and Zhu, J. Neurosci. 24 (2004): 1272-1279. Fig. 2	$g_{exc}(t) = g^0_{exc}\frac{t}{\tau}e^{1-\frac{t}{\tau}}$ g^0_{exc}=4nS, t=6 ms
Thalamocortical EPSP amplitude in eNGC	Zhu and Zhu, J. Neurosci. 24 (2004): 1272-1279. Fig. 2 Lee et al., J. Neurosci. 30 (2010): 16796-16808. Fig. 7	3 - 7 mV
Thalamocortical EPSP waveform in SBC	Zhu and Zhu, J. Neurosci. 24 (2004): 1272-1279. Fig. 2	$g_{exc}(t) = g^0_{exc}\frac{t}{\tau}e^{1-\frac{t}{\tau}}$ g^0_{exc}=4nS, t=6 ms
Thalamocortical EPSP amplitude in SBC	Zhu and Zhu, J. Neurosci. 24 (2004): 1272-1279. Fig. 2 Lee et al., J. Neurosci. 30 (2010): 16796-16808. Fig. 7 (But see also Cruikshank et al. J. Neurosci. 32 (2012): 127813-17823. Fig. 4d)	3 - 7 mV
Strength of neuromodulatory input to eNGC	Unknown	Assumed to be same for eNGC and SBC
Strength of neuromodulatory input to SBC	Unknown	Assumed to be same for eNGC and SBC

Table 3.2: Parameters used in simulations of L1 network activity. Some parameters were from data in rats or from different brain regions. We verified that where there was uncertainty in parameter values, the simulation results did not qualitatively depend on precise parameter values.

Item	Part number	Comments
2P Laser	Coherent DeepSee	
Scanning galvos	Cambridge Technologies 6215H	
Scan lens	Thorlabs, SL50-CLS2	
2P tube lens	Thorlabs, TL200-CLS2	
PMT	Hamamatsu, H11706P-40	
25x objective	Olympus XLPLN25XWMP2	
L1	400 mm, Edmund, 88-598-INK	
L2	Effective focal length, 150 mm, two 300 mm lenses, Thorlabs, AC508-300-A-ML	Two lenses back to back in Plössl configuration to reduce aberration
L3	75 mm, Thorlabs, AC254-075-A-ML	Relay lens to allow more space
L4	75 mm, Thorlabs, AC254-075-A-ML	Relay lens to allow more space
L5	60 mm, Thorlabs, AC254-060-A-ML	
L6	First generation: Sigma macro 18-200 mm	First generation: Zoom lens for varying NA of red illumination and size of red targeted region;
	Second generation: 75 mm, Thorlabs, AC508-075-A-ML	Second generation: 75 mm lens to reduce aberration
L7	200 mm, Thorlabs, AC508-200-A-ML	
L8	45 mm, Olympus XLFLUOR 4X/340	Objective used as a tube lens for reducing aberration and achieving large field of view

L9	Thorlabs, SL50-CLS2	Optimized scan lens
L10	Thorlabs, TL200-CLS2	Optimized tube lens
L11	16 mm, Thorlabs, AC080-016-A-ML	
L12	75 mm singlet, Thorlabs, LA1608-A-ML	
488 nm laser	Cobolt, 06-01 series, l = 488 nm, 60 mW	
AOTF	Gooch and Housego TF525-250-6-3-GH18A	
DMD	Vialux, V-7001 VIS	
639 nm laser	CNI Inc., MRL-FN-639, l = 639 nm, 700 mW single transverse mode	
SLM	Meadowlark 1920SLM VIS	
0-order block	home-made anti-pinhole comprised of a dot of solder on a glass slide	
sCMOS camera	Hamamatsu ORCA-Flash 4.0	
Sample stage	Sutter instrument, FG-MPC78, Moving stage plat W/MPC-200 for XY stage; SA-MP285-1X-M for Z axis	
DAQ system	NI PCIe-6363	

Table 3.3: Components required to build an optical system for holographic structured illumination voltage imaging combined with patterned optogenetic stimulation.

3.6 Manuscript Information

3.6.1 Previously published as

A version of this chapter appeared in[22]:

L. Z. Fan, S. Kheifets, U. L. Bohm, K. D. Piatkevich, H. Wu, V. Parot, M. E. Xie, E. S. Boyden, A. E. Takesian, A. E. Cohen. All-optical electrophysiology reveals excitation, inhibition, and neuromodulation in cortical layer 1. bioRxiv: 614172, 2019.

This work is submitted for publication, currently under revision.

3.6.2 Acknowledgements

We thank B. Sabatini for advice and discussion; G. Vargish and T. Hensch for the $5HT_{3A}$R-Cre mouse line; S. Begum, K. Williams, A. Preecha and H. Dahche for technical assistance; M. Gomez-Ramirez, C. Moore and F. Wang for advice on whisker stimulation; H. Pi for advice on air puff; B. Gmeiner for advice on optics; Y. Adam for advice on mouse surgeries. This work was supported by the Howard Hughes Medical Institute.

3.6.3 The author's contribution

Linlin Z Fan, Anne E Takesian, and Adam E Cohen conceived and designed the study. Linlin Z Fan designed and conducted the experiments, built the optical

system, programed the software, analyzed the data and co-wrote the manuscript. Simon Kheifets and Hao Wu built the optical system in early stage. Urs L Bohm performed numerical simulations and data fitting. Kiryl D Piatkevich and Edward S Boyden shared SomArchon. Vicent Parot helped with slice experiments. Michael E Xie helped analyze the data. Adam E Cohen and Linlin Z Fan performed network simulations. Adam E Cohen co-wrote the manuscript and supervised the research.

4

Conclusion

Years of exploration in voltage imaging of E and I has made me believe the future for voltage imaging is bright. Here I conclude with three directions. First, I detail a proposal for further dissecting L1 neurons in attention and learning. Second, I propose technical advances. Finally, one could apply the technique for testing network models as listed in the introduction part.

4.1 All-optical electrophysiology of cortical layer 1 neurons in attention and learning

Our brain receives constant inputs from all of our sensory organs; yet we only attend to those inputs that are important to us, either because they are novel or salient (e.g. when a fire alarm goes off), or because we have learned that they are important (e.g. an association of the dinner bell with food). How does our brain control which inputs get selected and which get ignored? I hypothesize that a collection of sparse interneurons in cortical layer 1 (L1) may function as a switch for filtering noises and controlling attention[95,94,93,92].

As shown in Chapter 3, all-optical electrophysiology imply that cortical L1 circuits are ideally located for integration of bottom-up and top-down information in behaving mice.

Understanding the function of cortical L1 circuits will require 1, the identification of cell types in cortical L1 circuits[106]; 2, mapping connectivity upstream and downstream of L1 circuits and among different cell types in L1; 3, the context of behaviors that engage the circuits; and 4, simultaneous recording and manipulation of the circuits for causality during behavior[133]. Here I propose to use an all-optical electrophysiology approach and quantitative behavior analysis to elucidate the role of L1 neurons and lateral inhibition in attention and reinforcement learning. Furthermore, I propose to use multimodal imaging to study how L1 neurons

control the lower layer cortical neurons and switch cortical states.

4.1.1 L1 neurons in sensory processing of attended vs unattended stimuli

The canonical model for sensory processing is that information propagates from thalamus to L4, up to L2/3, down to L5/6 as output. Cortical L1 is missing here but is very likely involved in selection of novel and salient signals because L1 receives input from thalamus, higher order cortical regions, and neuromodulatory centers. Among cortical L1 are sparsely distributed interneurons. Due to their location, L1 interneurons are ideal to integrate different inputs and control the output through either inhibition or disinhibition, and may thereby function as a switch for filtering noises and controlling attention[94].

To test this model and study the role of L1 neurons in attention, I propose to train the mice to attend to a whisker stimulation of a particular whisker (e.g. C2)[134]. Specifically, head-fixed mice will perform an object location discrimination task with C2 whisker and will report the location of object with licking or not licking. Previous study showed that, the trained mice would then ignore activity in L4 of other whiskers (e.g. E3)[134]. However, the underlying mechanisms of this spatial selective attention are unclear. I hypothesize that, L1 neurons control the selection of inputs by conveying top-down modulation. To test this hypothesis, I will optically measure and compare between the activity of L1 neurons in barrels corresponding to the attentive whisker and barrels corresponding to the

inattentive whisker. I will further use targeted optical perturbations with Optopatch (somArchon-P2A-somCheRiff) and i-Optopatch (somArchon-P2A-somGtACR)[19] to establish causal links between L1 activity and perception and behavior.

For instance, optogenetic activation of L1 neurons corresponding to the inattentive whisker may increase the behavioral perception and attention to this whisker; optogenetic inactivation of L1 neurons corresponding to the attentive whisker may decrease the behavioral perception and attention to this whisker.

Furthermore, my previous discovery on the lateral inhibition and recurrent connection among L1 neurons could function as a powerful gate for spatial selective attention. To test this idea, I propose to manipulate a subset of L1 neurons with high spatial-temporal resolution (e.g., a ring stimulation of neighboring L1 neurons).

4.1.2 plasticity of cortical L1 neurons in associative learning

Our brain can associate behaviorally relevant stimuli (e.g., a neutral sensory input with salient behavioral events, punishment or reward). While such associative learning involves high-order association cortices, primary sensory cortex has recently been found to encode associational information outside the immediate sensory modality[135]. Cortical layer 1 neurons have further been implicated in associative learning[94] by mediating cholinergic activation of the aversive stimulus. We found that, cortical layer 1 neurons receive not only excitatory neuromodulatory inputs

with primary reinforcer such as air puff, but also excitatory inputs from sensory stimuli. Therefore, cortical L1 neurons may associate specific sensory input with contextual information. However, it is unclear at cellular level how these two different inputs converge at L1 neurons. I hypothesize L1 neurons may undergo a plastic change over the course of reinforcement learning and associate these two inputs together.

For instance, L1 neurons potentiate and select the sensory input associated with reinforcement.

To study the integration and cellular plasticity of L1 neurons, I propose to record the activity with varying intervals between whisker stimulation and optogenetic activation of cholinergic terminals locally. To study the role of L1 in associative learning, I propose to record the activity longitudinally during this associative learning (the same Go/No-Go task in session 4.1.1) and correlate the activity with behavioral performance.

4.1.3 probing how L1 neurons switch cortical states with multimodal imaging

Typically, trained mice are attentive in waiting for the reward. They would take action immediately after receiving the go-cue. It is unclear how cortical states switch towards taking action after the go-cue. I hypothesize cortical L1 neurons may function as a switch for controlling cortical states by receiving thalamic

feedback input[136] and modulating pyramidal neurons.

For instance, L1 neurons may switch the cortical states by inhibiting other inhibitory neurons in L2/3 and therefore disinhibiting the pyramidal neurons in L2/3.

To understand how L1 neurons switch cortical states, I propose to perform simultaneous voltage imaging and optogenetic manipulation across cortical layers using prism[137]. One could also perform simultaneous voltage imaging in L1 neurons and calcium imaging in pyramidal neurons in L2/3, L4 and L5.

4.2 Technical outlook

4.2.1 Improve GEVIs

Further improvement of GEVIs would be needed to achieve their holy grail of optophysiology. Fast kinetics need to retain at sub-millisecond in order to follow fast spikes. Otherwise, the GEVIs will act as a low pass filter.

In order to improve GEVIs, it is worth taking a look at the short noise limited signal to noise ratio (SNR): SNR = dF / sqrt (F + B), where dF is the fluorescence change with voltage event of interest, F is baseline fluorescence, B is background fluorescence due to tissue-autofluorescence and out-of-focus fluorescence (in the case of one photon stimulation). Increasing brightness affect dF, F and B proportionally (in the case of one photon stimulation assuming B is mainly from

out-of-focus fluorescence), thus increasing SNR by its square root. Increasing sensitivity (affect dF) will linearly enhance SNR. Similarly, increase dF and F locally at the focal plane without changing B can increase SNR linearly (assuming for dim sensors, B dominates F). Detailed implementation and discussions are described in Chapter 3. Trafficking (affect B) is another important factor to consider as any molecules that do not traffic to the membrane contribute to the background.

One can already realize the difficulty of screening all these parameters together. Perhaps one way to move ahead is hierarchy screening. For instance, as brightness only affect SNR by square root and it is faster to screen with FACS sorting, one could first screen brightness. The most difficult part is to screen sensitivity while maintaining the speed. Presumably the poor trafficking variant will not show high sensitivity with functional recording as screening parameters. Induced transmembrane voltage (ITV)[34] in mammalian cells, and spiking hek cells[138] could serve as a high throughput platform for screening sensitivity and speed. For trafficking in vivo, one may imagine to screen in acute slices.

4.2.2 Future directions on two photon voltage imaging

For two photon voltage imaging, future efforts combining fast scanning with targeting region of interest will likely yield fruitful progress. Another way could be to use scanning-free element such as SLM for two photon excitation and record through camera-based method (It only reduces scattering on the excitation path

but not on the emission path).

4.2.3 Future directions on wide field voltage imaging

For wide field voltage imaging, to further reject out-of-focus background, one may use oblique illumination as that in SCAPE[139], although photon loss needs to be taken into consideration with tilted reimaging.

On the emission side, even with camera recording, it is hard to achieve whole-chip 1 kHz imaging speed. To image at 1 kHz, the camera region of interest (ROI) is restricted to typically 200 rows, centered on the image-sensor midline. To fully use the fast recording of the camera, one may use SLM in the detection path to reimage the emitted photon onto the central chip of the camera. One could also use cylindrical lens to compress the field of view on the emission path.

Another drawback for wide field microscopy is the limited focal depth. One may use wavefront coding mask to extend the depth of field imaging[140].

Eventually, wide field microscope will have limited depth penetration due to aberration. One could use graded-index (GRIN) lenses[141] to bring the region of interest to the surface. One could also use prism[137] for example to image the voltage cross cortical layers. The concern would be tissue damage. Adaptive optics[142], an idea from astronomy, to correct the aberration could also improve the depth penetration.

References

[1] Y. Ozuysal and S. A. Baccus, "Linking the computational structure of variance adaptation to biophysical mechanisms," *Neuron*, vol. 73, no. 5, pp. 1002–1015, 2012.

[2] G. Buzsáki and X.-J. Wang, "Mechanisms of gamma oscillations," *Annual review of neuroscience*, vol. 35, pp. 203–225, 2012.

[3] E. Marder and R. L. Calabrese, "Principles of rhythmic motor pattern generation," *Physiological reviews*, vol. 76, no. 3, pp. 687–717, 1996.

[4] H. K. Inagaki, L. Fontolan, S. Romani, and K. Svoboda, "Discrete attractor dynamics underlies persistent activity in the frontal cortex," *Nature*, vol. 566, no. 7743, p. 212, 2019.

[5] A. V. Egorov, B. N. Hamam, E. Fransén, M. E. Hasselmo, and A. A. Alonso, "Graded persistent activity in entorhinal cortex neurons," *Nature*, vol. 420, no. 6912, p. 173, 2002.

[6] L. Luo, E. M. Callaway, and K. Svoboda, "Genetic dissection of neural circuits: a decade of progress," *Neuron*, vol. 98, no. 2, pp. 256–281, 2018.

[7] D. Marr and T. Poggio, "From understanding computation to understanding neural circuitry," 1976.

[8] B. Tasic, Z. Yao, L. T. Graybuck, K. A. Smith, T. N. Nguyen, D. Bertagnolli, J. Goldy, E. Garren, M. N. Economo, S. Viswanathan, *et al.*, "Shared and distinct transcriptomic cell types across neocortical areas," *Nature*, vol. 563, no. 7729, p. 72, 2018.

[9] E. Neher and B. Sakmann, "Single-channel currents recorded from membrane of denervated frog muscle fibres," *Nature*, vol. 260, no. 5554, p. 799, 1976.

[10] C. C. Petersen, "Whole-cell recording of neuronal membrane potential during behavior," *Neuron*, vol. 95, no. 6, pp. 1266–1281, 2017.

[11] J. J. Jun, N. A. Steinmetz, J. H. Siegle, D. J. Denman, M. Bauza, B. Barbarits, A. K. Lee, C. A. Anastassiou, A. Andrei, Ç. Aydın, *et al.*, "Fully integrated silicon probes for high-density recording of neural activity," *Nature*, vol. 551, no. 7679, p. 232, 2017.

[12] J. Y. Cohen, S. Haesler, L. Vong, B. B. Lowell, and N. Uchida, "Neuron-type-specific signals for reward and punishment in the ventral tegmental area," *nature*, vol. 482, no. 7383, p. 85, 2012.

[13] J. E. Chung, H. R. Joo, J. L. Fan, D. F. Liu, A. H. Barnett, S. Chen, C. Geaghan-Breiner, M. P. Karlsson, M. Karlsson, K. Y. Lee, *et al.*, "High-density, long-lasting, and multi-region electrophysiological recordings using polymer electrode arrays," *Neuron*, vol. 101, no. 1, pp. 21–31, 2019.

[14] T.-M. Fu, G. Hong, T. Zhou, T. G. Schuhmann, R. D. Viveros, and C. M. Lieber, "Stable long-term chronic brain mapping at the single-neuron level," *Nature methods*, vol. 13, no. 10, p. 875, 2016.

[15] C. Van Vreeswijk and H. Sompolinsky, "Chaos in neuronal networks with balanced excitatory and inhibitory activity," *Science*, vol. 274, no. 5293, pp. 1724–1726, 1996.

[16] W. Schultz, P. Dayan, and P. R. Montague, "A neural substrate of prediction and reward," *Science*, vol. 275, no. 5306, pp. 1593–1599, 1997.

[17] R. P. Rao and D. H. Ballard, "Predictive coding in the visual cortex: a functional interpretation of some extra-classical receptive-field effects," *Nature neuroscience*, vol. 2, no. 1, p. 79, 1999.

[18] M. P. Karlsson and L. M. Frank, "Awake replay of remote experiences in the hippocampus," *Nature neuroscience*, vol. 12, no. 7, p. 913, 2009.

[19] M. Mahn, L. Gibor, P. Patil, K. C.-K. Malina, S. Oring, Y. Printz, R. Levy, I. Lampl, and O. Yizhar, "High-efficiency optogenetic silencing with soma-targeted anion-conducting channelrhodopsins," *Nature communications*, vol. 9, 2018.

[20] S. N. Chettih and C. D. Harvey, "Single-neuron perturbations reveal feature-specific competition in v1," *Nature*, vol. 567, no. 7748, p. 334, 2019.

[21] L. Z. Fan, R. Nehme, Y. Adam, E. S. Jung, H. Wu, K. Eggan, D. B. Arnold, and A. E. Cohen, "All-optical synaptic electrophysiology probes mechanism of ketamine-induced disinhibition," *Nature methods*, vol. 15, no. 10, p. 823, 2018.

[22] L. Z. Fan, S. Kheifets, U. L. Böhm, K. D. Piatkevich, H. Wu, V. Parot, M. Xie, E. S. Boyden, A. E. Takesian, and A. E. Cohen, "All-optical electrophysiology reveals excitation, inhibition, and neuromodulation in cortical layer 1," *bioRxiv*, p. 614172, 2019.

[23] M. S. Siegel and E. Y. Isacoff, "A genetically encoded optical probe of membrane voltage," *Neuron*, vol. 19, no. 4, pp. 735–741, 1997.

[24] G. Cao, J. Platisa, V. A. Pieribone, D. Raccuglia, M. Kunst, and M. N. Nitabach, "Genetically targeted optical electrophysiology in intact neural circuits," *Cell*, vol. 154, no. 4, pp. 904–913, 2013.

[25] F. St-Pierre, J. D. Marshall, Y. Yang, Y. Gong, M. J. Schnitzer, and M. Z. Lin, "High-fidelity optical reporting of neuronal electrical activity with an ultrafast fluorescent voltage sensor," *Nature neuroscience*, vol. 17, no. 6, p. 884, 2014.

[26] M. Chavarha, V. Villette, I. Dimov, L. Pradhan, S. Evans, D. Shi, R. Yang, S. Chamberland, J. Bradley, B. Mathieu, *et al.*, "Fast two-photon volumetric imaging of an improved voltage indicator reveals electrical activity in deeply located neurons in the awake brain," *bioRxiv*, p. 445064, 2018.

[27] N. C. Klapoetke, Y. Murata, S. S. Kim, S. R. Pulver, A. Birdsey-Benson, Y. K. Cho, T. K. Morimoto, A. S. Chuong, E. J. Carpenter, Z. Tian, *et al.*, "Independent optical excitation of distinct neural populations," *Nature methods*, vol. 11, no. 3, p. 338, 2014.

[28] A. R. Mardinly, I. A. Oldenburg, N. C. Pegard, S. Sridharan, E. H. Lyall, K. Chesnov, S. G. Brohawn, L. Waller, and H. Adesnik, "Precise multimodal optical control of neural ensemble activity," *Nature neuroscience*, vol. 21, no. 6, p. 881, 2018.

[29] J. Y. Lin, P. M. Knutsen, A. Muller, D. Kleinfeld, and R. Y. Tsien, "Reachr: a red-shifted variant of channelrhodopsin enables deep transcranial optogenetic excitation," *Nature neuroscience*, vol. 16, no. 10, p. 1499, 2013.

[30] O. Yizhar, L. E. Fenno, M. Prigge, F. Schneider, T. J. Davidson, D. J. O'shea, V. S. Sohal, I. Goshen, J. Finkelstein, J. T. Paz, *et al.*, "Neocortical excitation/inhibition balance in information processing and social dysfunction," *Nature*, vol. 477, no. 7363, p. 171, 2011.

[31] J. H. Marshel, Y. S. Kim, T. A. Machado, S. Quirin, B. Benson, J. Kadmon, C. Raja, A. Chibukhchyan, C. Ramakrishnan, M. Inoue, *et al.*, "Cortical layer–specific critical dynamics triggering perception," *Science*, vol. 365, no. 6453, p. eaaw5202, 2019.

[32] J. M. Kralj, D. R. Hochbaum, A. D. Douglass, and A. E. Cohen, "Electrical spiking in escherichia coli probed with a fluorescent voltage-indicating protein," *Science*, vol. 333, no. 6040, pp. 345–348, 2011.

[33] J. M. Kralj, A. D. Douglass, D. R. Hochbaum, D. Maclaurin, and A. E. Cohen, "Optical recording of action potentials in mammalian neurons using a microbial rhodopsin," *Nature methods*, vol. 9, no. 1, p. 90, 2012.

[34] D. R. Hochbaum, Y. Zhao, S. L. Farhi, N. Klapoetke, C. A. Werley, V. Kapoor, P. Zou, J. M. Kralj, D. Maclaurin, N. Smedemark-Margulies, *et al.*, "All-optical electrophysiology in mammalian neurons using engineered microbial rhodopsins," *Nature methods*, vol. 11, no. 8, p. 825, 2014.

[35] K. D. Piatkevich, E. E. Jung, C. Straub, C. Linghu, D. Park, H.-J. Suk, D. R. Hochbaum, D. Goodwin, E. Pnevmatikakis, N. Pak, *et al.*, "A robotic multidimensional directed evolution approach applied to fluorescent voltage reporters," *Nature chemical biology*, vol. 14, no. 4, p. 352, 2018.

[36] Y. Adam, J. J. Kim, S. Lou, Y. Zhao, M. E. Xie, D. Brinks, H. Wu, M. A. Mostajo-Radji, S. Kheifets, V. Parot, *et al.*, "Voltage imaging and optogenetics reveal behaviour-dependent changes in hippocampal dynamics," *Nature*, vol. 569, no. 7756, p. 413, 2019.

[37] P. Zou, Y. Zhao, A. D. Douglass, D. R. Hochbaum, D. Brinks, C. A. Werley, D. J. Harrison, R. E. Campbell, and A. E. Cohen, "Bright and fast multicoloured voltage reporters via electrochromic fret," *Nature communications*, vol. 5, p. 4625, 2014.

[38] Y. Gong, M. J. Wagner, J. Z. Li, and M. J. Schnitzer, "Imaging neural spiking in brain tissue using fret-opsin protein voltage sensors," *Nature communications*, vol. 5, p. 3674, 2014.

[39] Y. Gong, C. Huang, J. Z. Li, B. F. Grewe, Y. Zhang, S. Eismann, and M. J. Schnitzer, "High-speed recording of neural spikes in awake mice and flies with a fluorescent voltage sensor," *Science*, vol. 350, no. 6266, pp. 1361–1366, 2015.

[40] M. Kannan, G. Vasan, C. Huang, S. Haziza, J. Z. Li, H. Inan, M. J. Schnitzer, and V. A. Pieribone, "Fast, in vivo voltage imaging using a red fluorescent indicator," *Nature methods*, vol. 15, no. 12, p. 1108, 2018.

[41] A. S. Abdelfattah, T. Kawashima, A. Singh, O. Novak, H. Liu, Y. Shuai, Y.-C. Huang, L. Campagnola, S. C. Seeman, J. Yu, *et al.*, "Bright and photostable chemigenetic indicators for extended in vivo voltage imaging," *Science*, vol. 365, no. 6454, pp. 699–704, 2019.

[42] A. S. Abdelfattah, R. Valenti, A. Wong, M. Koyama, D. S. Kim, and E. R. Schreiter, "A general approach to engineer positive-going efret voltage indicators," *bioRxiv*, p. 690925, 2019.

[43] K. Svoboda and S. M. Block, "Biological applications of optical forces," *Annual review of biophysics and biomolecular structure*, vol. 23, no. 1, pp. 247–285, 1994.

[44] S. Chamberland, H. H. Yang, M. M. Pan, S. W. Evans, S. Guan, M. Chavarha, Y. Yang, C. Salesse, H. Wu, J. C. Wu, *et al.*, "Fast two-photon imaging of subcellular voltage dynamics in neuronal tissue with genetically encoded indicators," *Elife*, vol. 6, p. e25690, 2017.

[45] R. Lu, W. Sun, Y. Liang, A. Kerlin, J. Bierfeld, J. D. Seelig, D. E. Wilson, B. Scholl, B. Mohar, M. Tanimoto, *et al.*, "Video-rate volumetric functional

imaging of the brain at synaptic resolution," *Nature neuroscience*, vol. 20, no. 4, p. 620, 2017.

[46] W. Yang, J.-e. K. Miller, L. Carrillo-Reid, E. Pnevmatikakis, L. Paninski, R. Yuste, and D. S. Peterka, "Simultaneous multi-plane imaging of neural circuits," *Neuron*, vol. 89, no. 2, pp. 269–284, 2016.

[47] A. Kazemipour, O. Novak, D. Flickinger, J. S. Marvin, A. S. Abdelfattah, J. King, P. M. Borden, J. J. Kim, S. H. Al-Abdullatif, P. E. Deal, *et al.*, "Kilohertz frame-rate two-photon tomography," *Nature methods*, vol. 16, no. 8, p. 778, 2019.

[48] J. Wu, C.-L. Hsu, M. Chavarha, S. Evans, D. Shi, M. Lin, K. Tsia, N. Ji, *et al.*, "Kilohertz in vivo imaging of neural activity," *bioRxiv*, p. 543058, 2019.

[49] A. Yaroslavsky, P. Schulze, I. Yaroslavsky, R. Schober, F. Ulrich, and H. Schwarzmaier, "Optical properties of selected native and coagulated human brain tissues in vitro in the visible and near infrared spectral range," *Physics in Medicine & Biology*, vol. 47, no. 12, p. 2059, 2002.

[50] A. N. Van Den Pol, "Neuropeptide transmission in brain circuits," *Neuron*, vol. 76, no. 1, pp. 98–115, 2012.

[51] N. X. Tritsch and B. L. Sabatini, "Dopaminergic modulation of synaptic transmission in cortex and striatum," *Neuron*, vol. 76, no. 1, pp. 33–50.

[52] T. Kuner and G. J. Augustine, "A genetically encoded ratiometric indicator for chloride: capturing chloride transients in cultured hippocampal neurons," *Neuron*, vol. 27, no. 3, pp. 447–459, 2000.

[53] V. Emiliani, A. E. Cohen, K. Deisseroth, and M. Häusser, "All-optical interrogation of neural circuits," *Journal of Neuroscience*, vol. 35, no. 41, pp. 13917–13926, 2015.

[54] C. A. Werley, T. Brookings, H. Upadhyay, L. A. Williams, O. B. McManus, and G. T. Dempsey, "All-optical electrophysiology for disease modeling and pharmacological characterization of neurons," *Current protocols in pharmacology*, vol. 78, no. 1, pp. 11–20, 2017.

[55] S. Lou, Y. Adam, E. N. Weinstein, E. Williams, K. Williams, V. Parot, N. Kavokine, S. Liberles, L. Madisen, H. Zeng, *et al.*, "Genetically targeted all-optical electrophysiology with a transgenic cre-dependent optopatch mouse," *Journal of Neuroscience*, vol. 36, no. 43, pp. 11059–11073, 2016.

[56] O. A. Shemesh, D. Tanese, V. Zampini, C. Linghu, K. Piatkevich, E. Ronzitti, E. Papagiakoumou, E. S. Boyden, and V. Emiliani, "Temporally precise single-cell-resolution optogenetics," *Nature neuroscience*, vol. 20, no. 12, p. 1796, 2017.

[57] J. H. Krystal, L. P. Karper, J. P. Seibyl, G. K. Freeman, R. Delaney, J. D. Bremner, G. R. Heninger, M. B. Bowers, and D. S. Charney, "Subanesthetic effects of the noncompetitive nmda antagonist, ketamine, in humans: psychotomimetic, perceptual, cognitive, and neuroendocrine responses," *Archives of general psychiatry*, vol. 51, no. 3, pp. 199–214, 1994.

[58] N. V. Kraguljac, M. A. Frölich, S. Tran, D. M. White, N. Nichols, A. Barton-McArdle, M. A. Reid, M. S. Bolding, and A. C. Lahti, "Ketamine modulates hippocampal neurochemistry and functional connectivity: a combined magnetic resonance spectroscopy and resting-state fmri study in healthy volunteers," *Molecular psychiatry*, vol. 22, no. 4, p. 562, 2017.

[59] M. E. Jackson, H. Homayoun, and B. Moghaddam, "Nmda receptor hypofunction produces concomitant firing rate potentiation and burst activity reduction in the prefrontal cortex," *Proceedings of the National Academy of Sciences*, vol. 101, no. 22, pp. 8467–8472, 2004.

[60] V. D. Lazzaro, A. Oliviero, P. Profice, M. Pennisi, F. Pilato, G. Zito, M. Dileone, R. Nicoletti, P. Pasqualetti, and P. Tonali, "Ketamine increases human motor cortex excitability to transcranial magnetic stimulation," *The Journal of physiology*, vol. 547, no. 2, pp. 485–496, 2003.

[61] J. P. Hamm, D. S. Peterka, J. A. Gogos, and R. Yuste, "Altered cortical ensembles in mouse models of schizophrenia," *Neuron*, vol. 94, no. 1, pp. 153–167, 2017.

[62] Y. Izumi and C. F. Zorumski, "Metaplastic effects of subanesthetic ketamine on ca1 hippocampal function," *Neuropharmacology*, vol. 86, pp. 273–281, 2014.

[63] H. C. Grunze, D. G. Rainnie, M. E. Hasselmo, E. Barkai, E. F. Hearn, R. W. McCarley, and R. W. Greene, "Nmda-dependent modulation of ca1 local circuit inhibition," *Journal of Neuroscience*, vol. 16, no. 6, pp. 2034–2043, 1996.

[64] J. E. Lisman, J. T. Coyle, R. W. Green, D. C. Javitt, F. M. Benes, S. Heckers, and A. A. Grace, "Circuit-based framework for understanding neurotransmitter and risk gene interactions in schizophrenia," *Trends in neurosciences*, vol. 31, no. 5, pp. 234–242, 2008.

[65] Y. Adam, J. J. Kim, S. Lou, Y. Zhao, D. Brinks, H. Wu, M. A. Mostajo-Radji, S. Kheifets, V. Parot, S. Chettih, *et al.*, "All-optical electrophysiology reveals brain-state dependent changes in hippocampal subthreshold dynamics and excitability," *bioRxiv*, p. 281618, 2018.

[66] V. Gradinaru, F. Zhang, C. Ramakrishnan, J. Mattis, R. Prakash, I. Diester, I. Goshen, K. R. Thompson, and K. Deisseroth, "Molecular and cellular approaches for diversifying and extending optogenetics," *Cell*, vol. 141, no. 1, pp. 154–165, 2010.

[67] C. S. Branda and S. M. Dymecki, "Talking about a revolution: The impact of site-specific recombinases on genetic analyses in mice," *Developmental cell*, vol. 6, no. 1, pp. 7–28, 2004.

[68] D. Atasoy, Y. Aponte, H. H. Su, and S. M. Sternson, "A flex switch targets channelrhodopsin-2 to multiple cell types for imaging and long-range circuit mapping," *Journal of Neuroscience*, vol. 28, no. 28, pp. 7025–7030, 2008.

[69] A. Saunders, C. Johnson, and B. Sabatini, "Novel recombinant adeno-associated viruses for cre activated and inactivated transgene expression in neurons," *Frontiers in neural circuits*, vol. 6, p. 47, 2012.

[70] L. Petreanu, T. Mao, S. M. Sternson, and K. Svoboda, "The subcellular organization of neocortical excitatory connections," *Nature*, vol. 457, no. 7233, p. 1142, 2009.

[71] T.-W. Chen, T. J. Wardill, Y. Sun, S. R. Pulver, S. L. Renninger, A. Baohan, E. R. Schreiter, R. A. Kerr, M. B. Orger, V. Jayaraman, *et al.*, "Ultrasensitive fluorescent proteins for imaging neuronal activity," *Nature*, vol. 499, no. 7458, p. 295, 2013.

[72] H. Dana, B. Mohar, Y. Sun, S. Narayan, A. Gordus, J. P. Hasseman, G. Tsegaye, G. T. Holt, A. Hu, D. Walpita, *et al.*, "Sensitive red protein calcium indicators for imaging neural activity," *Elife*, vol. 5, p. e12727, 2016.

[73] M. Fischer, S. Kaech, D. Knutti, and A. Matus, "Rapid actin-based plasticity in dendritic spines," *Neuron*, vol. 20, no. 5, pp. 847–854, 1998.

[74] B. M. Burkel, G. Von Dassow, and W. M. Bement, "Versatile fluorescent probes for actin filaments based on the actin-binding domain of utrophin," *Cell motility and the cytoskeleton*, vol. 64, no. 11, pp. 822–832, 2007.

[75] G. G. Gross, J. A. Junge, R. J. Mora, H.-B. Kwon, C. A. Olson, T. T. Takahashi, E. R. Liman, G. C. Ellis-Davies, A. W. McGee, B. L. Sabatini, *et al.*, "Recombinant probes for visualizing endogenous synaptic proteins in living neurons," *Neuron*, vol. 78, no. 6, pp. 971–985, 2013.

[76] J. S. Klein, S. Jiang, R. P. Galimidi, J. R. Keeffe, and P. J. Bjorkman, "Design and characterization of structured protein linkers with differing flexibilities," *Protein Engineering, Design & Selection*, vol. 27, no. 10, pp. 325–330, 2014.

[77] C. A. Baker, Y. M. Elyada, A. Parra, and M. M. Bolton, "Cellular resolution circuit mapping with temporal-focused excitation of soma-targeted channelrhodopsin," *Elife*, vol. 5, p. e14193, 2016.

[78] C. R. Gerfen, R. Paletzki, and N. Heintz, "Gensat bac cre-recombinase driver lines to study the functional organization of cerebral cortical and basal ganglia circuits," *Neuron*, vol. 80, no. 6, pp. 1368–1383, 2013.

[79] F. A. Edwards, A. Konnerth, and B. Sakmann, "Quantal analysis of inhibitory synaptic transmission in the dentate gyrus of rat hippocampal slices: a

patch-clamp study.," *The Journal of Physiology*, vol. 430, no. 1, pp. 213–249, 1990.

[80] R. Dingledine, *Brain slices*. Springer Science & Business Media, 2013.

[81] G. B. Potter, M. A. Petryniak, E. Shevchenko, G. L. McKinsey, M. Ekker, and J. L. Rubenstein, "Generation of cre-transgenic mice using dlx1/dlx2 enhancers and their characterization in gabaergic interneurons," *Molecular and Cellular Neuroscience*, vol. 40, no. 2, pp. 167–186, 2009.

[82] L. Poitras, N. Ghanem, G. Hatch, and M. Ekker, "The proneural determinant mash1 regulates forebrain dlx1/2 expression through the i12b intergenic enhancer," *Development*, vol. 134, no. 9, pp. 1755–1765, 2007.

[83] G. Colasante, G. Lignani, A. Rubio, L. Medrihan, L. Yekhlef, A. Sessa, L. Massimino, S. G. Giannelli, S. Sacchetti, M. Caiazzo, *et al.*, "Rapid conversion of fibroblasts into functional forebrain gabaergic interneurons by direct genetic reprogramming," *Cell Stem Cell*, vol. 17, no. 6, pp. 719–734, 2015.

[84] D. A. McCormick, B. W. Connors, J. W. Lighthall, and D. A. Prince, "Comparative electrophysiology of pyramidal and sparsely spiny stellate neurons of the neocortex," *Journal of neurophysiology*, vol. 54, no. 4, pp. 782–806, 1985.

[85] A. C. Kwan and Y. Dan, "Dissection of cortical microcircuits by single-neuron stimulation in vivo," *Current Biology*, vol. 22, no. 16, pp. 1459–1467, 2012.

[86] J. M. McNally, R. W. McCarley, J. T. McKenna, Y. Yanagawa, and R. E. Brown, "Complex receptor mediation of acute ketamine application on in vitro gamma oscillations in mouse prefrontal cortex: modeling gamma band oscillation abnormalities in schizophrenia," *Neuroscience*, vol. 199, pp. 51–63, 2011.

[87] J. W. Kinney, C. N. Davis, I. Tabarean, B. Conti, T. Bartfai, and M. M. Behrens, "A specific role for nr2a-containing nmda receptors in the maintenance of parvalbumin and gad67 immunoreactivity in cultured interneurons," *Journal of Neuroscience*, vol. 26, no. 5, pp. 1604–1615, 2006.

[88] D. Xi, B. Keeler, W. Zhang, J. D. Houle, and W.-J. Gao, "Nmda receptor subunit expression in gabaergic interneurons in the prefrontal cortex: application of laser microdissection technique," *Journal of neuroscience methods*, vol. 176, no. 2, pp. 172–181, 2009.

[89] P. Paoletti and J. Neyton, "Nmda receptor subunits: function and pharmacology," *Current opinion in pharmacology*, vol. 7, no. 1, pp. 39–47, 2007.

[90] R. Jones and E. Bühl, "Basket-like interneurones in layer ii of the entorhinal cortex exhibit a powerful nmda-mediated synaptic excitation," *Neuroscience letters*, vol. 149, no. 1, pp. 35–39, 1993.

[91] Y. Adam *et al.*, "All-optical electrophysiology in awake behaving rodents," 2017.

[92] X. Jiang, G. Wang, A. J. Lee, R. L. Stornetta, and J. J. Zhu, "The organization of two new cortical interneuronal circuits," *Nature neuroscience*, vol. 16, no. 2, p. 210, 2013.

[93] A. E. Takesian, L. J. Bogart, J. W. Lichtman, and T. K. Hensch, "Inhibitory circuit gating of auditory critical-period plasticity," *Nature neuroscience*, vol. 21, no. 2, p. 218, 2018.

[94] J. J. Letzkus, S. B. Wolff, E. M. Meyer, P. Tovote, J. Courtin, C. Herry, and A. Lüthi, "A disinhibitory microcircuit for associative fear learning in the auditory cortex," *Nature*, vol. 480, no. 7377, p. 331, 2011.

[95] Y. Zhu and J. J. Zhu, "Rapid arrival and integration of ascending sensory information in layer 1 nonpyramidal neurons and tuft dendrites of layer 5 pyramidal neurons of the neocortex," *Journal of Neuroscience*, vol. 24, no. 6, pp. 1272–1279, 2004.

[96] S. J. Cruikshank, O. J. Ahmed, T. R. Stevens, S. L. Patrick, A. N. Gonzalez, M. Elmaleh, and B. W. Connors, "Thalamic control of layer 1 circuits in prefrontal cortex," *Journal of Neuroscience*, vol. 32, no. 49, pp. 17813–17823, 2012.

[97] S. Lee, I. Kruglikov, Z. J. Huang, G. Fishell, and B. Rudy, "A disinhibitory circuit mediates motor integration in the somatosensory cortex," *Nature neuroscience*, vol. 16, no. 11, p. 1662, 2013.

[98] L. M. Palmer, J. M. Schulz, S. C. Murphy, D. Ledergerber, M. Murayama, and M. E. Larkum, "The cellular basis of gabab-mediated interhemispheric inhibition," *Science*, vol. 335, no. 6071, pp. 989–993, 2012.

[99] R. B. Poorthuis, K. Muhammad, M. Wang, M. B. Verhoog, S. Junek, A. Wrana, H. D. Mansvelder, and J. J. Letzkus, "Rapid neuromodulation of layer 1 interneurons in human neocortex," *Cell reports*, vol. 23, no. 4, pp. 951–958, 2018.

[100] S. Lee, J. Hjerling-Leffler, E. Zagha, G. Fishell, and B. Rudy, "The largest group of superficial neocortical gabaergic interneurons expresses ionotropic serotonin receptors," *Journal of Neuroscience*, vol. 30, no. 50, pp. 16796–16808, 2010.

[101] A. J. Lee, G. Wang, X. Jiang, S. M. Johnson, E. T. Hoang, F. Lanté, R. L. Stornetta, M. P. Beenhakker, Y. Shen, and J. Julius Zhu, "Canonical organization of layer 1 neuron-led cortical inhibitory and disinhibitory interneuronal circuits," *Cerebral Cortex*, vol. 25, no. 8, pp. 2114–2126, 2014.

[102] E. Abs, R. B. Poorthuis, D. Apelblat, K. Muhammad, M. B. Pardi, L. Enke, D. Kushinsky, D.-L. Pu, M. F. Eizinger, K.-K. Conzelmann, *et al.*, "Learning-related plasticity in dendrite-targeting layer 1 interneurons," *Neuron*, vol. 100, no. 3, pp. 684–699, 2018.

[103] L. Gabernet, S. P. Jadhav, D. E. Feldman, M. Carandini, and M. Scanziani, "Somatosensory integration controlled by dynamic thalamocortical feed-forward inhibition," *Neuron*, vol. 48, no. 2, pp. 315–327, 2005.

[104] M. Wehr and A. M. Zador, "Balanced inhibition underlies tuning and sharpens spike timing in auditory cortex," *Nature*, vol. 426, no. 6965, p. 442, 2003.

[105] Z. Chu, M. Galarreta, and S. Hestrin, "Synaptic interactions of late-spiking neocortical neurons in layer 1," *Journal of Neuroscience*, vol. 23, no. 1, pp. 96–102, 2003.

[106] B. Schuman, R. P. Machold, Y. Hashikawa, J. Fuzik, G. J. Fishell, and B. Rudy, "Four unique interneuron populations reside in neocortical layer 1," *Journal of Neuroscience*, vol. 39, no. 1, pp. 125–139, 2019.

[107] B. Hangya, S. P. Ranade, M. Lorenc, and A. Kepecs, "Central cholinergic neurons are rapidly recruited by reinforcement feedback," *Cell*, vol. 162, no. 5, pp. 1155–1168, 2015.

[108] A. S. Abdelfattah, T. Kawashima, A. Singh, O. Novak, H. Liu, Y. Shuai, Y.-C. Huang, J. B. Grimm, R. Patel, J. Friedrich, *et al.*, "Bright and photostable chemigenetic indicators for extended in vivo voltage imaging," *bioRxiv*, p. 436840, 2018.

[109] K. D. Piatkevich, S. Bensussen, H.-a. Tseng, S. N. Shroff, V. G. Lopez-Huerta, D. Park, E. E. Jung, O. A. Shemesh, C. Straub, H. J. Gritton, *et al.*, "Population imaging of neural activity in awake behaving mice in multiple brain regions," *bioRxiv*, p. 616094, 2019.

[110] M. Segal and J. L. Barker, "Rat hippocampal neurons in culture: voltage-clamp analysis of inhibitory synaptic connections," *Journal of neurophysiology*, vol. 52, no. 3, pp. 469–487, 1984.

[111] C. Lutz, T. S. Otis, V. DeSars, S. Charpak, D. A. DiGregorio, and V. Emiliani, "Holographic photolysis of caged neurotransmitters," *Nature Methods*, vol. 5, no. 9, p. 821, 2008.

[112] R. Egger, A. C. Schmitt, D. J. Wallace, B. Sakmann, M. Oberlaender, and J. N. Kerr, "Robustness of sensory-evoked excitation is increased by inhibitory inputs to distal apical tuft dendrites," *Proceedings of the National Academy of Sciences*, vol. 112, no. 45, pp. 14072–14077, 2015.

[113] C. R. Cadwell, A. Palasantza, X. Jiang, P. Berens, Q. Deng, M. Yilmaz, J. Reimer, S. Shen, M. Bethge, K. F. Tolias, *et al.*, "Electrophysiological, transcriptomic and morphologic profiling of single neurons using patch-seq," *Nature biotechnology*, vol. 34, no. 2, p. 199, 2016.

[114] C. M. Constantinople and R. M. Bruno, "Effects and mechanisms of wakefulness on local cortical networks," *Neuron*, vol. 69, no. 6, pp. 1061–1068, 2011.

[115] E. Eggermann, Y. Kremer, S. Crochet, and C. C. Petersen, "Cholinergic signals in mouse barrel cortex during active whisker sensing," *Cell reports*, vol. 9, no. 5, pp. 1654–1660, 2014.

[116] S. Arroyo, C. Bennett, D. Aziz, S. P. Brown, and S. Hestrin, "Prolonged disynaptic inhibition in the cortex mediated by slow, non-$\alpha 7$ nicotinic excitation of a specific subset of cortical interneurons," *Journal of Neuroscience*, vol. 32, no. 11, pp. 3859–3864, 2012.

[117] H. Markram, E. Muller, S. Ramaswamy, M. W. Reimann, M. Abdellah, C. A. Sanchez, A. Ailamaki, L. Alonso-Nanclares, N. Antille, S. Arsever, *et al.*, "Reconstruction and simulation of neocortical microcircuitry," *Cell*, vol. 163, no. 2, pp. 456–492, 2015.

[118] E. M. Izhikevich, "Simple model of spiking neurons," *IEEE Transactions on neural networks*, vol. 14, no. 6, pp. 1569–1572, 2003.

[119] E. M. Izhikevich, *Dynamical Systems in Neuroscience*. 2018.

[120] E. M. Izhikevich and G. M. Edelman, "Large-scale model of mammalian thalamocortical systems," *Proceedings of the national academy of sciences*, vol. 105, no. 9, pp. 3593–3598, 2008.

[121] X. Jiang, S. Shen, C. R. Cadwell, P. Berens, F. Sinz, A. S. Ecker, S. Patel, and A. S. Tolias, "Principles of connectivity among morphologically defined cell types in adult neocortex," *Science*, vol. 350, no. 6264, p. aac9462, 2015.

[122] A. L. Hodgkin, "The local electric changes associated with repetitive action in a non-medullated axon," *The Journal of physiology*, vol. 107, no. 2, pp. 165–181, 1948.

[123] N. Burnashev, H. Monyer, P. H. Seeburg, and B. Sakmann, "Divalent ion permeability of ampa receptor channels is dominated by the edited form of a single subunit," *Neuron*, vol. 8, no. 1, pp. 189–198, 1992.

[124] M. Ballivet, P. Nef, S. Couturier, D. Rungger, C. Bader, D. Bertrand, and E. Cooper, "Electrophysiology of a chick neuronal nicotinic acetylcholine receptor expressed in xenopus oocytes after cdna injection," *Neuron*, vol. 1, no. 9, pp. 847–852, 1988.

[125] N. K. McKinnon, D. C. Reeves, and M. H. Akabas, "5-ht3 receptor ion size selectivity is a property of the transmembrane channel, not the cytoplasmic vestibule portals," *The Journal of general physiology*, vol. 138, no. 4, pp. 453–466, 2011.

[126] H. Zhang, E. Reichert, and A. E. Cohen, "Optical electrophysiology for probing function and pharmacology of voltage-gated ion channels," *Elife*, vol. 5, p. e15202, 2016.

[127] G. G. Turrigiano, K. R. Leslie, N. S. Desai, L. C. Rutherford, and S. B. Nelson, "Activity-dependent scaling of quantal amplitude in neocortical neurons," *Nature*, vol. 391, no. 6670, p. 892, 1998.

[128] G. J. Goldey, D. K. Roumis, L. L. Glickfeld, A. M. Kerlin, R. C. Reid, V. Bonin, D. P. Schafer, and M. L. Andermann, "Removable cranial windows for long-term imaging in awake mice," *Nature protocols*, vol. 9, no. 11, p. 2515, 2014.

[129] E. A. Pnevmatikakis and A. Giovannucci, "Normcorre: An online algorithm for piecewise rigid motion correction of calcium imaging data," *Journal of neuroscience methods*, vol. 291, pp. 83–94, 2017.

[130] E. A. Mukamel, A. Nimmerjahn, and M. J. Schnitzer, "Automated analysis of cellular signals from large-scale calcium imaging data," *Neuron*, vol. 63, no. 6, pp. 747–760, 2009.

[131] A. Brombas, L. N. Fletcher, and S. R. Williams, "Activity-dependent modulation of layer 1 inhibitory neocortical circuits by acetylcholine," *Journal of Neuroscience*, vol. 34, no. 5, pp. 1932–1941, 2014.

[132] H. S. Meyer, R. Egger, J. M. Guest, R. Foerster, S. Reissl, and M. Oberlaender, "Cellular organization of cortical barrel columns is whisker-specific," *Proceed-*

ings of the national academy of sciences, vol. 110, no. 47, pp. 19113–19118, 2013.

[133] D. H. O'Connor, D. Huber, and K. Svoboda, "Reverse engineering the mouse brain," *Nature*, vol. 461, no. 7266, p. 923, 2009.

[134] D. H. O'connor, S. A. Hires, Z. V. Guo, N. Li, J. Yu, Q.-Q. Sun, D. Huber, and K. Svoboda, "Neural coding during active somatosensation revealed using illusory touch," *Nature neuroscience*, vol. 16, no. 7, p. 958, 2013.

[135] C. O. Lacefield, E. A. Pnevmatikakis, L. Paninski, and R. M. Bruno, "Reinforcement learning recruits somata and apical dendrites across layers of primary sensory cortex," *Cell reports*, vol. 26, no. 8, pp. 2000–2008, 2019.

[136] Z. V. Guo, H. K. Inagaki, K. Daie, S. Druckmann, C. R. Gerfen, and K. Svoboda, "Maintenance of persistent activity in a frontal thalamocortical loop," *Nature*, vol. 545, no. 7653, p. 181, 2017.

[137] M. L. Andermann, N. B. Gilfoy, G. J. Goldey, R. N. Sachdev, M. Wölfel, D. A. McCormick, R. C. Reid, and M. J. Levene, "Chronic cellular imaging of entire cortical columns in awake mice using microprisms," *Neuron*, vol. 80, no. 4, pp. 900–913, 2013.

[138] J. Park, C. A. Werley, V. Venkatachalam, J. M. Kralj, S. D. Dib-Hajj, S. G. Waxman, and A. E. Cohen, "Screening fluorescent voltage indicators with spontaneously spiking hek cells," *PloS one*, vol. 8, no. 12, p. e85221, 2013.

[139] M. B. Bouchard, V. Voleti, C. S. Mendes, C. Lacefield, W. B. Grueber, R. S. Mann, R. M. Bruno, and E. M. Hillman, "Swept confocally-aligned planar excitation (scape) microscopy for high-speed volumetric imaging of behaving organisms," *Nature photonics*, vol. 9, no. 2, p. 113, 2015.

[140] S. Quirin, D. S. Peterka, and R. Yuste, "Instantaneous three-dimensional sensing using spatial light modulator illumination with extended depth of field imaging," *Optics express*, vol. 21, no. 13, pp. 16007–16021, 2013.

[141] J. C. Jung, A. D. Mehta, E. Aksay, R. Stepnoski, and M. J. Schnitzer, "In vivo mammalian brain imaging using one-and two-photon fluorescence

microendoscopy," *Journal of neurophysiology*, vol. 92, no. 5, pp. 3121–3133, 2004.

[142] N. Ji, "Adaptive optical fluorescence microscopy," *Nature methods*, vol. 14, no. 4, p. 374, 2017.